



UNIVERSITÀ DEGLI STUDI DI CATANIA

IN CONVENZIONE CON



UNIVERSITÀ DEGLI STUDI DI PALERMO

DOTTORATO DI RICERCA IN

SCIENZA DEI MATERIALI E NANOTECNOLOGIE - XXIX CICLO

ROBERTO SCHIMMENTI

**THEORETICAL INSIGHTS INTO HETEROGENEOUS
METALLIC CATALYSTS FOR BIOMASS BASED
HYDROGEN PRODUCTION**

TUTOR: PROF. DARIO DUCA

COORDINATORE: PROF. MARIA GRAZIA GRIMALDI

TESI PER IL CONSEGUIMENTO DEL TITOLO DI DOTTORE DI RICERCA



UNIVERSITÀ DEGLI STUDI DI PALERMO



UNIVERSITÀ DEGLI STUDI DI CATANIA

DOCTORAL THESIS

Theoretical insights into heterogeneous metallic catalysts for biomass based hydrogen production

Ph.D. Candidate:
Roberto Schimmenti

Supervisor:
Prof. Dario Duca

*A thesis submitted in fulfillment of the requirements
for the degree of Doctor of Philosophy*

in

Material Science and Nanotechnology

January 29, 2017

Acknowledgements

I would like to thank all the people and organizations that gave their contribution during the three years of my Ph.D.

First of all, I would like to acknowledge all the members of the Computational Chemistry Center of Palermo (CCCP). A special thank goes to Prof. Dario Duca for his supervision and Dr. Remedios Cortese for her mentoring activity.

I would also like to thank Prof. Dmitry Murzin and M.Sc. Lidia Godina, from the Laboratory of Industrial Chemistry and Reaction Engineering of the Åbo Akademi University of Turku (FI), for fruitful discussions on 1,2-PDO decomposition mechanism and APR.

I want to thank Prof. Carlo Adamo and Prof. Dmitry Murzin, who accepted to referee this thesis, for their availability.

Finally I would like to thank all the members of the Computational Surface Science and Catalysis (CSSC) group of the University of Wisconsin-Madison (USA); in particular, I would like to express my gratitude to Prof. Manos Mavrikakis for his guidance and availability.

Part of the results presented in this thesis were collected using the computational resources of the National Energy Research Scientific Computing Center, a DOE Office of Science User Facility supported by the Office of Science of the U.S. Department of Energy under Contract No. DE-AC02-05CH11231.

Funding by European Union Seventh Framework Programme (FP7/2007-2013) within the project SusFuelCat: "Sustainable fuel production by aqueous phase reforming-understanding catalysis and hydrothermal stability of carbon supported noble metals" GA: CP-IP 310490 (http://cordis.europa.eu/projects/rcn/106702_en.html) is gratefully acknowledged.

Palermo, 11/13/2016

R. S.

Preface

This Ph.D. thesis, entitled "Theoretical insights into heterogeneous metallic catalysts for biomass based hydrogen production", is the result of the work mainly carried out at the Department of Physics and Chemistry of the University of Palermo, from January 2013 to November 2016. Part of the results, mainly reported and discussed in the Chapter III of the thesis, were collected at the Department of Chemical and Biological Engineering of the University of Wisconsin-Madison, during a six months research period spent in the Computational Catalysis and Surface Group.

The thesis is completely based on computational approaches (mainly DFT) applied to the study of metal based catalyst for hydrogen production and it is structured in three main chapters:

- Chapter I introduces to the study of biomass based hydrogen production technologies, with particular attention to metal catalyzed aqueous phase reforming and formic acid decomposition. The field of computational catalysis is introduced in the same framework;
- In Chapter II, the 1,2-Propanediol decomposition mechanism is studied using two low Miller-index platinum model surfaces, (111) and (100);
- In Chapter III, the catalytic properties of a boron nitride supported sub-nanometric palladium cluster are analyzed, focusing on its potential use for the selective decomposition of formic acid to hydrogen.

Besides the investigated systems, a more general distinction underlies Chapters II and III: in the former the study was carried out mainly with interpretative purposes, on the basis of experimental studies carried out at the Laboratory of Industrial Chemistry and Reaction Engineering of the Åbo Akademi University (AAU) of Turku (FI); instead, in Chapter III, the computational approach used has a more predictive intent.

Density Functional Theory was rigorously treated in the appendix of the thesis, while the computational details used for treating the different systems were reported at the beginning of each chapter.

Palermo, 11/13/2016

R. S.

Abstract

The study of different metallic catalysts (Pt, Pd) for the 1,2-Propanediol (1,2-PDO) and formic acid (FA) to hydrogen conversion was addressed by means of computational methods. In order to shed light into the key factors governing the reactivity of these catalysts multiple models were used, ranging from Pt low Miller-index (111) and (100) like surfaces to supported sub-nanometric Pd clusters. Through a detailed study of the competition between C-H, O-H and C-C bond breakings, it was demonstrated that the 1,2-PDO Pt catalyzed decomposition is likely to occur *via* consecutive dehydrogenation steps, followed by C-C bond cleavages. These latter are more favoured once terminal CO moieties are formed. Hydroxyacetone resulted to be among the major by-products of the reaction. These findings are common both to (111) and (100) Pt surfaces, suggesting that the decomposition reaction may be structure insensitive. In parallel, the catalytic properties of a *h*-BN supported sub-nanometric Pd₆ cluster toward FA dehydrogenation were investigated. A QM/MM approach was used for studying the nucleation mechanism of selected Pd clusters onto a boron nitride nanotube (BNNT) support and the information gained were exploited for the reactivity study. In this framework, the competition between the formate (HCOO) and carboxyl (COOH) FA decomposition pathways was discussed. The Pd₆ undercoordination was proposed to be at the basis of a major selectivity towards the formation of the HCOO intermediate. Conversely, the production of CO seems to be inhibited, and this could represent a major improvement for the CO-free production of hydrogen. A more realistic picture of the catalytic system was achieved by taking into account a variety of effects, such as support defectivity and metallic catalyst reconstruction. These were demonstrated to have a non-negligible impact on the FA decomposition reaction mechanism. In particular, the B vacancy-mediated dehydrogenation was found to be competitive with the Pd-mediated one, thus suggesting that the support could actively take part to the catalytic process.

Keywords: Catalysis, DFT, Biomass, Hydrogen, Sub-nanometric catalysts, Platinum, Palladium, Boron Nitride

Contents

Acknowledgements	i
Preface	iii
Abstract	v
1 Introduction	1
1.1 Hydrogen Economy	1
1.2 Biomass based sustainable hydrogen production	2
1.2.1 Reforming	2
Catalysis role in biomass derived molecules reforming	3
1.2.2 The case of formic acid	6
1.3 An overall view on computational catalysis	8
1.3.1 From molecular events to the prediction of catalyst properties	8
1.3.2 Case studies	12
1.4 Aim of the thesis	18
2 Platinum catalyzed 1,2-PDO decomposition	19
2.1 Computational Details	20
2.2 Part I - 1,2-PDO decomposition on a Pt(111) surface	21
Results and Discussion	21
2.2.1 Kinetic of the first H ₂ molecule loss	21
Step I	21
Step II	23
2.2.2 Energetics of intermediates in steps I and II	25
2.2.3 Further dehydrogenations	26
The fate of INTe and INTf	31
2.2.4 C-C bond breakings	31
2.2.5 The reaction mechanism	33
2.2.6 BEP relationships	35
2.3 Part II - 1,2-PDO decomposition on a Pt(100) surface	38
Results and Discussion	38
2.3.1 First H ₂ loss	39
1,2-PDO - 1H	39

1,2-PDO - 2H	40
2.3.2 Second H ₂ loss	41
1,2-PDO - 3H	43
1,2-PDO - 4H	43
1,2-PDO - 5H	46
2.3.3 C-C bond cleavages	47
2.3.4 Structure sensitivity	47
2.4 Conclusions	51
3 Computational Design of a Boron Nitride Supported Pd Catalyst	53
3.1 Part I - Growth of a sub-nanometric Pd cluster on a boron nitride support	55
3.1.1 Computational Details	55
3.1.2 Results and Discussion	56
Growth thermodynamics	64
3.2 Part II - Reactivity of formic acid on <i>h</i> -BN supported Pd ₆ catalyst	67
3.2.1 Computational Details	67
3.2.2 Results	68
Pd ₆ / <i>h</i> -BN interaction	68
Formic acid adsorption	71
Formic acid decomposition	73
Top Face - Formate Pathway	73
Top Face - Carboxyl Pathway	76
Perimetral sites reactivity	77
3.2.3 Discussion	80
Size sensitivity	80
Competition between HCOO and COOH pathways	83
Hydrogen spillover	86
3.3 Part III - Reactivity of formic acid on a defective <i>h</i> -BN supported Pd ₆ catalyst	88
3.3.1 Computational Details	88
3.3.2 Results	88
Adsorption of Pd ₆ on defective <i>h</i> -B _V N	88
Formic acid adsorption	89
Formic acid decomposition	91
Top Face - Formate Pathway	91
Top Face - Carboxyl Pathway	93
Perimetral sites reactivity	96
3.3.3 Discussion	98
Competition between HCOO and COOH pathways	98
Hydrogen availability	101
3.4 Conclusions	103
4 Concluding remarks	105

A Density Functional Theory Formalism	107
Bibliography	117

1 Introduction

Hydrogen Economy

The advantages of using hydrogen as fuel are today worldwide recognized: among all the chemicals, H_2 has one of the highest chemical energy per mass ratio (142 M J kg^{-1} vs 47 M J kg^{-1} for liquid hydrocarbons); the combustion of H_2 with oxygen leads to water and thus it is practically a pollutant free process. The leading role of hydrogen in the global future energetic panorama is witnessed by the efforts that structures such as the U.S. Department of Energy (DOE) are making to respect a timeline that will lead us toward the so called "Hydrogen Economy", by 2040.

The term "Hydrogen Economy" (HE) describes an economical, industrial and social system in which hydrogen is exploited as energy vector; HE is made up of the chain of all the processes that carry hydrogen from production to its effective use, passing through storage and distribution. Unfortunately, almost every step of the HE system suffers of severe obstacles that slow down the transition toward a hydrogen based fuel strategy.

Aside from pure economical and technical arguments, specific environmental requirements must be satisfied by each step of a energy vector life cycle. The production methodologies sustainability is related to multiple factors, but nature of the starting material used and by-products produced are among the most critical. Dincer and Acar [1] have reported in a recent review at least nineteen different hydrogen production methods among electrical, thermal or hybrid processes; anyway, the wide majority of hydrogen is produced through natural gas steam reforming that, despite being the cheapest method, relies completely on non-renewable feedstocks. On the contrary, coal gasification, that is both economically and technologically profitable, produces high amounts of CO_2 from a non-renewable raw material.

Once produced, other issues arise from the storage step: indeed, 1 kg of gaseous H_2 at room temperature and atmospheric pressure occupies more than 10 m^3 , an order of magnitude unpractical for transportation and storage purposes.

In order to overtake these limits, research is really active in the study of new production and storage technologies. In particular, obtaining almost CO free H_2 from renewable feedstocks is

one of the major challenges: the absence of CO is a fundamental prerequisite for efficiently use hydrogen in fuel cells, whose anode materials particularly suffer of poisoning phenomena.

Biomass based sustainable hydrogen production

Today the research into alternative, viable, hydrogen production methods is really active and as a consequence the associated literature is boundless. For the purposes of this dissertation it has been chosen to focus only on a particular hydrogen production field, that is to say biomass processing. Anyway electrolysis or photocatalytic water splitting should be mentioned as well.

Vegetable derived biomasses are well geographically distributed, they are abundant and easily storable; feedstocks are usually cheap and, when processed, the final CO₂ emissions has no net impact on the environment, being reintroduced in the carbohydrates cycle. Generally, biomass processing regards, for obvious reasons, non-edible materials such as lignocellulosic biomasses. These are complex raw feedstocks, rich in cellulose, hemicellulose, lignin and other substances. Only a few methods such as pure or hydrothermal gasification allow an almost direct conversion of biomass into hydrogen (commonly as *syngas*) while, the first step of biomass industry is usually the transformation of the raw supply into more processable materials.

Thermochemical methods such as pyrolysis are among the most used: the process requires lower temperature than gasification but leads to a complex mixture of condensable and non-condensable gas, liquid and solid (*char*) products; the non-condensable gas is composed by low molecular weight molecules such as H₂, CO, CO₂ and CH₄ while the condensable fraction is made up of heavier products. The liquid instead, known as pyrolysis oil, is rich in oxygenated compounds that can be further processed, through hydrodeoxygenation (HDO) with the aim of lowering the total amount of oxygens, increasing the C/H ratio (but consuming hydrogen). Alternatively, lignocellulosic biomasses, after different pretreating that may include also low temperature pyrolysis, can be hydrolyzed with chemical or enzymatic methods, leading to glucose (the constituting monomer of cellulose) that can be then further processed to give a variety of oxygenates or other chemical platforms with carbon atom chains going from C₁ to C₆. However, several other methodologies for the direct conversion of lignocellulose to more valuable chemicals have been proposed in the literature [2].

Reforming

Irrespective of the initial product, coming from the pretreating steps described above, further processing or completely different not biomass based processes, reforming is the key step used for obtaining hydrogen from oxygenate compounds. In fact, as shown in Table 1.1, a variety of chemicals can be used, most of them directly or indirectly obtainable from biomass processing [3].

Syngas (CO+H₂) can be produced with different reforming variations:

1.2. Biomass based sustainable hydrogen production

- Steam Reforming (SR). It is the most classical protocol to produce syngas starting from hydrocarbons or oxygenates in presence of water; the process is carried out in vapor phase at temperatures in the range 1000-1400 K;
- Partial Oxidation (POx). In vapor phase, hydrocarbons or oxygenates are reformed with O₂; the operating temperatures are lower than SR but hydrogen yield is lower;
- Aqueous Phase Reforming (APR). The reaction takes place in aqueous solution at intermediate temperatures (450-540 K); there is no need to vaporize oxygenates and water, with a consequent energetic advantage; Water Gas Shift (WGS) is thermodynamically favoured in the APR reaction conditions and so the two reactions can be carried out in one single step [4].

Further methodologies include photocatalytic reforming, supercritical water reforming, dry reforming, plasma reforming and others.

Table 1.1 – Typical chemicals exploitable for the production of hydrogen and the associated production strategy; biomass based process are underlined. (Adapted from Li *et al.* [3])

Chemical	Model Compound	Source/Production
monoalcohol	methanol	synthesis from syngas
	ethanol	ethylene dehydration; <u>sugars fermentation</u>
aldehydes	formaldehyde	methanol oxidation
	acetaldehyde	ethylene oxidation
polyol	ethylene glycol	hydration of ethylene oxide; synthesis from syngas; <u>synthesis from biomass-derived glycerol and cellulose</u>
	glycerol	<u>byproduct of biodiesel production</u>
ether	dimethyl ether	methanol dehydration; synthesis from syngas
carboxylic acids	formic acid	naphtha partial oxidation; methanol carbonylation; <u>biomass and CO₂ hydrogenation</u>
	acetic acid	methanol carbonylation; <u>sugars and alcohols bacterial fermentation</u>
ketones	acetone	cumene process
aromatics	phenols	cumene process
carbohydrates	sugars	<u>hydrolysis of lignocellulosic biomasses</u>
bio-oil	raw bio-oil	<u>pyrolysis of lignocellulosic biomasses</u>

Catalysis role in biomass derived molecules reforming

All the above described processes could not be possible without the use of specific catalysts. Clearly, among the aims of the state of art and of the future catalysts research in this field it is possible to fix some points: i) increasing the selectivity toward hydrogen production, reducing

Chapter 1. Introduction

the content of CO; ii) decreasing the operating temperature iii) obtaining fast kinetics.

An unresolved point of the biomass derived reforming concerns the reaction mechanism, that even in the simplest cases such as methanol, is still highly debated, due to the intrinsic complexity of the processes. These may involve elusive surface intermediates, structure sensitivity, non-negligible support or poisonous effects. Instead, the exhaustive comprehension of a reaction mechanism, possibly from a molecular basis, is the first step toward catalysts modification and optimization.

Since polyalcohols (polyols) and sugars are among the main species used in biomass processing, in this section we will focus on the state of art regarding the catalysts for the reforming of these feedstocks.

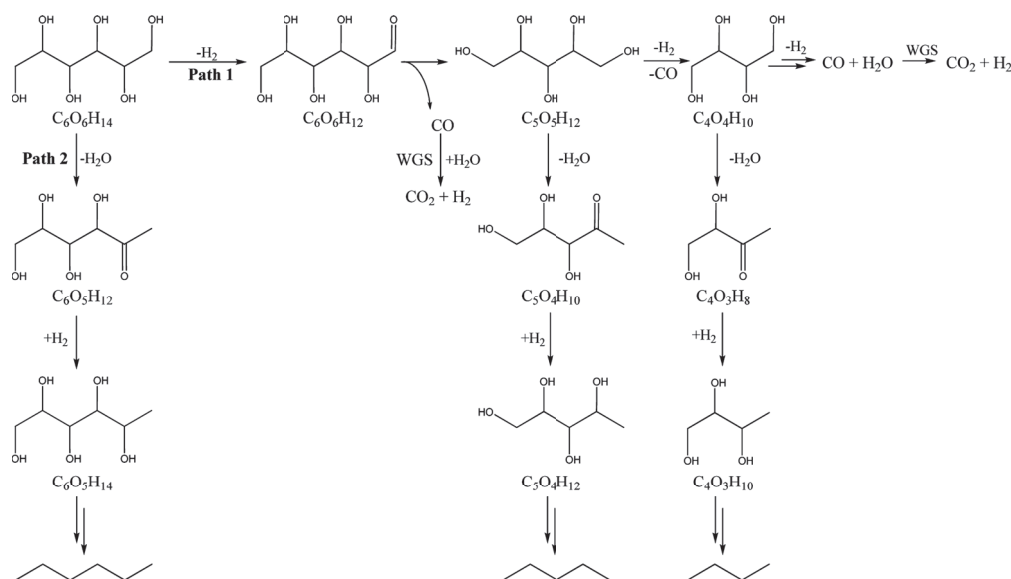
Countless studies have been carried out upon glycerol reforming, taken both as an easily obtainable raw material (it is indeed the major byproduct of transesterification of vegetable oils) and as model compound for more complex polyols [5, 6]. Supported noble metal catalysts – Pt, Re, Ru, Rh among all – are the most used for glycerol and in general for polyols reforming: several examples can be found in the literature regarding alumina [7], silica [8], ceria [9] or mixed ceria/alumina supported Pt catalysts [10], which operates at intermediate temperatures (600-700 K) with selectivity towards H_2 between 60 and 70 %. Remarkably better results were found for Ru based catalysts (Ru/ Y_2O_3) [11]. Particular attention was devoted to supported Ni catalysts: indeed, nickel is cheaper than common precious metals, but demonstrated high activity when supported on Al_2O_3 [12]. For this reason, alloying platinoids metal with nickel is a common practice for decreasing the overall price of the catalyst used. Moreover, the formed bimetallic catalysts usually show improved activity, often ascribed to promotional effects [7]. Really studied was the case of Pt-Re bimetallic alloys that demonstrated to have higher rates with respect to conventional monometallic catalysts [13]. This effect was explained invoking electronic modifications leading to weaker CO binding and faster WGS reaction. A major improvement on the understanding of this kind of effects, as well as reaction mechanisms was due to the increasing number of studies relying on Density Functional Theory (DFT) approaches, that for the aims of this dissertation will be more thoroughly addressed in section 1.3.

For its multiple advantages with respect to the other reforming methods, it is worth discussing more deeply APR. Introduced in 2002 by Dumesic and coworkers, APR is one of the most promising methodologies for the sustainable production of hydrogen [4].

The general scheme of the APR reaction, starting from sorbitol, is reported in Scheme 1.1. In an oversimplified picture, useful for understanding the main aspects of the reaction, APR has two main pathways: the first proceeds through dehydrogenation and decarbonylation (Path 1), leading to H_2 and shorter chain polyols, while the second (Path 2) proceeds through dehydration and leads to alkanes; it has to be noticed that the total amount of H_2 produced is increased by coupling APR with WGS, that is favoured at the same reaction conditions (~500 K, 15-50 bar). It is intuitive that the best catalyst for the reaction – if H_2 is the required product – should enhance the C-C bond cleavage (Path 1) and prevent C-O bond breakings (Path 2), being at the same time active toward WGS.

1.2. Biomass based sustainable hydrogen production

Supported Pt, Pd, Ni, Ru, Rh, Ir were previously tested by Dumesic and coworkers [14]. Pt was demonstrated to be active and selective toward the production of hydrogen starting from ethylene glycol. Even if less selective, Pt catalysts were used also for the direct conversion of glucose to hydrogen within the APR process. Anyway APR reaction mechanism is far to be completely understood, especially for molecules more complex than methanol or ethylene glycol. Recently, Godina *et al.* [15] demonstrated that, in Pt catalyzed APR of sorbitol, more than thirty liquid phase products can be formed, among major and trace species. These are the result of a really complex reaction network that may involve retro-aldol reactions along with more common dehydrogenation/decarbonylation steps.



Scheme 1.1 – Aqueous Phase Reforming reaction scheme, for a model polyol (sorbitol); Path 1 leads to H_2 and shorter polyalcohols through dehydrogenation and C-C bond breakings; Path 2 leads to alkanes *via* dehydration. Water Gas Shift is coupled with the reaction to convert the produced carbon monoxide to hydrogen and carbon dioxide.

To the complexity of the reaction pathway itself, that for simple molecules was modelled on different metallic plane and bimetallic surfaces by DFT [16, 17], support effects should have to be added as well; as an example the activity of Pt catalysts was demonstrated to be highly dependent on the support used, being Pt/ Al_2O_3 the most active. More acidic supports conversely seem to inhibit the reaction [18] whereas a correlation between the activity towards WGS and APR was also proposed [19]. In addition, the study of several bimetallic and non Pt-based catalysts was addressed in the literature. Pt-Re bimetallic alloys were demonstrated to have superior APR activity but lower H_2 selectivity [20]. Bimetallic Pt-Co alloy on single walled carbon nanotubes (SWNCT) instead showed high H_2 selectivity, but this was strongly influenced by the catalyst preparation method [21, 22]. Just as in the case of SR, nickel is a widely tested material as APR catalyst, both as companion metal in bimetallic nanoparticles or supported on Al_2O_3 , showing overall good performances. The addition of tin to nickel was demonstrated to be beneficial for increasing H_2 selectivity [9]. Raney nickel was tested as

Chapter 1. Introduction

catalyst for ethylene glycol, glycerol and sorbitol APR with results similar to those of alumina supported Pt. Moreover, the addition of Sn increased the H₂ selectivity with a mechanism similar to that already reported for rhenium [23].

The collection of these results, which obviously shows how promising and debated is APR, demonstrates also that there are still issues that prevent a complete technological transfer from research to industry. Apart from the already mentioned difficulties in the complete understanding of the reaction mechanism, the lack of catalyst hydrothermal stability is a major concern. Sintering, coking and leaching of the catalysts considerably lower their activity; hydroxylated supports, such as alumina, often lead to catalyst deactivation, facilitating sintering [3]. In this respect, it should be mentioned the ongoing research upon new catalytic supports able to prevent nanoparticles growth and synergically contribute to increase the catalyst activity and selectivity. As an example, boron nitride (BN) based systems, such as nanotubes (BNNTs) and nanosheets, have gained increased attention due to their unique mechanical, thermal and chemical resistance properties [24, 25]. Their use as support in catalysis was recently proposed by Meyer *et al.* in the gold and palladium catalyzed lactose oxidation [26] and they will be discussed as potential support for sub-nanometric Pd catalysts, in Chapter III.

The case of formic acid

It is worth treating formic acid (HCOOH, FA) like hydrogen vector as a special case. Indeed, along with more complex polyalcohols feedstocks, FA was proposed as good candidate for the sustainable production of hydrogen; FA is nontoxic and obtainable i) from biomass oxidation ii) as a by-product of different processes such as levulinic acid production [27] and in lesser amount from the same Aqueous Phase Reforming process. Direct FA Fuel Cells (DFAFC) were suggested as an alternative to conventional hydrogen fuel cells, avoiding the need of reforming processes and the limitations provided by storage and handling of H₂.

Just as in the case of polyols or sugars reforming, increasing the selectivity towards hydrogen is a major challenge in FA decomposition processes. Indeed, Pt and Pd, the most active catalysts for FA dehydrogenation and typical DFAC anode constituent, suffer considerably CO poisoning phenomena. In fact, nearly CO free hydrogen fuel has been already obtained with peculiar iridium, ruthenium and iron homogeneous catalysts [28, 29, 30], but the development of likewise active and selective heterogeneous catalysts would be an outstanding technological improvement.

It seems rather accepted that FA decomposition can occur following two main paths, *i.e.* dehydrogenation, involving the production of formate (HCOO) or carboxyl (COOH) intermediates, according to Equations 1.1 and 1.2, or dehydration (Equation 1.3), leading to carbon monoxide and water.

1.2. Biomass based sustainable hydrogen production



Solymosi *et al.* have tested a variety of supported metal nanoparticles (Pt, Pd, Ni, Ir) that showed interesting activity but rather poor selectivity toward H₂ – if compared with the fuel cells anodes CO tolerance – except for the case of Ir and Pt [31]. In opposition, Nishimura [32] and in more recent times Arenz [33] demonstrated that palladium, either alone or deposited on other metal surfaces, did not show any evidences of CO formation. Independently, Cai and coworkers [34] did detect CO during the electrochemical decomposition of HCOOH on a model Pd catalyst, through surface-enhanced IR absorption spectroscopy. These contrasting evidences demonstrate a general poor mechanism understanding, that only recently was improved by a powerful combination of experimental and computational studies. As an example, Choi *et al.* through electrochemical measurements and DFT calculations demonstrated that the presence of low coordination sites on Pd nanocrystal catalysts could enhance the activity toward FA oxidation, reducing the amount of CO produced [35]. Instead, Herron *et al.*, through periodic DFT calculations, concluded that, Ni(111), Ru(0001), Pd(100), Pt(100) and other transition metal surfaces could be considerably poisoned by CO when FA decomposes via a carboxyl mediated pathway [36]. These evidences were already observed in a number of experimental studies [37, 38, 39] that included in the list of CO selective surfaces also Pd(111) [40] and Ni(111) [41].

Despite the increasing amount of studies dealing with FA decomposition on metallic surfaces, scarce attention has been devoted to the ascending case of sub-nanometric catalysts, which have demonstrated unique activity and selectivity in various reactions such as the oxidative dehydrogenation of propane and propylene epoxidation [42, 43]. Parallely to the theoretical study of new bimetallic alloys [44], the choice of a sub-nanometer sized catalyst for FA decomposition could offer a new strategy for achieving high selectivity toward H₂ and low dehydration. Thus, the extremely undercoordinated sites shown by sub-nanometric clusters may lead to unexpected activity and/or selectivity. It is worth mentioning the recent work of Bi *et al.* who claimed for a CO free generation of hydrogen from FA catalyzed by highly active ZrO₂ supported gold sub-nanometric particles (ca. 1.1 nm) [45]. Moreover, according to their findings, the reaction mechanism could specifically involve the atoms at the cluster-support interface.

An overall view on computational catalysis

It is out of any doubt that over the past few decades most of the areas involving physical science experienced an extraordinary evolution, mostly characterized by the use of widely multidisciplinary approaches. The field of heterogeneous catalysis is a concrete example of such a maturation in conceiving scientific research itself. From the empiricism of the early developments (first decades of 1900s) in both catalyst synthesis and reaction mechanisms understanding, the rational design of catalyst with selected properties is nowadays possible. A tremendous contribution to these improvements was given by the integration of experimental and theoretical studies, mostly framed within DFT methods. Thanks to the continuous increase in computational power, the complexity and size of the systems that is possible to treat within first principle calculations has grown up toward the possibility of molecular events simulation at the catalyst interface.

The great importance of theoretical approaches in this field of investigation can be attributed to their double valence of explicative and predictive tools. One of the easiest but straightforward example is given by the possibility to calculate thermodynamic and kinetic quantities, as well as structural parameters, related to selected reaction intermediates. Despite this approach can be today defined quite a routinary task, it is still one of the most important resource in the case of complex reactions involving several competing pathways. Then, the contribution of this step is much more valuable considering that usually the identification of metastable surface intermediates can be extremely difficult within purely experimental methods. Starting from this point, more elaborated approaches have been developed, exploiting the knowledge of electronic, thermodynamic, kinetic and structural properties to develop specific relationships with predictive purposes; to give an example, in the case of metal catalyzed reactions, the construction of linear Brønsted-Evans-Polanyi (BEP) relationships starting from the knowledge of DFT computed activation and reaction energies allows one the fast prediction of activation barriers for selected surface molecular events, thus providing a useful tool for catalyst screening.

While in the next section both general concepts and specific examples regarding the connections of computational chemistry and catalysis will be presented, it is already rather intuitive from the few previous lines that the deep link between these two areas of expertise gave rise to a new well established research field, that is to say "Computational Catalysis".

From molecular events to the prediction of catalyst properties

Even the easiest catalyzed chemical process occurring in a laboratory scale reactor can be extremely difficult to model and rationalize. The reason lies behind both the number of simultaneous processes occurring and their different time and size domains. These spread from the macroscopic scale, where usually transport phenomena take place, to the microscopic scale, domain of molecular, thus electronic processes, which can be rationalized by quantum mechanical approaches. Between these two, at the mesoscopic scale, the influence that all the

1.3. An overall view on computational catalysis

elementary processes, accounted at the microscopic level, have in describing experimentally known quantities, such as Turnover Frequencies (TOF), can be evaluated through statistical (td-MC/kMC) or mean-field microkinetic modeling approaches. A schematic picture in which different methodologies are related to their proper time and size domain is presented in Figure 1.1.

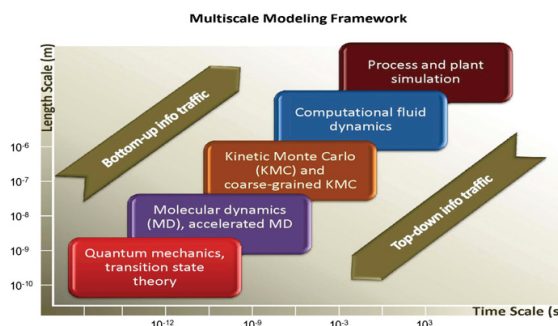


Figure 1.1 – Time-Size scales approachable with simulations and associated best suited computational methods for each domain. (Reproduced from Saliccioli *et al.* [46].)

Besides the intrinsic difficulty residing in the modeling of heterogeneous scales system, also its modification over the time should be taken into account: the properties of a catalyst are far to be static in any case. Aside from mechanical phenomena that are closer to the macroscopic size/time scale (such as catalyst *leaching*), surface coverage effects, implying adsorbate-adsorbate interactions, change in adsorption sites preferences (also involving catalyst-support interfaces) and reconstruction of the catalyst surface are relevant processes that might rule the description of the catalyst properties at the molecular and mesoscale size (all these processes are summarized in Figure 1.2).

However, through the combination of a well designed model and proper techniques, the most part of these difficulties can be overcome, resulting in straightforward examples of catalyst properties prediction starting from pure *ab initio* approaches. Despite the variety of methods, case studies and exceptions accounted in literature, generally all the techniques used for obtaining macroscopic (thus experimentally measurable) quantities from electronic calculations follow a nearly similar and hierarchical scheme:

1. Calculation of total energies. The calculation of reaction intermediates and transition state energies allows the identification of the minimum energy path;
2. Enthalpies and entropies of each reaction intermediate and transition state are evaluated at the specific experimental temperature; equilibrium (K) and rate constant (k) for each molecular event are calculated according to thermodynamics and transition state theory;
3. Construction of a suitable kinetic model. Starting from equilibrium and rate constants computed in the step above, a model is developed, including the significant reaction steps;

Chapter 1. Introduction

4. Calculation of target quantities, such as TOFs or apparent activation barriers to be compared with experimental results;
5. Improvement of the model. Several operations can be done for this purpose: inclusion of reaction steps that were initially discarded, accounting for adsorbate-adsorbate interactions or, if not used in the first attempts, dispersion interactions are the most common solutions.

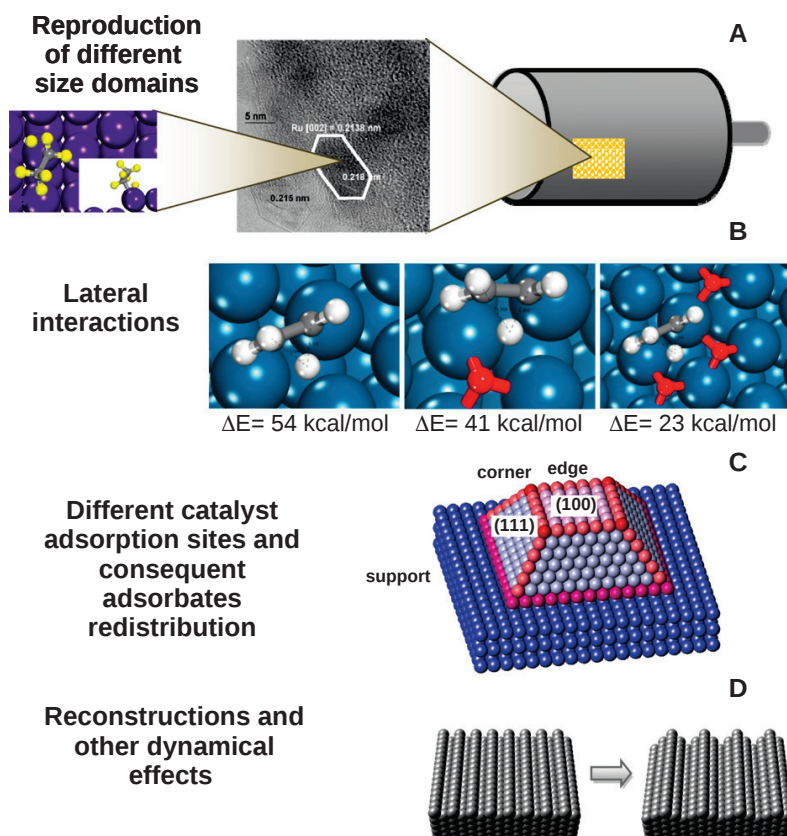


Figure 1.2 – Degree of complexity in heterogeneous catalyst modeling. A) Size domains to be reproduced span from molecular level events to reactors modeling; B) the calculated energies of molecular scale events depend on the surface occupation and lateral interactions could be non-negligible in several chemical systems: in the insets, activation energy variation for ethylene isomerization is shown depending on the number of co-adsorbed oxygen atoms. C) Adsorbates redistribute in a variety of catalyst adsorption sites: different exposed surfaces, catalyst-support interface, low coordinated sites; D) a missing row reconstruction of a (110) plane is presented as an example of dynamical modification of the catalyst. (Reproduced from Saliccioli *et al.* [46].)

If metal catalysts are involved, the first step is generally carried out within periodic DFT approaches, which are a good compromise between accuracy and computational efficiency.

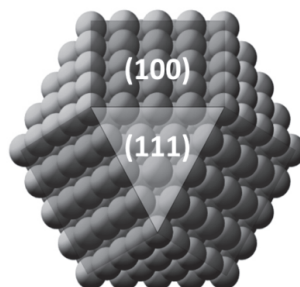


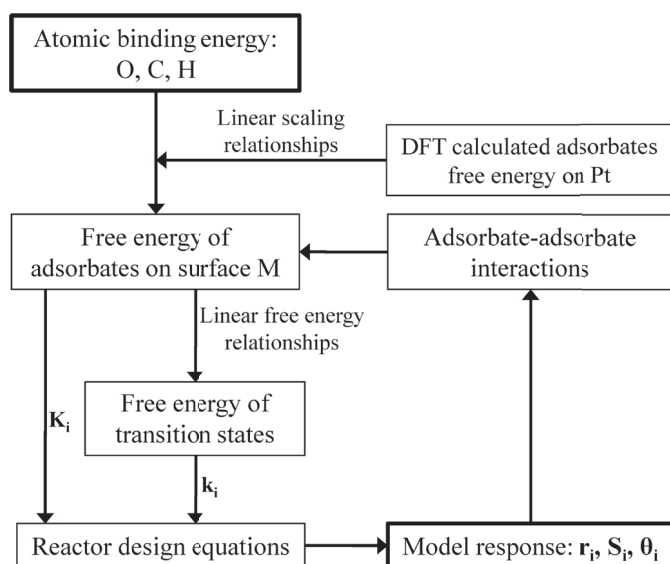
Figure 1.3 – A large metal nanoparticle model. Due to the size, the catalytic properties of the nanoparticle can be modeled taking into account each exposed surfaces, as (111) and (100) low Miller-index planes, with periodic DFT approaches.

The approximation of metallic catalysts as plain and stepped surfaces is generally enough to capture their main properties, due to catalyst morphology, as showed in Figure 1.3 ; sometimes this crude approximation may also apply to nanoparticles or clusters: due to nucleation, metal growth or sintering processes often occurring at the reaction condition used, the final properties of the catalyst can be described within periodic models. However, these cannot be applied when the catalytic properties arise from specific conditions, such as sub-nanometric sizes [47] or when there is a specific interest in the catalyst/support interaction.

The above reported scheme is exactly the procedure used to build microkinetic models starting from *ab initio* computed quantities. The predictive and explicative power of this approach is of course enormous; indeed, as a matter of fact, it represents the connection between quantities calculated through quantomechanical approaches and experimental TOF or other kinetic parameters. Nevertheless, for practical applications involving really complex surface reactions, such as polyols reforming on metals, the computational cost could result prohibitively high. A major improvement to the overcoming this huge limitation was given by the introduction of linear energy relationships and transition state scaling approach for the efficient calculation of reaction intermediates and transition states energy: Abild-Pedersen *et al.* [48] have elegantly demonstrated the subsistence of a linear correlation between the binding energy of a given hydrogenated adsorbate H_xA on a metal surface and that of the corresponding atom A (linear scaling relationships). From the pioneering works of Brønsted [49] and Evans and Polanyi [50] similar correlations were derived (BEP relationships), but linearly relating the activation energy with reaction energy. Of course these two combined approaches offer an outstanding tool for catalyst screening, starting from DFT calculations.

To give an example with a direct implication in biomass derived molecules, Saliccioli and Vlachos performed an extensive study of computationally driven catalyst screening for ethylene glycol decomposition [51]. In particular, a microkinetic model was developed exploiting a combination of state of art linear scaling and BEP relationships and introducing CO coverage

effects, according to Scheme 1.2. Indeed, relating the TOF of H_2 production with C and O binding energies, as showed in the contour plots reported in Figure 1.4, it was possible to find what is the parameter combination maximizing the activity toward H_2 . These combinations change from metal to metal and, as an example, a catalyst composed of a nichel overlayer on a Pt(111) surface approached the optimal values predicted by the model.



Scheme 1.2 – Kinetic parameter generation starting from the knowledge of atomic binding energies. The parameters r , S and θ represent reaction rates, selectivities and surface coverages that were used as target quantities for a kinetic model construction. (Adapted from Saliccioli *et al.* [51].)

However, the simple calculation of reaction intermediates and transition state structures and energies, despite not providing the same amount of information obtainable by more comprehensive approaches, like the microkinetic one, is often enough to draw significant conclusions on catalytic systems.

Case studies

This section is intended as a brief collection of computational or combined experimental and theoretical studies, where some of the key concepts that are used in the next chapters of this dissertation, were previously deepened. In particular, the studies have been selected on the basis of the methods employed or of the systems investigated.

Modeling of transition metal catalyzed dehydrogenation processes

In the last ten years a variety of computational works, aimed at understanding the competition between C-H, O-H, C-C and C-O bond breakings of small model molecules on transition

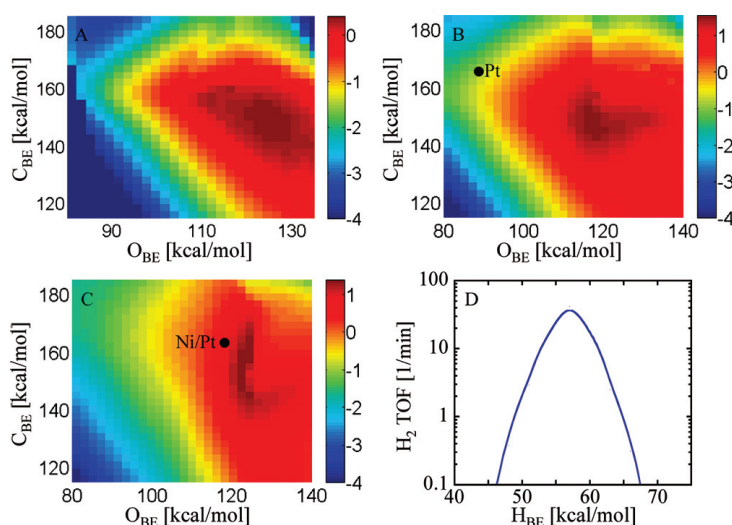


Figure 1.4 – Contour plots of predicted hydrogen TOF from ethylene glycol decomposition as a function of C and O binding energies (C_{BE} and O_{BE} respectively) at atomic hydrogen binding energies (H_{BE}) of A) 50 kcal mol⁻¹; B) 56 kcal mol⁻¹ and C) 62 kcal mol⁻¹; D) hydrogen production rate as a function of the H binding energy at fixed C and O binding energy. (Adapted from Saliccioli *et al.* [51].)

metals, arose. These were mainly based on periodic DFT calculations, that despite providing accurate insights into molecular events, have really high computational costs, especially for the calculation of transition states, necessary for reaction barrier estimations.

Nevertheless Ferrin *et al.* [17] have circumvented the problem through a combination of scaling and BEP relationships for the efficient calculation of both reaction intermediates and transition states deriving from ethanol decomposition on multiple metal surfaces. In particular, starting from the DFT energies obtained on a Ru(0001) surface, they postulated the possibility of calculating indirectly the binding energy of all the ethanol dehydrogenation intermediates on most of the transition metals. According to their findings, the C-C bond breaking resulted more *facile* at high level of dehydrogenation, that correspond, in most of the cases, to the direct loss of CO from a CH-CO fragment. Moreover the affinity of a specific metal surface toward carbon or oxygen atomic species (in terms of binding energy) could represent a selectivity descriptor toward C-C or C-O bond breakings. The preference of C-C cleavages with respect to C-O was previously demonstrated for a Pt(111) surface [52].

More recently Vlachos and coworkers [16] and Liu and Greeley [53, 54] have addressed the same topics using ethylene glycol and glycerol as starting molecules for their studies, respectively. In both cases, a substantial agreement upon the influence of dehydrogenation on the C-C bond cleavage was found: molecular events implying the shortening of polyalcohols chains should be possible only at high level of dehydrogenation, possibly with the loss of a carbon monoxide molecule. For glycerol, a first activation of the C-H bonds followed by the hydroxyl dehydrogenation was predicted while for ethylene glycol the O-H bond breaking was the initial preferred event. The competition between C-H, O-H and C-C bond cleavages, at different level of dehydrogenation, can be more easily shown plotting the Gibbs Free energy of

reactions for different reaction intermediates, as displayed in Figure 1.5.

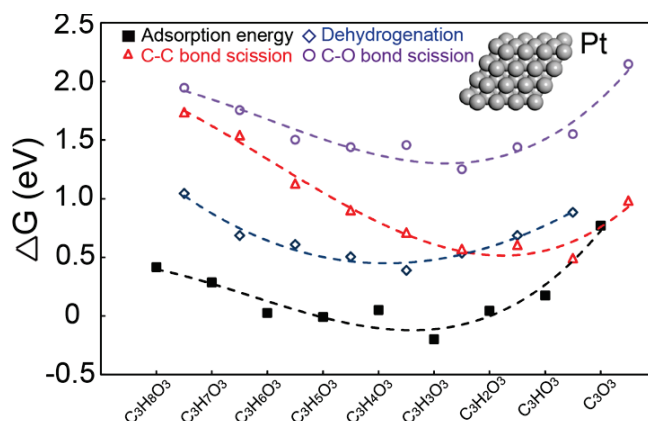


Figure 1.5 – Gibbs free energy for different molecular processes involved in the APR process on Pt(111) surface. C-C bond breakings were demonstrated to be competitive with dehydrogenation steps, only after the starting molecules showed high degree of insaturation. (Adapted from Liu *et al.* [53].)

Finally, it has to be remarked the importance of the introduction of solvent in order to gain a more realistic picture of the system. Indeed, it was demonstrated that water could have a non negligible influence in biomass oxidation, participating directly in dehydrogenation. Sautet and co-workers, analyzed the effect of hydrogen bond formation during the dehydrogenation of ethanol on Rh(111) [55]; they concluded that neighbouring water or co-adsorbed ethanol molecules, through intermolecular hydrogen bonding can assist the O-H bond cleavage and inhibit the C-H one. Naturally, depending on the combination of adsorbate/metal taken into account, the effect of hydrogen bonding can vary considerably. Cortese *et al.* [56] have demonstrated that the cooperative/competitive effect exerted by co-adsorbed water molecule on the polyalcohols adsorption on metal surfaces, strongly depends on the chemical nature of the metal. In particular while on Pd(111) the effect of hydrogen bonding on the adsorption of polyols seems more important, it has less effect on more "oxophilic" metals such as ruthenium or rhenium.

Structure sensitivity

Structure sensitivity of catalyzed biomass decomposition reactions was addressed by a number of studies, especially exploiting computational approaches. The catalysts exposed surfaces, that within periodic DFT calculations are usually modeled through low Miller-index planes, can show really different properties. Typically, open and stepped surfaces – such as (100) and (211) – are thought to be more reactive of more closed-packed arrangements – such as (111) planes – but this trend can vary from reaction to reaction.

Focusing on biomass derived molecules, Gu and Greeley [57] have studied the influence of a step in the ethylene glycol decomposition, by comparing the results obtained through periodic DFT calculations on Pt(111) and Pt(211) surfaces. The results indicated that, in both cases,

1.3. An overall view on computational catalysis

the reaction pathway should follow a double dehydrogenation route, leading to a CO-CHOH surface intermediate that can in turn evolve into carbon monoxide, strongly bound to the step, and into a hydroxymethylene fragment. The reaction seemed to proceed through the same mechanism in both cases; for this reason they concluded that APR on Pt should be structure insensitive, at least for the analyzed cases. Anyway on the Pt(211) surface, at APR conditions, lower activation barriers were generally found, also for C-O cleavages, suggesting that less oxygenated by-products could be found.

Structure sensitivity was deeply studied in the case of formic acid decomposition. According to Xia and coworkers [58] it is possible to synthesize Pd nanocrystals with selected shape and size, with facets representable as (111) and (211) Pd low Miller-index planes. DFT calculations showed that formic acid electro-oxidation on these two surfaces may be a structure sensitive reaction: the relative stability of carboxyl and formate surface intermediates is different on the two surfaces, with COOH preferred on (100) surfaces. This can have remarkable effects on the selectivity, since carbon monoxide was recognized to originate from COOH decomposition. In other words, the relative stability of these two intermediates on different catalyst exposed faces could be the key to finely tune the reaction selectivity.

Different conclusions were carried out for copper and gold [59, 60]. In the latter case, the HCOO pathway was recognized to be favoured irrespective of the surface considered; interestingly, mean-field microkinetic modeling showed that considering only (111), (100) and (211) planes may not be a suitable approach for correctly reproducing experimental TOFs, that can be majorly affected by the presence of even lower coordinated reaction sites.

In fact, the concept of structure sensitivity was rediscussed very recently by Crampton *et al.* [61] for magnesia supported sub-nanonmetric platinum clusters, evidencing the importance of low coordination sites and the impossibility of making extrapolation on the activity behaviour at the sub-nano scale. Finally, it is worth mentioning the approach exploited by Prestianni *et al.* [62] for the computational evaluation of structure sensitivity in alkynols and alkenols hydrogenation over palladium catalysts: the proposed methodology is based on the use of purposely shaped clusters exposing different low Miller-index planes as well as edge and corner at the same time, which allowed to study structure sensitivity effects, without relying on heavier periodic DFT calculations. This approach is extensively used along this dissertation.

Supported sub-nanometric catalysts

The deep connection between sub-nanometric catalysts and structure-activity relationships as well as their importance in processes related to biomass conversion emerges clearly from the discussion so far undertaken. Nevertheless, the study of sub-nanosized catalysts in this field has not been deepened.

A huge contribution to the development of sub-nano catalysts was given by Vajda and his group, that synthesized a variety of size selected metallic clusters then deposited on different supports through a soft landing procedure exploiting substrate biasing. Among a number of studies, concerning propane dehydrogenation and propylene epoxidation [42], it is inter-

esting to report the case of methanol synthesis from carbon dioxide, on Al_2O_3 supported sub-nanometric Cu_4 clusters [63]. Indeed, the corresponding reaction pathway shares some branches with the above mentioned formic acid decomposition and leads to the formation of carboxyl and formate intermediates. The coordination environment of the cluster was proposed as the main reason of a really high and unexpected activity of the catalyst.

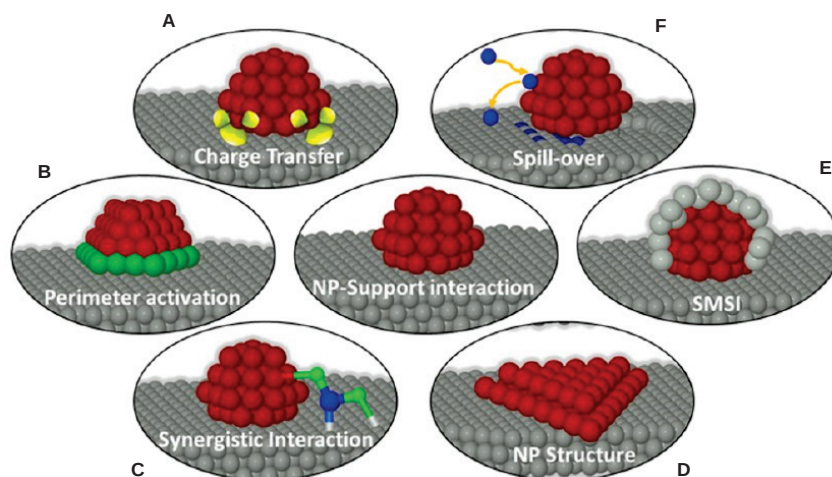


Figure 1.6 – Schematic representation of metal nanoparticle-support interaction effects: A) electronic charge transfers from/to the support; B) different catalytic properties of atoms directly interacting with the support; C) synergic interaction of the adsorbate with both the metal nanoparticle and support; D) reconstruction or templating effects exerted by the support; E) Strong Metal Support Interaction in the acceptance of migration of support atoms onto the active metallic phase; F) spillover of adsorbed species from the metal to the support. (Adapted from Ahmadi *et al.* [64].)

In fact, the unique properties of these materials depend on several, profoundly connected, factors; Hakkinen *et al.* [65] individuated three main effects that could rule the reactivity of sub-nanometric clusters: electronic effects, cluster fluxionality (reconstruction in presence of defects or adsorbates), dopants and impurities. Actually, these latter could be directly or indirectly related to solely electronic effects; in some extent, the briefly mentioned influence of supports can be as well ascribed to electronic effects, as nicely explained by Campbell in a revisitation of the well known Strong Metal Support Interaction (SMSI) [66]. It should be stressed that these effects could assume much more importance in the sub-nanometric regime since, for cluster of 6-10 atoms, the number of atoms directly in contact with the support could be a significant fraction of the total. Consequently, multiple processes involving metal-support interactions can contribute to the overall properties of the catalysts; in a really recent letter of Ahmadi *et al.* [64], the authors proposed the following list of important effects exerted by the support, schematically depicted in Figure 1.6:

- Charge transfer from the support (or *viceversa*). It is one of the more common phe-

1.3. An overall view on computational catalysis

nomena especially in the presence of support defectivity. Charge depletion from sub-nanometric metallic clusters to defective graphene, was demonstrated to be directly correlated to the adsorption energy of small probe molecules on the cluster itself [67]; conversely, the opposite charge transfer from MgO to Au₈ particles seems to be responsible of biatomic molecules activation [68];

- Perimeter activation and synergistic interactions. Due to their different environment, metallic atoms at the support interface could show different reactivity; this effect was proposed to explain the increased activity of ceria or titania supported Au nanoparticles in the WGS reaction or FA decomposition [45, 69]. Moreover, the vicinal support atoms could directly contribute to the reaction, providing adsorption sites for the reactants;
- Structural changes in nanoparticles. The geometry of metallic clusters *in vacuo* and when supported can change significantly. In a more general view, metal-support interactions may determine shape and size of the supported cluster and controlling factors in nanoparticles nucleation and growth phenomena.

The above presented concepts will be further discussed and contextualized, in the framework of boron nitride supported palladium catalysts, in the third chapter.

Aim of the thesis

This thesis, by means of computational approaches, is aimed at providing fundamental insights on different catalytic systems for the conversion of biomass derived molecules (1,2-PDO and FA). In particular a purposely shaped Pt cluster and a *h*-BN supported Pd₆ sub-nanoparticle were investigated as model catalysts. Indeed, both Pt and Pd are among the most employed metals for biomass reforming catalysts; moreover, the use of computational models representing plane surfaces or explicitly including a support well illustrates the main features of commonly used heterogeneous catalyst.

The aims of the work can be summarized as follows:

1. Assessing the catalytic properties of the investigated systems, in terms of activity and selectivity towards H₂ production;
2. Proposing a suitable reaction mechanism for the 1,2-PDO decomposition on a platinum catalyst, focusing on the competition between C-H, O-H and C-C bond cleavages and evaluating if and in what terms the process is structure sensitive;
3. Exploring the potential use of a selected BN supported sub-nanometric Pd cluster for the CO-free production of hydrogen from FA.

Finally it is expected to obtain a comprehensive picture of highly tangled reaction networks relying under the biomass reforming processes and to portray the key factors controlling the catalytic behaviour of the analyzed systems.

2 Platinum catalyzed 1,2-PDO decomposition

In this chapter the platinum catalyzed decomposition of 1,2-Propanediol (1,2-PDO), as model molecule for more complex polyalcohols, will be studied and discussed by means of DFT calculations. In particular, all the results that will be presented were obtained through a mutual collaboration with the Laboratory of Industrial Chemistry and Reaction Engineering of the Åbo Akademi University (AAU) of Turku (FI), where the Pt catalyzed 1,2-PDO aqueous phase reforming has been experimentally investigated. Anyway, only the computational part of the work will be discussed in this chapter recalling, when necessary, the conclusions drawn in the experimental counterpart.

The chapter is divided in two parts; the first deals with the decomposition of 1,2-PDO on a model Pt(111) low Miller-index surface; reaction intermediates and transition states for the decomposition process were calculated and on the grounds of these findings the most probable reaction path will be proposed; a specific part was dedicated to the evaluation of BEP type relationships for the C-H, O-H and C-C bond breakings studied. This could be used in future works for the efficient calculation of activation energies starting from pure thermodynamic quantities for larger polyalcohols on Pt.

In the second part the analysis was reproposed on a model Pt(100) surface, in order to discuss the structure sensitivity of the reaction, in terms of preference toward C-H or O-H bond cleavages, activity toward the C-C bond breakings and more generally, differences in the reaction mechanism.

It should be stressed that, while a variety of computational and experimental studies already addressed the decomposition of small biomass derived molecules, such as ethylene glycol, on Pt(111) (*vid.* Chapter I), limited attention has been devoted to other possible feedstock molecules, such as 1,2-PDO, even if it is an intermediate of glycerol reforming. To the best of our knowledge, the case of a Pt(100) surface as decomposition catalyst, has never been treated in the literature through computational methodologies.

Computational Details

All calculations were performed with the Gaussian 09 package [70], using the M06-L exchange-correlation functional which has been recognized to be efficient for the treatment of transition metal complexes as well as for the correct reproduction of dispersion interactions [71]. For all the reported calculations the Los Alamos LANL2 effective core potential and the corresponding double- ζ basis set was used for Pt atoms while, for lighter atoms, the D95 basis set with the addition of the LANL2dp polarization functions was employed.

Through a proper cut of the *fcc* bulk platinum lattice, a Pt₃₀ cluster showing both the (111) and (100) surfaces was obtained. Despite being a molecular cluster, this model should ensure the same sites topology as a periodic surface. In order to search for a cluster structure that, together with the lowest energy, would retain the initial symmetry without incurring into severe distortions, the cluster was fully relaxed trying different spin multiplicities. This resulted in the conclusion that a multiplicity of seventeen is the one that fulfills these criteria. This is in line with the findings of Goddard *et al.* on Pt clusters of comparable sizes [72]. Reaction intermediates and transition states were fully optimized using the same spin multiplicity, checking the nature of the stationary point on the potential energy surface by calculation and inspection of vibrational frequencies. All the energy values have been corrected for the zero-point vibrational contribution.

Except when specifically mentioned, the reported energies of the reaction intermediates are referred to the absolute energy value of the most hydrogenated species in the same reaction scheme, while the activation barriers are taken with respect to the reactant of the elementary step to which the transition state is associated.

Adsorption energies, ΔE_{Ads} , were calculated through the following equation:

$$\Delta E_{Ads} = E_{Tot} - E_{Pt} - E_{PDO} \quad (2.1)$$

where E_{Tot} is the total energy of the system made up of cluster and adsorbate, E_{Pt} is the energy of the Pt cluster and E_{PDO} is the absolute energy of 1,2-PDO. The obtained values were corrected for the basis set superposition error (BSSE), estimated by the application of the counterpoise method, as suggested by Boys and Bernardi [73].

Part I - 1,2-PDO decomposition on a Pt(111) surface

The adsorption energy of the 1,2-PDO on the Pt surface has been estimated to be $-46.9 \text{ kJ mol}^{-1}$. Oxygen belonging to the primary alcoholic moiety interacts atop with a Pt atom as shown in Figure 2.1, being their bond distance 2.51 \AA , while the secondary one, which acts as an intramolecular hydrogen bond acceptor, is placed at 3.40 \AA from the nearest metal atom. This is in agreement with previous findings suggesting that during adsorption of oxygenates on metal surfaces, the intramolecular hydrogen bond is very likely retained [56]. A similar conformation was found also by Gu *et al.* [57] and Kandoi *et al.* [74] in the case of the ethylene glycol on a Pt(111) surface. With the computational approach here chosen, the adsorption energy of ethylene glycol on Pt_{30} is $-43.3 \text{ kJ mol}^{-1}$, which suggests that, at least for the adsorption stage, the substitution of one of the hydrogen atoms with a methyl group does not have a significant influence. Further, ethylene glycol coordination geometry is very similar to that reported in the literature and also the calculated adsorption energy is in close agreement (-54.9 and $-35.7 \text{ kJ mol}^{-1}$ for the two studies cited above). This comparison revealed that the influence of the computational settings, as well as of the possible border effects, on the adsorption energetics are negligible.

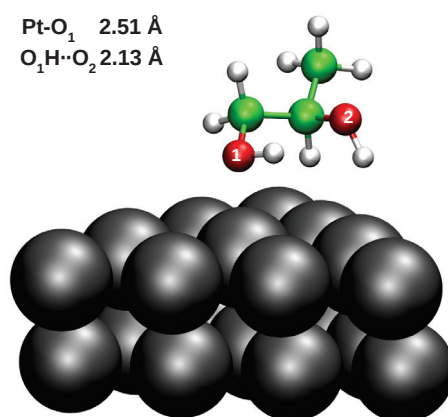


Figure 2.1 – Adsorption geometry of 1,2-PDO on the Pt_{30} (111) surface. Relevant geometrical descriptors are reported in the inset.

Kinetic of the first H_2 molecule loss

Step I

The 1,2-PDO shows five chemically different hydrogen atoms namely methylic (bound to the methylic carbon, C_m), primary (bound to the primary carbon, C_1), secondary (bound to the secondary carbon, C_2) and those of the primary (O_1) and secondary (O_2) hydroxylic moieties. These, in principle, trace five different dehydrogenation routes. Four of them are

Chapter 2. Platinum catalyzed 1,2-PDO decomposition

reported in Scheme 2.1 with respective activation barriers; the optimized geometries of the reaction intermediates produced in the first decomposition step are instead reported in the central panel of Figure 2.2. The fifth possible reaction path, corresponding to Cm-H bond breaking, shows an energy barrier of $126.5 \text{ kJ mol}^{-1}$; thus, it will not be treated at this stage of the investigation, since this barrier is too high if compared to those of the other paths.

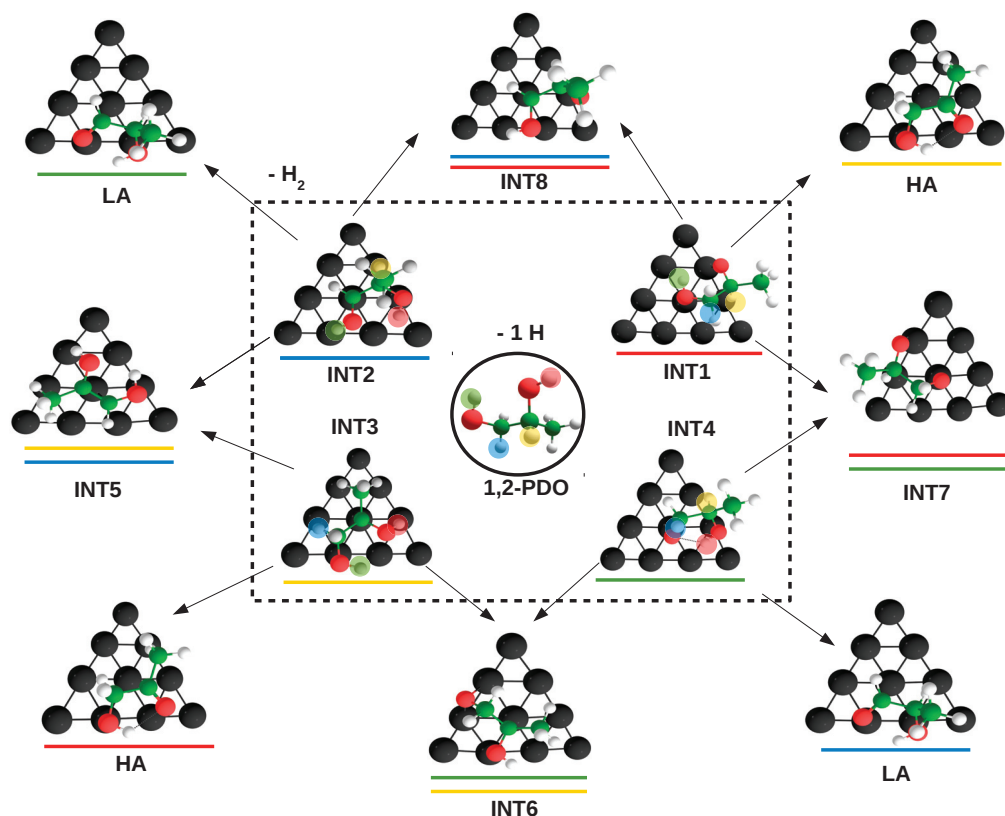


Figure 2.2 – Optimized geometries of intermediates produced in step I and step II. Each hydrogen was highlighted with a different color: green, the primary hydroxylic hydrogen; red, the secondary hydroxylic hydrogen; blue, the primary carbon hydrogen; yellow, the secondary carbon hydrogen. In this way, the color used for underline the structures in the outer panel shows what is the bond cleavage occurred to form a specific reaction intermediate.

The activation barrier for C1 dehydrogenation has been calculated to be 83.2 kJ mol^{-1} ; by comparing this value with the one associated to the Cm-H bond cleavage, a lowering of approximately 40 kJ mol^{-1} is revealed, which can be attributed to the effect of the hydroxy group in C1 and to a more favorable orientation of 1,2-PDO for the C1-H breaking. A slightly higher barrier of 93.4 kJ mol^{-1} was calculated in the case of C2 dehydrogenation. It is interesting to notice that the structure of the transition state associated to the C2 dehydrogenation shows close similarity to the adsorption structure of the 1,2-PDO, as shown in Figure 2.3B; thus the higher activation barrier required for this specific dehydrogenation, with respect to that of the

C1 carbon, cannot be ascribed to conformational changes or other structural rearrangements.

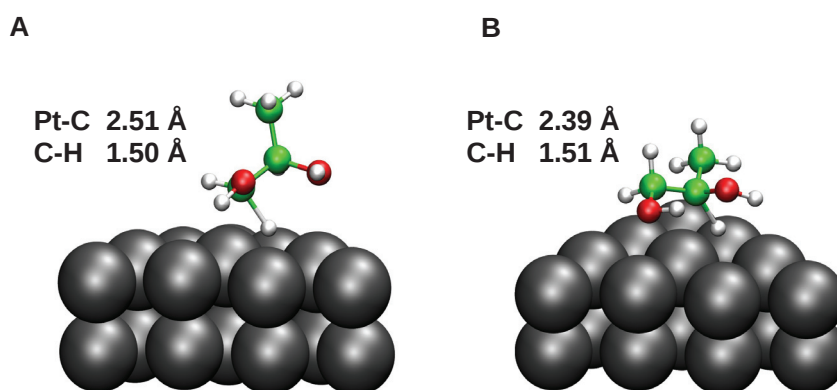


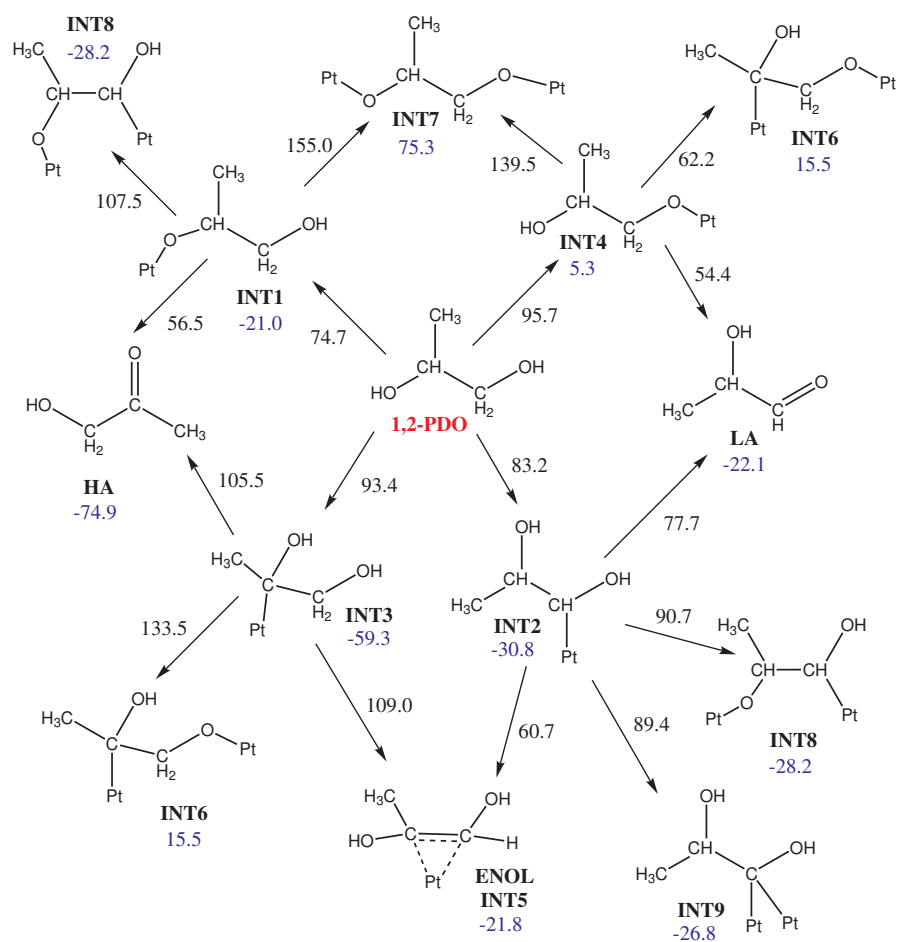
Figure 2.3 – Optimized structures of the transition states for the C1-H (A) and C2-H (B) bond breakings. Relevant geometrical descriptors, associated to the bond breaking event, are reported in the insets for each structure.

Dehydrogenation of O1 is nearly isoenergetic with that of C2, being the activation barrier being 95.7 kJ mol^{-1} . The most favorable kinetic pathway involves dehydrogenation of O2, requiring only 74.7 kJ mol^{-1} . Overall, the calculated activation barriers follow the order $\text{O2} < \text{C1} < \text{C2} \approx \text{O1}$. In fact, the exact quantification of these activation barriers seems to be at least controversial in the literature, which can be in part due to the differences in the approaches employed for their determination. As an example, taking into account glycerol on Pt(111), Liu and Greeley [54] have determined that the energy required for the first dehydrogenation step to occur, follows the trend $\text{C2} (75.5 \text{ kJ mol}^{-1}) < \text{O2} (79.4 \text{ kJ mol}^{-1}) < \text{O1} (82.1 \text{ kJ mol}^{-1}) < \text{C1} (97.2 \text{ kJ mol}^{-1})$. Note that the first three values are within a range of 6 kJ mol^{-1} . Independently, Chen *et al.* [75] calculated activation barriers for C1, C2 and O2 dehydrogenation of 36.3 , 37.2 and $101.9 \text{ kJ mol}^{-1}$ respectively. More recently, Rangarajan *et al.* have proposed, through an automatized approach based on the combination of both empirical and DFT derived correlation schemes, the following bond cleavage preference: $\text{C1} (20.9 \text{ kJ mol}^{-1}) < \text{C2} (49.5 \text{ kJ mol}^{-1}) < \text{O1} (74.1 \text{ kJ mol}^{-1})$ [76]. These latter findings seem to be in line with the energetic order found in our investigation, even if there is disagreement on the magnitude of the energy barriers.

Step II

The optimized structures obtained through the second dehydrogenation step, that is to say after the release of one H_2 molecule, are reported outside the central panel of Figure 2.2; each surface intermediate deriving from step I could in principle lead to four other intermediates, which are either surface species or stable products. However, each of these can be obtained as product of different pathways, depending on the order followed in the two consecutive dehydrogenation reactions. As an example, enolic intermediate (INT5), shown in Scheme 2.1, can be either obtained from INT2 and INT3. Moreover, with respect to Cm-H bond breaking,

Chapter 2. Platinum catalyzed 1,2-PDO decomposition



Scheme 2.1 – Reaction scheme for step I and II. Activation barriers (in kJ mol⁻¹), calculated with respect to the associated precursor, are reported in black, while the energy of each reaction intermediate or stable species, calculated taking the energy of the adsorbed 1,2-PDO as reference is reported in blue.

2.2. Part I - 1,2-PDO decomposition on a Pt(111) surface

only in the case of INT3 the methylic group could effectively interact with the metal surface. It has been estimated that this dehydrogenation requires $154.0 \text{ kJ mol}^{-1}$; thus, this particular C-H bond cleavage can be excluded from the reaction mechanism network. On the basis of these considerations, the number of intermediates involved in the analysis has diminished further.

Formation of hydroxyacetone (HA) from INT1 and enolic INT5 from INT2 are by far the most favorable routes, with activation barriers of 56.5 and 60.7 respectively, as reported in Scheme 2.1. The former is essentially a stable product in the liquid or gas phase and not a surface intermediate. For these latter species instead activation barriers of more than 100 kJ mol^{-1} have been calculated.

Reactivity of 1,2-PDO on palladium (111) surface and ethylene glycol on platinum (111) have been previously investigated by HREELS [77, 78]. Based on these data it is possible to argue that formation of 1,2-dioxy species is more likely to occur on Pd, than on Pt. Our calculations confirm that dehydrogenation of both alcoholic moieties is very unfavorable on the Pt surface. Indeed, the activation barriers of the molecular events leading from INT1 and INT4 to INT7 are the highest in the reaction path (*i.e.* 155.0 and $139.5 \text{ kJ mol}^{-1}$). For this reason, INT7 will be excluded from further analysis.

All the decomposition paths discussed so far involve an alternation of C-H or O-H bond cleavages. In fact, 1,2-PDO could as well undergo a double dehydrogenation on the primary carbon leading to INT9 *via* INT2. For the production of this latter intermediate an activation barrier of 89.4 kJ mol^{-1} was found; it is interesting to note that this process requires approximately 30 kJ mol^{-1} more than that consisting of the alternate C-H bond breaking leading to INT5. This trend is in agreement with the study of Chen *et al.* [75] which, for glycerol, estimates an alternate dehydrogenation path more feasible compared with that associated to consecutive dehydrogenations on the same carbon.

Energetics of intermediates in steps I and II

INT3 was evaluated to be the most stable intermediate of step I, being 59.3 kJ mol^{-1} more stable than adsorbed 1,2-PDO, followed by INT2, that is 30.8 kJ mol^{-1} more stable than its precursor. The exoergicity of the two molecular processes leading to INT3 and INT2 is reasonably due to substitution of C-H bonds with stronger C-Pt bonds. In INT3, whose structure is reported in Figure 2.4B, the dehydrogenated C2 is atop coordinated, with a C-Pt bond distance of 2.13 \AA . This interaction geometry is characterized by a tetrahedral arrangement that allows both the interaction of the primary hydroxyl group with the surface and the retaining of an intramolecular hydrogen bond in which O1 acts as donor. A similar geometry is adopted by INT1 (Figure 2.4A), except slightly longer intramolecular O \cdots H bond distance of 2.32 \AA , compared with the 2.30 \AA one found for INT3. The INT1 intermediate, originated from O1-H bond cleavages in step I, is 21.0 kJ mol^{-1} more stable than the reference state, while formation of INT4, derived from O2-H bond breaking, is slightly endoergic. Interestingly the energetic

differences between these two intermediates were generally not encountered in the previous studies on glycerol [74, 75]. Probably, this is a consequence of a better description of hydrogen bond interactions provided in the present work using the M06-L functional, which stabilizes INT1.

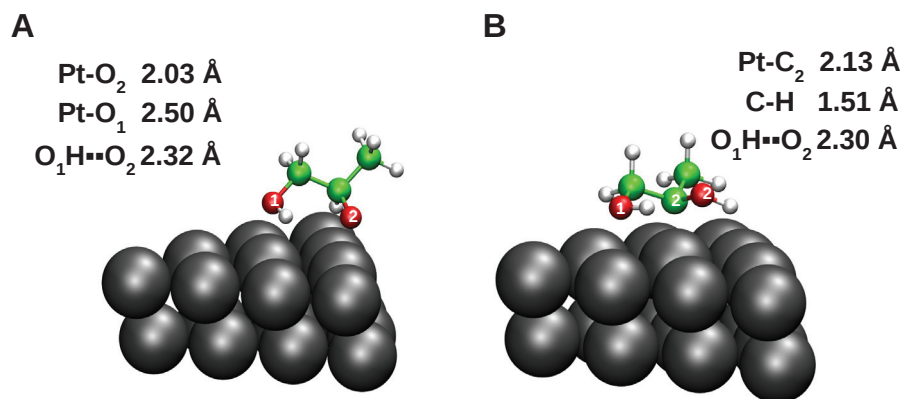


Figure 2.4 – Optimized structures of INT1 (A) and INT3 (B). Relevant geometrical descriptors are reported in the insets for each structure.

HA is by far one of the most stable product formed in step II, being 74.9 kJ mol^{-1} more stable than the reference state. INT8, lactic aldehyde (LA) and INT5 can be considered approximately isoenergetic, being respectively 28.2, 22.1 and 21.8 kJ mol^{-1} more stable than the adsorbed 1,2-PDO. Noticeably INT9, being the product of double dehydrogenation on the primary carbon, is stabilized by 26.8 kJ mol^{-1} . The remaining two intermediates, namely INT6 and the 1,2-propanedioxy species INT7, are the only to be less stable than the considered reference state, being respectively 15.5 and 75.5 kJ mol^{-1} higher in energy.

Further dehydrogenations

Almost all the reaction intermediates optimized in the previous molecular step were used as starting point for further investigations; HA, LA and INT7 are the only exceptions. The first has been experimentally recognized to be a by-product of the reaction in the experiments carried at at the AAU and so its dehydrogenation is unlikely to occur; even if its decomposition had an influence on the overall reaction mechanism, it would be equivalent to the study of the decomposition mechanism starting from different feedstocks and so independent from the original choice of the 1,2-PDO. The same discussion may be applied to LA, that has not been experimentally found, while INT7 is the only reaction intermediate whose formation was discarded, due to the prohibitive activation barriers as well to its thermodynamic instability. Accordingly to this premise, in Scheme 2.2 the suggested reaction paths for the C-H and O-H bond breakings of INT5, INT6, INT8 and INT9 are shown, while the optimized structures of their decomposition products are displayed in Figure 2.5.

The dehydrogenation paths of INT5 and INT8 are connected through the INTa intermediate,

while INTb links INT5 to INT6. INTd leads from INT5 to INT9, but the two paths were retained independent.

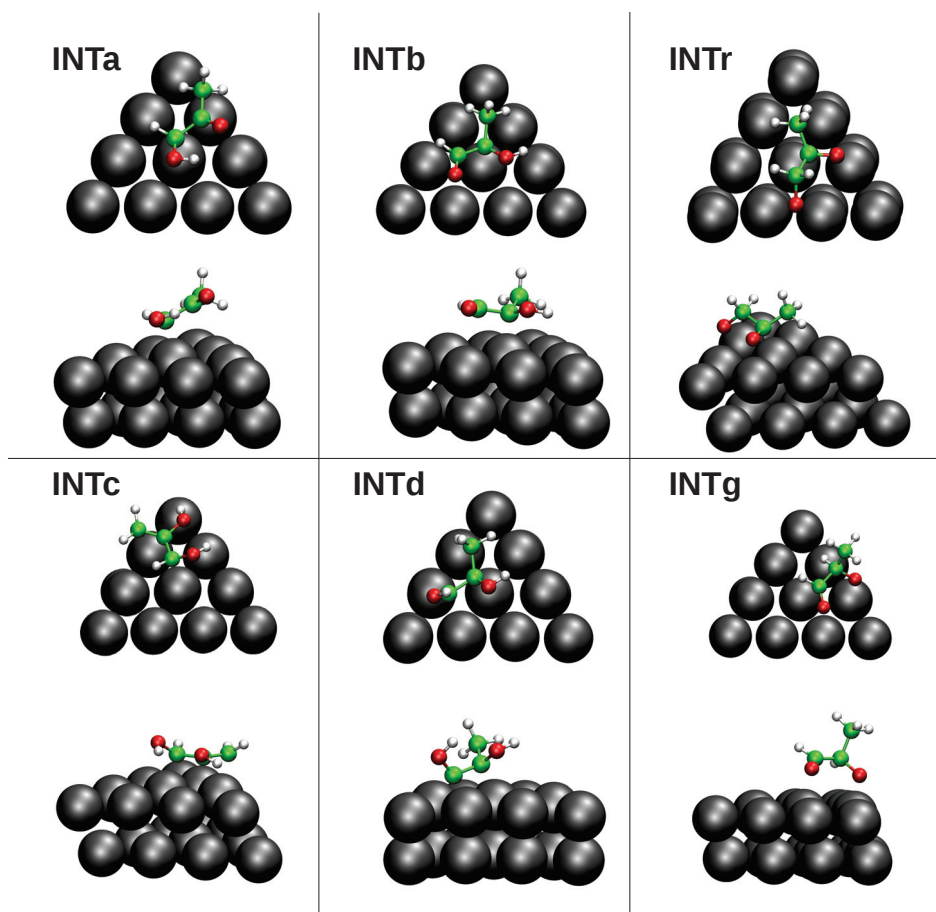
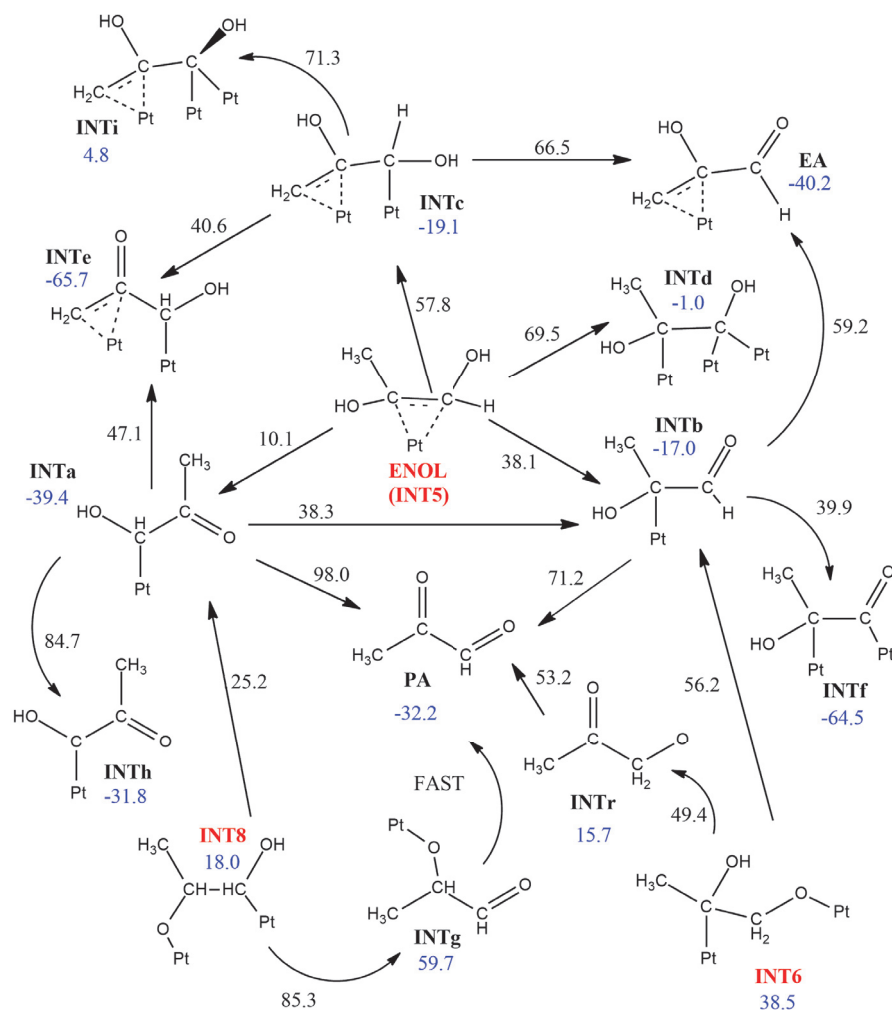


Figure 2.5 – Top (upper part) and side (bottom part) view of the optimized structures of all the reaction intermediates obtained through the removal of three hydrogens from 1,2-PDO.

The enolic INT5 has four chemically different hydrogen atoms, which could in principle lead to an equivalent number of intermediates, namely INTa-d. The former has been evaluated to be the most favoured product, with an activation barrier of 10.1 kJ mol^{-1} for the O-H bond cleavage of the secondary alcoholic group; the final product has been estimated to be 39.4 kJ mol^{-1} more stable than INT5. The activation barriers leading to the other intermediates were 38.1 (INTb), 57.8 (INTc) and 69.5 (INTd) kJ mol^{-1} . On the basis of these energy barriers, it seems highly probable that INT5 will proceed to successive dehydrogenation *via* INTa. This intermediate could be produced also from INT8 through the secondary carbon dehydrogenation requiring only 25.2 kJ mol^{-1} . It is worth noting that the same INT8 could otherwise lose its remaining alcoholic hydrogen to form INTg, its activation barrier being 85.3 kJ mol^{-1} . Even if conversion of INTg to pyruvic aldehyde (PA) should be really fast (the associated transition state is approximately isoenergetic with INTg) and the formed product is considerably more stable than INT5, we can rule out formation of PA. In effect both INTa and INT8 do prefer to

Chapter 2. Platinum catalyzed 1,2-PDO decomposition



Scheme 2.2 – Reaction scheme for further dehydrogenation steps starting from INT5, INT6 and INT8. Activation energies (in kJ mol⁻¹) calculated with respect the associated precursor are reported in black, while in blue is reported the energy of each reaction intermediate or stable species, calculated taking the energy of INT5 as reference.

follow other paths.

The formation of INTb from INT6 can occur through the primary C-H bond breaking, requiring the overcoming of an activation barrier of 56.2 kJ mol^{-1} ; otherwise INT6 may evolve also into PA through a connecting reaction intermediate, INTr, which is 15.7 kJ mol^{-1} less stable than INT5, taken as reference. The activation energy required for the conversion of INT6 to INTr is 49.4 kJ mol^{-1} while INTr can finally turn into PA through a barrier 53.2 kJ mol^{-1} high.

The INTa intermediate can follow four alternative routes. The primary carbon dehydrogenation, with an activation barrier of 84.7 kJ mol^{-1} , gives rise to INTb which is 31.8 kJ mol^{-1} more stable than INT5. Furthermore, contrary to what reported for the 1,2-PDO case, the Cm-H bond cleavage is much easier, showing an activation barrier of 47.1 kJ mol^{-1} to produce INTe, whose optimized structure is reported in Figure 2.6A. It is to notice that, as reported above, also the Cm-H bond rupture of INT5 shows a similar but slightly higher activation barrier of 57.8 kJ mol^{-1} . This is not a coincidence since in both cases the methylic group is directly bound to unsaturated C=C or C=O moieties, which may promote its dehydrogenation. Moreover, as reported in Figure 2.7, both the transition states leading to INTc and INTe respectively from INT5 and INTa, have quite similar structures characterized by the atop coordination of the primary carbon to a Pt atom and by a η^2 coordination of the remaining carbon atoms. This interaction geometry, along with the presence of the intramolecular hydrogen bond, should be behind the lower activation barriers associated to Cm-H bond breakings if compared to the same molecular event for the 1,2-PDO case. On the basis of this favorable geometrical arrangement on the Pt surface, INTe (see Figure 2.6A), resulted the most stable reaction intermediate appeared in this stage of the decomposition mechanism, experiencing a lowering in energy of 65.7 kJ mol^{-1} with respect to INT5. Finally, also in this case, the step leading to PA would be the least kinetically affordable, with an energy barrier of 98.0 kJ mol^{-1} .

Although the discussion so far seems to point out INTa as the starting point of the most important branch of the reaction, the decomposition path of INTb was investigated as well. Indeed, INTb can be also obtained from INTa through a rather easy intramolecular hydrogen shift, requiring 38.3 kJ mol^{-1} to occur. Three different dehydrogenation paths can be traced starting from INTb, leading to PA, enolic aldehyde (EA) and INTf (Figure 2.6B); activation barriers of 71.2 , 59.2 and 39.9 kJ mol^{-1} , respectively, have been calculated for their formation. Comparing the reaction mechanism branches originating from INTa and INTb it turns out that the formation of INTf is competitive with that of INTe.

Finally, with respect to the INT9 intermediate, only the dehydrogenation of the primary hydroxylic group was analyzed; indeed the O1-H cleavage would determine the formation of an intermediate showing a terminal C=O moiety that according to what concluded for INTf should be particularly favored. As presumable, a nearly inexistent activation barrier was found for this bond breaking, indicating a fast process, and the resulting intermediate, INT χ , is 52.0 kJ mol^{-1} more stable than its precursor.

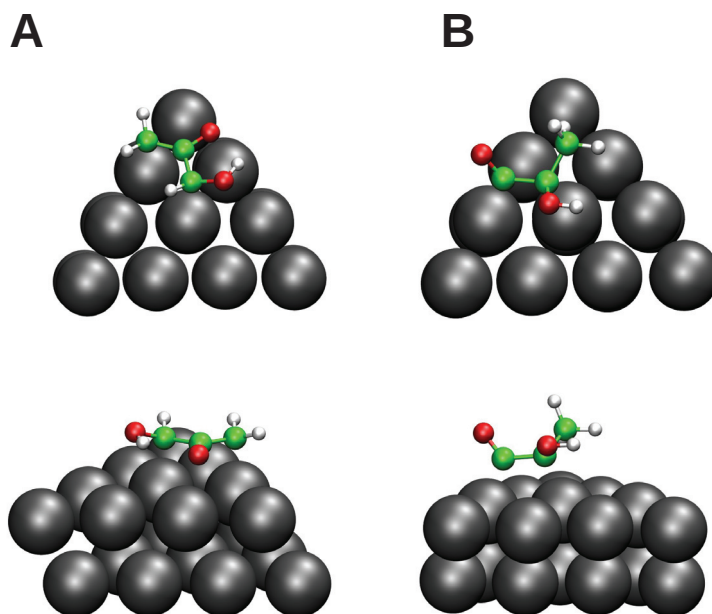


Figure 2.6 – Top (upper part) and side (bottom part) view of INTe (A) and INTf (B) optimized structures, key intermediates of the INT5 dehydrogenation reaction mechanism.

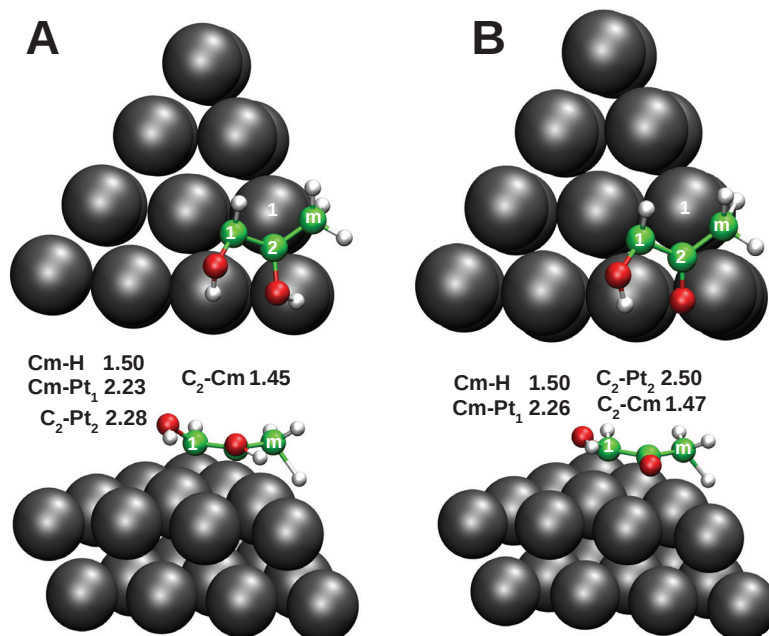


Figure 2.7 – Top (upper part) and side (bottom part) view of the transition state structures leading to INTc and INTe respectively from INT5 (A) and INTa (B).

The fate of INTe and INTf

Through the examination of the above mentioned decomposition steps, both INTe and INTf were shown to be among the easiest reaction intermediates to be formed. Indeed, all the others surface species or products at the same level of dehydrogenation, INT_h, INT_g, EA or INT_r, could be formed only through reaction branches that involve higher activation energies. Thus, it is worth discussing the fate of only these two surface species, as reported in Scheme 2.3.

Both the surface intermediates could contribute to the overall H₂ production with four more hydrogen atoms. However, with respect to INTe, only the primary carbon and hydroxylic group dehydrogenation were investigated, as these are thought to be more feasible events than that of the methylenic group. This is in agreement with previous studies suggesting that, in the case of ethanol, the methylene dehydrogenation occurs only when all other hydrogen atoms have been removed [79]. Activation barriers of 90.7 and 74.4 kJ mol⁻¹ were found respectively for C1-H and O1-H bond ruptures. Both these two processes are endoergic being INT_α and INT_β respectively 21.4 and 6.4 kJ mol⁻¹ less stable than INTe. Both the formed reaction intermediates would produce INT_ω, whose structure is reported in Figure 2.8B, but only the further dehydrogenation from INT_α was treated. The latter species is generated through the path with the lower activation barrier. Moreover the adsorption geometry of INT_β shows the hydroxylic hydrogen directed outward the surface forming an intramolecular hydrogen bond with the carbonylic oxygen; so INT_β is not prompt to be dehydrogenated. The last step, from INT_α to INT_ω, requires 70.7 kJ mol⁻¹ to occur, with the final product 15.3 kJ mol⁻¹ more stable than INTe.

In the case of INTf the methylic group points out from the Pt cluster, as shown in Figure 2.6B and it is stuck in this conformation due to the presence of two C-Pt bonds; therefore, only the secondary hydroxyl dehydrogenation has been considered. For this process, an activation barrier of 53.0 kJ mol⁻¹ has been calculated and the product, INT_j, displayed in Figure 2.8A, is nearly isoenergetic with INTf being only 2.4 kJ mol⁻¹ more stable.

C-C bond breakings

The C-C bond breaking is the key step that, in the case of APR process, leads from the starting feedstock to shorter polyols. Thus, the C1-C2 bond cleavage has been studied for several reaction intermediates selected from different reaction steps and therefore showing various dehydrogenation degrees (DeH). According to Liu and Greeley [54] the C-C bond cleavage should be more favorable if less hydrogenated compounds are considered. The results of our calculations, reported in Table 2.1, seem to confirm this evidence in some cases. Indeed, while the C-C bond breaking for INT₃ requires the overcoming of an activation barrier of 224.0 kJ mol⁻¹, the same process is much more affordable in the case of the enolic INT₅, with its activation barrier being 95.7 kJ mol⁻¹. Moreover, it is interesting to note that when a terminal C=O moiety is present in the intermediate, the rupture becomes easier, as evident by comparing E_a^{C1-C2} values of INT_χ and INT_b. However, even if the tendency of decreasing

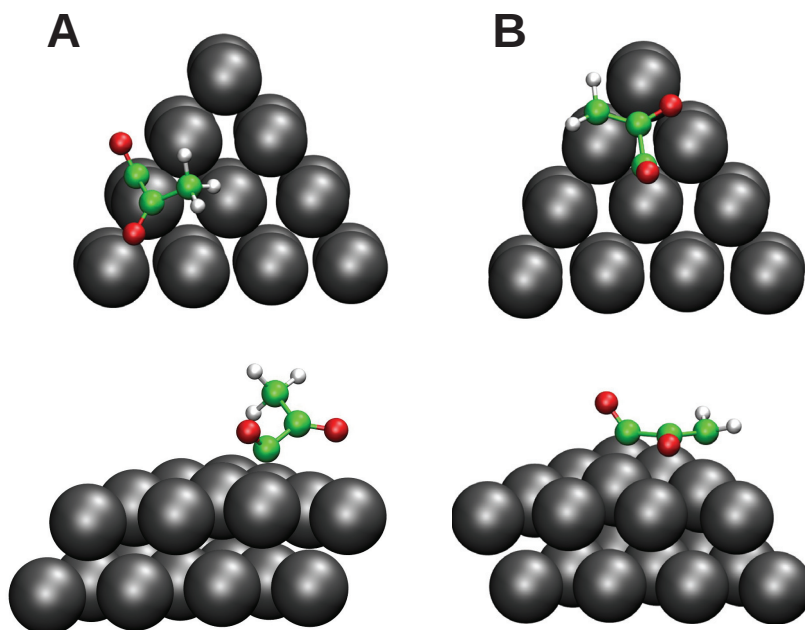
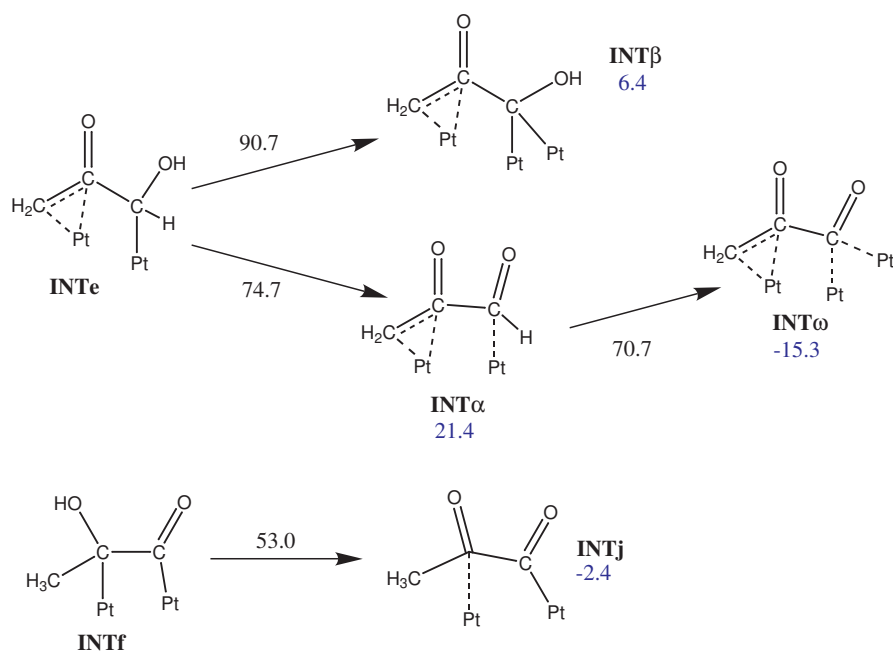


Figure 2.8 – Top (upper part) and side (bottom part) view of INT_j (A) and INT_ω (B) optimized structures, final products of dehydrogenation.



Scheme 2.3 – Reaction pathways for further dehydrogenation of INT_e and INT_f.

2.2. Part I - 1,2-PDO decomposition on a Pt(111) surface

the activation barrier for the C-C bond breaking along with the dehydrogenation degree is generally respected, it is difficult to find a direct relationship between the number of hydrogens lost and the energetic requirement for the reforming. As an example, taking into account INTa and INTb, which have the same dehydrogenation degree, reaction barriers of 109.6 and 132.3 kJ mol⁻¹ were obtained, both being higher than in the case of the more hydrogenated INT5. INTe and INTf can be considered as two limiting cases: despite having the same dehydrogenation degree, they have very different activation barriers, 211.3 and 63.6 kJ mol⁻¹. This large difference reflects the thermodynamic stabilization of INTe and INTf. In particular, due to its geometry and insaturations, INTe seems to be very well suited to fit in the fcc site offered by the surface (Figure 2.6). Hence the unexpected very high activation barrier may be explained considering that the C-C bond breaking would disrupt this stable conformation.

Table 2.1 – Activation barriers in kJ mol⁻¹ for the C1-C2 bond breaking of selected reaction intermediates showing different dehydrogenation degree (DeH). In the last four columns the activation barriers for the possible dehydrogenation processes occurring to selected intermediates are reported.

Intermediate	Formula	DeH	E _a ^{C1-C2}	E _a ^{O1-H}	E _a ^{O2-H}	E _a ^{C1-H}	E _a ^{Cm-H}
INT3	CH ₃ COHCH ₂ OH	1	224.0	133.5	105.5	109.0	-
INT5	CH ₃ COHCHOH	2	95.7	38.1	10.1	69.5	57.8
INTa	CH ₃ COCHOH	3	132.3	98.0	-	84.7	47.1
INTb	CH ₃ COHCHO	3	109.6	-	71.3	39.9	59.2
INT χ	CH ₃ CHOHCO	3	92.6	≈0	-	-	-
INTe	CH ₂ COCHOH	4	211.3	-	53.0	-	-
INTf	CH ₃ COHCO	4	63.6	74.7	-	90.7	-
INTj	CH ₃ COCO	5	48.8	-	-	-	-
INT ω	CH ₂ COCO	6	95.5	-	-	-	-

In addition to the analysis of the activation barriers trend as a function of the dehydrogenation degree, it can be very instructive to frame the C-C bond scissions within the energetic network of all the considered dehydrogenation reactions. Comparing the activation barriers for dehydrogenation reactions that a given intermediate can undergo with those for the C1-C2 bond scission, it is clear that only for INTf, INTj and INT ω the latter is a competitive and therefore feasible process.

The reaction mechanism

In the light of these findings, it is useful to review, in the form of potential energy curve (PEC), the entire reaction mechanism. In Figure 2.9 the PEC for 1,2-PDO dehydrogenation was reported. As a matter of fact, the distinction between reaction paths could be controversial in some cases, as it was demonstrated for the first dehydrogenation step. Thus, along with the path following the lowest activation barriers, these peculiar cases were as well reported; the other paths were directly discarded, due to their prohibitive energy requirement.

Apart the reaction path leading to HA from INT1, which has been already recognized to be

Chapter 2. Platinum catalyzed 1,2-PDO decomposition

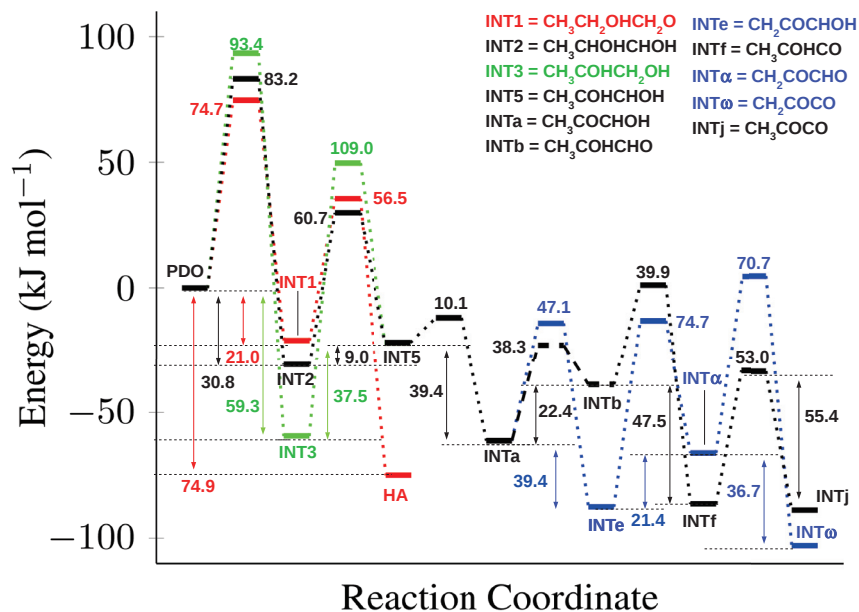


Figure 2.9 – PEC for 1,2-PDO dehydrogenation. Red lines are associated to the path leading to HA; blue lines, to the path leading to INT ω via INTe and black lines to the path leading to INTj via INTf. Dashed lines were used for the INTa to INTb tautomerization step. In the inset, the stoichiometry of each reaction intermediate is reported. The adsorbed 1,2-PDO on the Pt(111) face was abbreviated as "PDO" in the plot.

2.2. Part I - 1,2-PDO decomposition on a Pt(111) surface

among the most probable, the 1,2-PDO could convert to INT2 or INT3 overcoming similar activation barriers of 83.2 and 93.4 kJ mol⁻¹. It is worth noting that despite the slightly higher activation barrier for its formation, INT3 results 38.3 kJ mol⁻¹ more stable than INT2; this means that, if INT3 is formed, this could poison the surface, also in light of the very high activation barrier of 109.0 kJ mol⁻¹ required for its decomposition. However the path leading to INT5 from INT2 seems to be more affordable. A similar case was found for the conversion of INTa to INTb *via* hydrogen shift or of INT5 to INTb *via* dehydrogenation; the former process is endoergic, being INTb 22.4 kJ mol⁻¹ less stable than INTa, but requires a lower activation energy than the latter. In opposition, INTe is 39.4 kJ more stable than its precursor. However, at this level of investigation we can't predict which of the two factors has more weight in determining the reaction mechanism, especially since the activation barrier discussed are not too far from each other; for this purposes more comprehensive methods such as microkinetic modeling would be required.

In any case, following the path having the lowest activation barriers the reaction should proceed with this order of molecular events: 1,2-PDO → INT2 → INT5 → INTa → INTb → INTf → INTω being these two last reaction intermediates the only in which the C-C bond breakings becomes competitive with the dehydrogenation processes.

BEP relationships

The very high number of transition states required for having an overall picture of even small biomass derived molecules decomposition processes justifies the research of efficient strategies for activation barrier calculations. In this sense, BEP relationships could be a valuable guide for a fast screening of empirically obtained activation barriers, to be refined with more accurate approaches. For this reason, the correlation between the activation energy (E_a) of different bond breaking events with the formation energy (ΔE) of the associated surface reaction intermediates from its precursor, were evaluated for the here presented case. This relation was found to apply, even if with different extents, to C-H, O-H and C-C bond breakings, as shown in Figure 2.10A; a similar trend was also found considering C-H and O-H bond cleavages as part of the same data set (Figure 2.10B). Finally, the following equations were obtained through a linear regression procedure:

$$E_a = (0.77 \pm 0.14)\Delta E + (71.6 \pm 4.1) \quad (C - H) \quad (2.2)$$

$$E_a = (0.82 \pm 0.09)\Delta E + (76.8 \pm 4.6) \quad (O - H) \quad (2.3)$$

$$E_a = (0.79 \pm 0.12)\Delta E + (132.8 \pm 8.1) \quad (C - C) \quad (2.4)$$

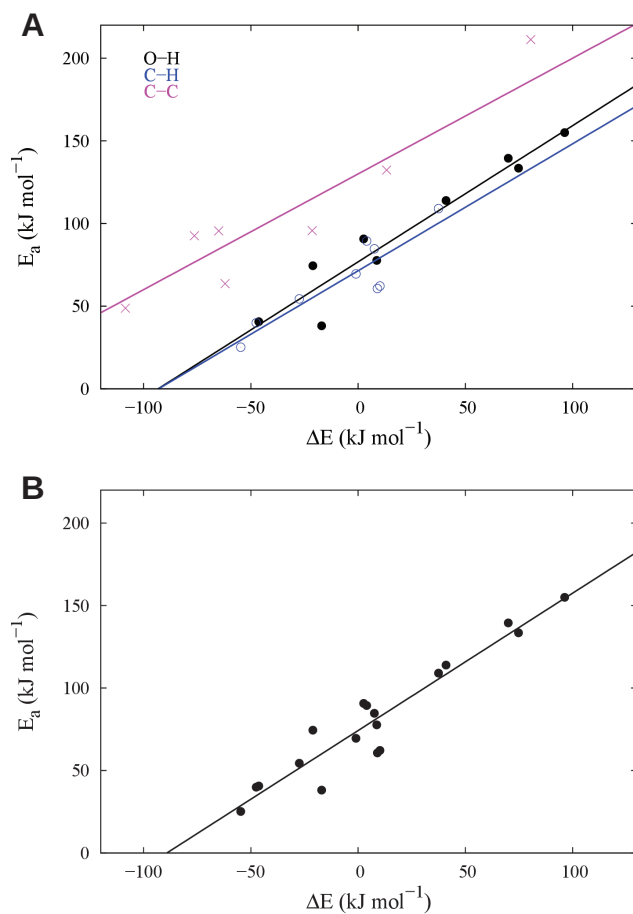


Figure 2.10 – BEP relationships developed for the second, third and fourth dehydrogenation steps. ΔE , the energy difference between the formed product and its precursor, correlates linearly with activation energy (E_a) required for the product formation. In panel A, BEP relationships for O-H (black), C-H (blue) and C-C (magenta) bond cleavages were reported; in panel B, the C-H and O-H bond breakings were used without distinction for the construction of a generic relationship for dehydrogenation. Lines are the result of a linear regression leading to Equations 2.2, 2.3, 2.4, 2.5.

2.2. Part I - 1,2-PDO decomposition on a Pt(111) surface

$$E_a = (0.83 \pm 0.07)\Delta E + (74.2 \pm 2.8) \quad (C - H + O - H) \quad (2.5)$$

According to Vlachos and co-workers [80], the correlation coefficient (R^2) has a minor role as quality descriptor for these kind of linear energy relationships while it is important to quantify how well they predict activation energies for selected molecular events. Despite more complex statistical analysis should be taken into account, probably not suited in this case due to the limited data collected, the comparison between calculated and predicted activation barriers could be used as a reasonable descriptor of the accuracy of the relationships found. In our case most part of the calculated deviations is smaller than the averaged mean unsigned error of 16.2 kJ mol^{-1} associated to transition states determination by the M06-L functional [81]. The highest errors were found in the case of C-C bond cleavages, but in the worst case scenario, the deviation was estimated to be 20.2 kJ mol^{-1} , only 4.0 kJ mol^{-1} higher than the reference value; thus this level of accuracy could be suitable for the purpose of fast initial screening of feasible bond scissions of more complex polyols.

Part II - 1,2-PDO decomposition on a Pt(100) surface

The adsorption energy of the 1,2-PDO on the Pt(100) surface has been calculated through Equation 2.1, resulting $-52.7 \text{ kJ mol}^{-1}$. This value can be compared with our previous study on the simulated Pt(111) plane, belonging to the same cluster, for which an adsorption energy of $-46.9 \text{ kJ mol}^{-1}$ was found. Thus, the adsorption energy seems not to change significantly on the two surfaces; a similar conclusion was also carried out by Tereshchuk *et al.* [82] that investigated glycerol adsorption on different low Miller-index Pt surfaces, finding a nearly equivalent adsorption energy on Pt(111) and Pt(100) at the PBE level.

The optimized structure, reported in Figure 2.11, shows the same features already found for the adsorption on the Pt(111) surface: only one of the two hydroxylic moieties, *i.e.* the primary, interacts with the surface and it is atop coordinated to a Pt atom with a Pt-O bond distance of 2.52 \AA .

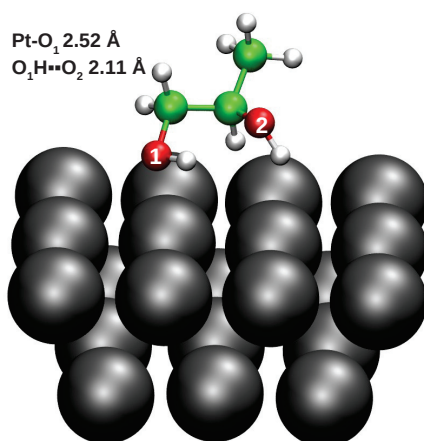


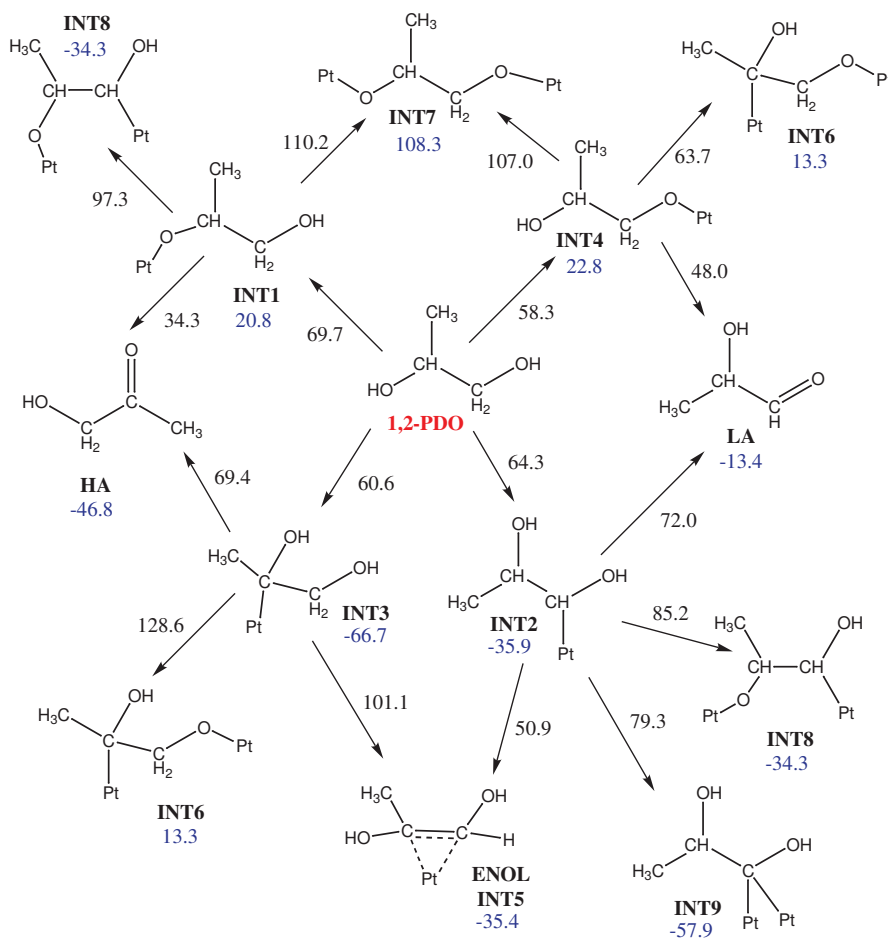
Figure 2.11 – Adsorption geometry of 1,2-PDO on the Pt₃₀ (100) surface. Relevant geometrical descriptors are reported in the inset.

1,2-PDO dehydrogenation can proceed through five different routes, corresponding to two O-H and three C-H bond cleavages; however, since the methylic group is not correctly orientated to interact with the surface, as it can be noticed from Figure 2.11, its dehydrogenation is really improbable. Moreover, we have already demonstrated in the first part of this chapter, that the presence of a hydroxylic group on the carbon atom is an important condition to lower the activation barrier for the C-H dehydrogenation. For these reason the methylic group reactivity will not be examined at this stage of the investigation.

First H₂ loss

1,2-PDO - 1H

The remaining four dehydrogenation paths involve the primary (O1) and secondary (O2) hydroxyl O-H bond breakings and the primary (C1) and secondary (C2) carbon C-H ones. The optimized structures of all the reaction intermediates arising from these dehydrogenation steps, are shown in Figure 2.12 while the associated reaction pathway is reported in Scheme 2.4.



Scheme 2.4 – Reaction scheme for step I and II. Activation barriers and energy differences between intermediates and the corresponding reference state, in kJ mol⁻¹, are reported respectively in black and blue.

The activation barriers for the first dehydrogenation were estimated to be 58.3 (O1-H), 69.7 (O2-H), 64.3 (C1-H) and 60.6 (C2-H) kJ mol⁻¹. It can be noticed that the energetic differences found are really contained: the lowest activation barrier, associated to the O1-H bond cleavage, leading to INT4, is only 11.6 kJ mol⁻¹ lower than the energy required for the O2-H bond breaking, having the highest barrier; from this latter, INT1 is formed.

For this reason, it is really difficult to make a prediction on the order in which the first molecular

event should occur. Therefore, it is reasonable that the stabilization of the produced surface species could have an important role in determining how the reaction proceed. It is interesting to notice how the intermediates formed by a C-H bond breaking, INT2 and INT3, are much more stabilized than those arising from a O-H bond cleavage, *i.e.* INT1 and INT4. In particular, INT3 results 66.7 kJ mol^{-1} more stable than the adsorbed 1,2-PDO (see Scheme 2.4), while INT2 only 35.2 kJ mol^{-1} . Conversely, INT1 and INT4 are respectively 20.8 and 22.8 kJ mol^{-1} destabilized with respect to the reference state. This evidence suggests that the formation of a Pt-C bond should be on the whole preferred to a Pt-O one. It is to notice that both INT3 and INT2 have really similar geometries, as shown in Figure 2.12: the dehydrogenated carbon atom is atop coordinated to a Pt atom, being the Pt-C bond length in INT3 2.13 \AA and 2.08 \AA in INT2; these coordination modes allow the oxygen bound to the vicinal saturated carbon to interact with the surface, showing a Pt-O bond distance of 2.48 \AA in the case of INT3 and 2.51 \AA for INT2.

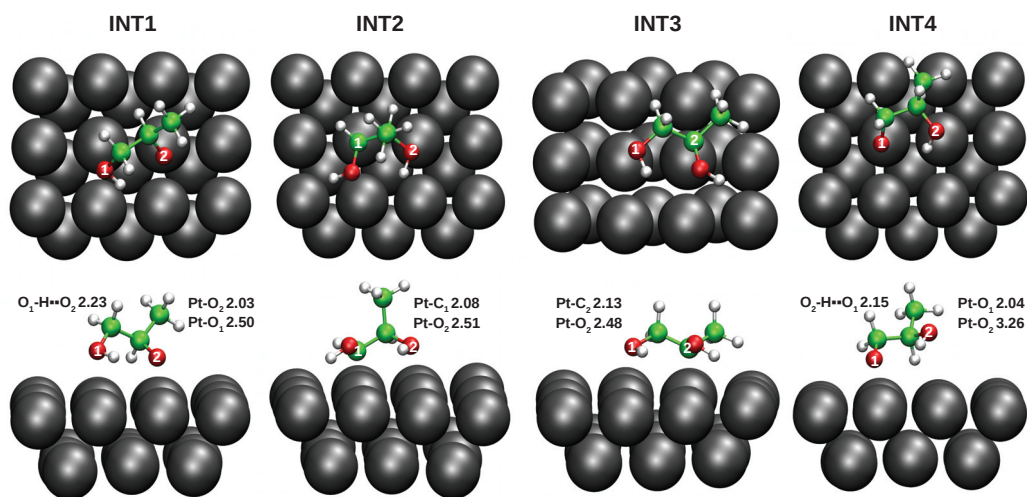


Figure 2.12 – Top (upper part) and lateral (bottom part) view of the optimized geometries of INT1-4 on the Pt(100) surface. Relevant geometrical descriptors are reported in Å units.

1,2-PDO - 2H

Among the products obtainable by a double dehydrogenation (*i.e.* the loss of a H_2 molecule) there are two stable species, hydroxyacetone (HA) and lactic aldehyde (LA), and five surface intermediates (INT5-INT9) whose optimized structures are reported in Figure 2.13. Just as in the case of the Pt(111) model previously described, each surface intermediate can be obtained by at least two precursors since it could be formed through consecutive C-H and O-H (or *viceversa*) bond cleavages. The only exception is INT9, that instead is obtained through a double dehydrogenation from the primary carbon of 1,2-PDO, being INT2 its precursor. This specific surface intermediate is the most stable among the double dehydrogenated surface

2.3. Part II - 1,2-PDO decomposition on a Pt(100) surface

species, being stabilized by 57.9 kJ mol^{-1} with respect the reference state. After this, it is possible to find in the order, HA ($\Delta E = -46.8$), INT5 ($\Delta E = -35.4 \text{ kJ mol}^{-1}$), INT8 ($\Delta E = -34.3 \text{ kJ mol}^{-1}$) and LA ($\Delta E = -13.4 \text{ kJ mol}^{-1}$). The remaining two surface intermediates, *i.e.* INT6 and INT7, are the only two to be less stable than the adsorbed 1,2-PDO, confirming that the formation of alkoxylates on Pt is not a favoured process. This is in agreement with the findings reported in the previous part of the chapter, dealing with the Pt(111) surface.

As regard the activation barriers for the elementary steps giving rise to the above discussed intermediates, they can be roughly divided in three different groups: the lowest activation barriers were found for processes leading to stable products, that is to say HA from INT1, requiring only 34.3 kJ mol^{-1} and LA from INT4, requiring 48.0 kJ mol^{-1} ; similarly, the formation of INT5 from INT2 requires the overcoming of an activation barrier of 50.9 kJ mol^{-1} . Average activation barriers, ranging from 63.2 to 85.2 kJ mol^{-1} were found for the formation of INT6, INT8 and INT9; instead, regardless the path chosen, the formation of INT7 seems to be kinetically unfavoured, since from INT4 and INT1, it would require 107.2 and $110.2 \text{ kJ mol}^{-1}$ respectively.

Second H₂ loss

Apart from those arising from the methyl dehydrogenation, so far, all the reaction intermediates and transition states associated to dehydrogenation steps were investigated. Nevertheless, the same procedure can be hardly applied to all the stable products or surface species formed in the step before: indeed, each intermediate can undergo at least two different dehydrogenation steps, prohibitively increasing the computational efforts required. Instead, as previously done for the Pt(111) case it is more efficient to make a selection of the most probable reaction intermediates, that will be used as starting point for the successive dehydrogenation steps.

Since all the activation barriers for the formation of INT1, INT2, INT3 and INT4 can be considered nearly equivalent, it is convenient to focus only on the reaction thermodynamics, as done previously in similar cases [57]; accordingly, the reaction flux should pass through the only two stabilized intermediates, *i.e.* INT2 or INT3. From INT3, HA formation should be easier than INT5 or INT6 production; this is in agreement with the experimental studies, performed at the AAU, showing that HA is a major by-product of 1,2-PDO APR; however, shorter carbon chain species were found as well and, according to the literature [53] and to the findings previously collected, the C-C bond breaking should be activated only for highly dehydrogenated compounds. Thus, it is probable that the reaction could further proceed to the formation of INT5 through INT3, despite the rather high activation barrier of $100.1 \text{ kJ mol}^{-1}$ required. Otherwise, following the INT2 path, INT5 could be formed overcoming a more affordable activation barrier of 50.2 kJ mol^{-1} . In spite of a higher activation barrier, the stability of INT9 with respect to the other reaction species, suggests that its formation cannot be *a priori* excluded. Conversely, LA has not been experimentally found among the products, while the formation of INT8, despite being as stable as INT5, is less kinetically

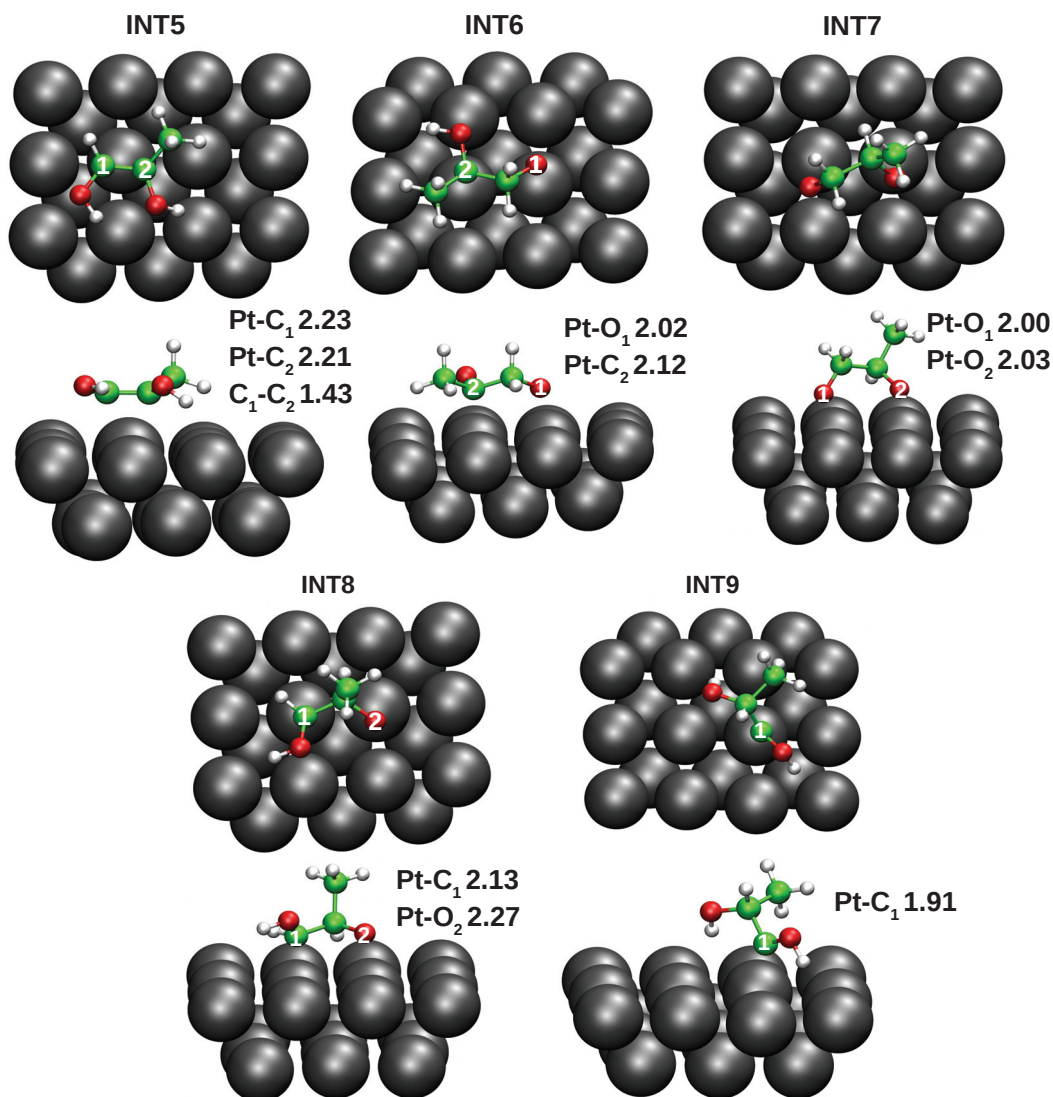


Figure 2.13 – Top (upper part) and lateral (bottom part) view of the optimized geometries of INT5-9 on the Pt(100) surface. Relevant geometrical descriptors are reported in Å units.

2.3. Part II - 1,2-PDO decomposition on a Pt(100) surface

favorable. Therefore, in agreement with these considerations HA, INT5, INT9 should be the most probable products; however for the same motivations already explained in the first part of the chapter, HA dehydrogenation was not treated. Thus, only INT5 and INT9 will be further investigated.

1,2-PDO - 3H

All the reaction intermediates deriving from the loss of one hydrogen atom from INT5, are reported in Figure 2.14, while the entire reaction path is displayed in Scheme 2.5. Since the methylic group shows a better orientation for the effective interaction with the Pt surface, if compared with the intermediates in the previous reaction scheme, this time the Cm-H bond breaking was included in the dehydrogenation path. Hence, four different products can be obtained, namely INTa (CH_3COCHOH), INTb (CH_3COHCHO), INTc ($\text{CH}_2\text{COHCHOH}$) and INTd (CH_3COHCOH). INTc resulted the most stable among this series of surface intermediates, being 34.3 kJ mol^{-1} more stable than INT5 and almost isoenergetic with INTb. Similarly to what found previously for INT2 and INT3, the stabilization of INTc may be ascribed to the formation of another Pt-C bond; in its fully relaxed structure INTc shows a η^2 coordination of the primary and secondary carbon atoms to a Pt one, while the newly dehydrogenated methylic group interacts atop with a surface atom, being the Pt-Cm bond distance 2.08 \AA .

However, the direct formation of INTc and INTb from INT5 requires activation barriers of 103.4 and 95.5 kJ mol^{-1} respectively. Instead the production of INTa should be kinetically more favorable, due to its low activation barrier of 26.0 kJ mol^{-1} . It is worth mentioning, similarly to what found on the Pt(111), the possibility of a tautomerization mechanism leading from INTa to INTb and requiring 30.2 kJ mol^{-1} ; thus it's reasonable that INT5 could convert to INTb, passing from INTa.

Parallely to the above presented path, also the decomposition of INT9 can lead to reaction intermediates with the same level of dehydrogenation. In particular, on the grounds of the findings collected for the Pt(111), only the primary oxygen dehydrogenation was investigated in this case, since the formation of a terminal CO species has been demonstrated to be favoured. Indeed, the transition state energy associated to this bond breaking, was found almost isoenergetic to INT9, in the limit of 4 kJ mol^{-1} . This means, that the activation barrier associated to the O1-H dehydrogenation is so low that the conversion should occur really fast, alike what concluded for the formation of pyruvic aldehyde in our previous study. The product formed, INT χ , is 18.9 kJ mol^{-1} more stable than its precursor INT9.

1,2-PDO - 4H

Among all the products of the INT5 double dehydrogenation, INTe, INTf, INTg and the pyruvic aldehyde, PA, were optimized on the surface. Relaxed structures of the surface intermediates are reported in Figure 2.15; in fact, as previously seen in Part I also enolic aldehyde could be

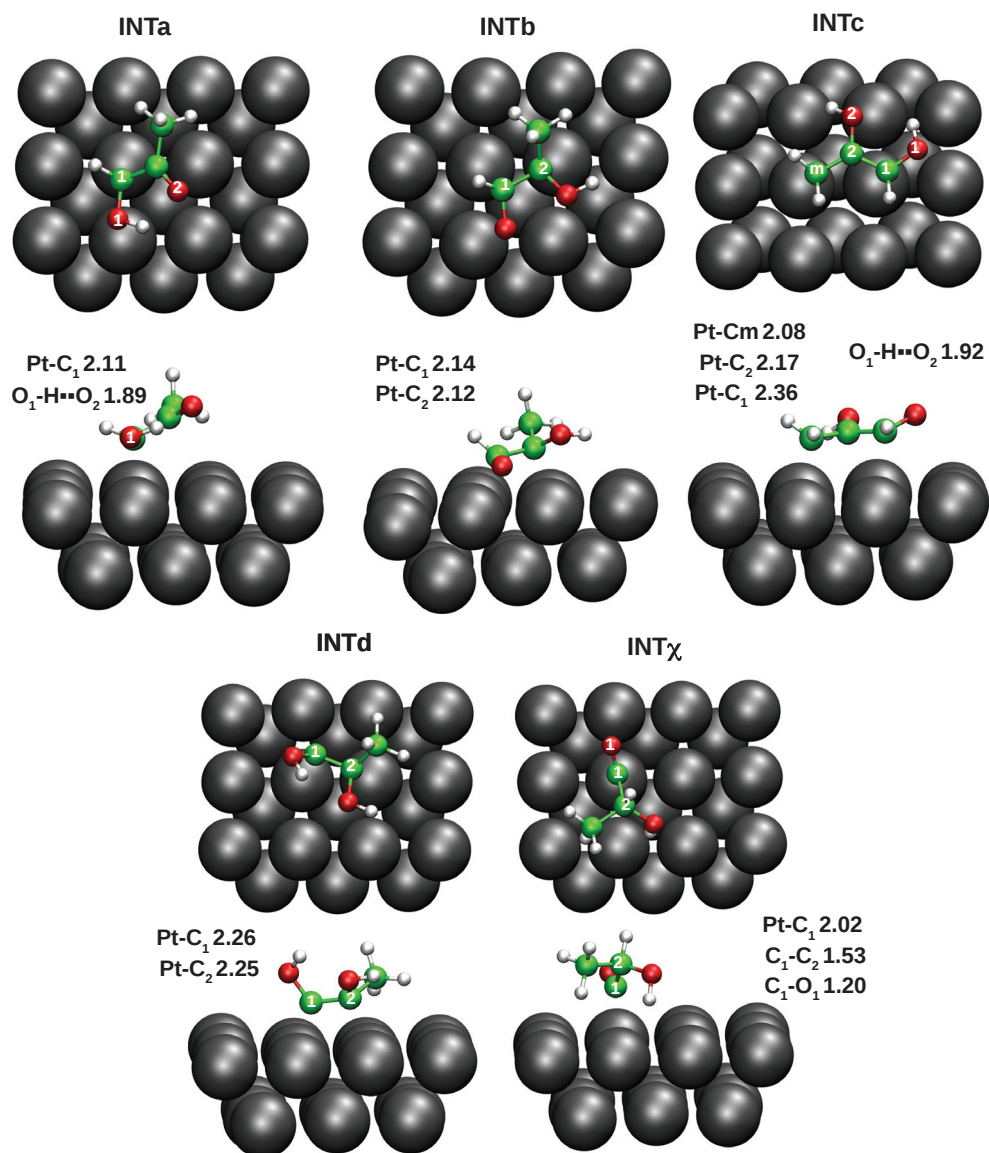
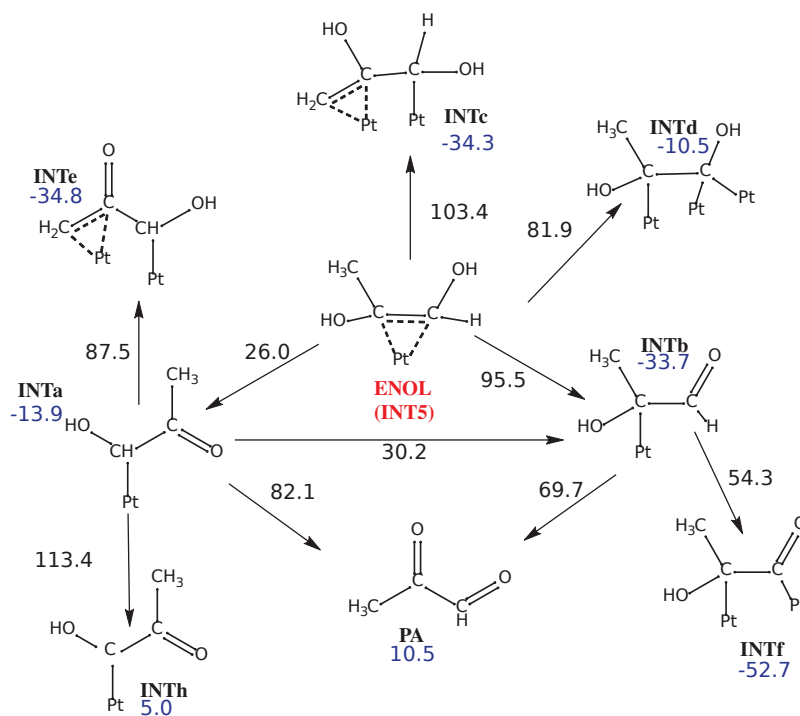


Figure 2.14 – Top (upper part) and lateral (bottom part) view of the optimized geometries of INTa-d and INT χ on the Pt(100) surface. Relevant geometrical descriptors are reported in Å units.

2.3. Part II - 1,2-PDO decomposition on a Pt(100) surface



Scheme 2.5 – Reaction scheme for step I and II. Activation barriers and energy differences between intermediates and the corresponding reference state, in kJ mol^{-1} , are reported respectively in black and blue.

Chapter 2. Platinum catalyzed 1,2-PDO decomposition

in principle formed from INTc or either INTb. However, since the formation of INTc has the highest activation barrier found in Scheme 2.5 and the methylic group of INTb is not correctly oriented to interact with the surface, we did not investigate the possibility of EA formation. For the same reason, the surface species formed by the INTc primary carbon dehydrogenation, presented for the Pt(111), has not been currently included in the study.

INTf, which shows a totally dehydrogenated carbon, is the most stable reaction intermediate presented in Scheme 2.5; this is in agreement with the general trend observed by Liu *et al.* for glycerol decomposition on a Pt(111) surface [53]. INTe is instead slightly less stable, but still its formation from INTa or INT5 remains exoergic. INTb instead is 5.0 kJ mol⁻¹ less stable than the reference state. Also the formation of PA seems to be not thermodynamically favoured, being 10.5 kJ mol⁻¹ less stable than the adsorbed INT5. Moreover, both PA and INTb have higher activation barriers if compared with that for the formation of INTf, which requires 54.3 kJ mol⁻¹ to be formed. INT ρ , whose structure is reported as well in Figure 2.15, is instead the product of INT χ decomposition. This surface intermediate is 29.5 kJ mol⁻¹ less stable than its precursor.

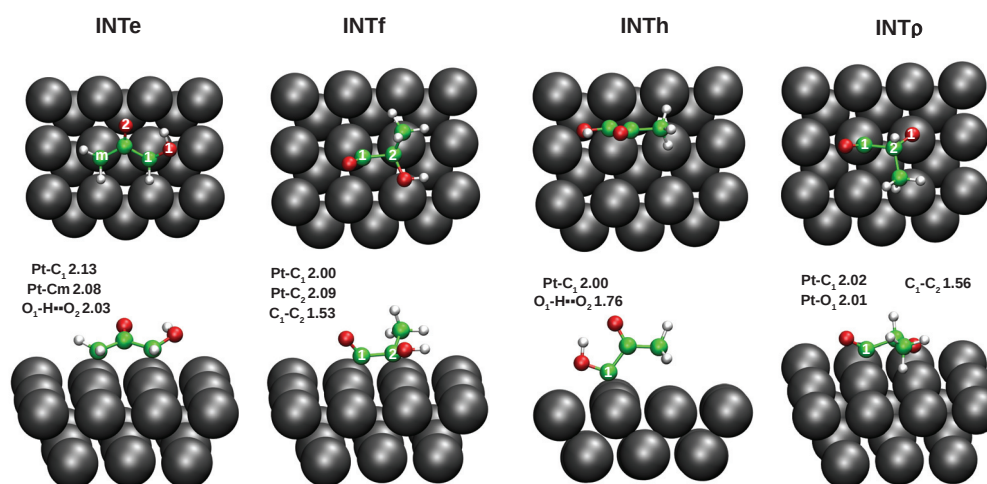


Figure 2.15 – Top (upper part) and side (bottom part) view of the optimized geometries of INTe-f and INT ρ on the Pt(100) surface. Relevant geometrical descriptors are reported in Å units.

According to these findings it seems that only the path leading to INTf should be taken into account for successive dehydrogenation steps, on the basis of the thermodynamic stability of its precursor and of the accessible activation barrier for its production.

1,2-PDO - 5H

INTj is produced through the remaining O-H bond scission of INTf. This molecular event has been calculated to require 20.1 kJ mol⁻¹; the process is slightly exoergic, since INTj results to

be 14.2 kJ mol^{-1} more stable than INTf.

C-C bond cleavages

The discussion presented so far dealt only with the dehydrogenation of 1,2-PDO *via* O-H or C-H cleavages. However in order to gain further insights regarding the competition between dehydrogenation and polyol shortening, it is necessary to discuss also the C-C bond breakings. Similarly to what already done previously for the other exposed surface of the cluster, the calculated activation barriers for C-C bond cleavages molecular events were reported in the Table 2.2 and compared with those required for dehydrogenation. It has to be said that dehydrogenation steps were not investigated for all the surface species here presented (*e.g.* INTe and INT ω) when they were judged unlikely to form on the surface. However, the activation barrier for the C-C bond cleavages was calculated in any case, to make easier a comparison with the findings presented for the (111) surface. On the (100), in agreement with those previous results, the energy required to break the C-C bond seems to decrease with the surface species dehydrogenation, reaching his lowest value with INTj and INT ω ; the latter can be hardly formed on the surface since the methylic group in INTj has not a proper orientation to guarantee the interaction with the surface.

Table 2.2 – Activation barriers in kJ mol^{-1} for the C1-C2 bond breaking of selected reaction intermediates showing different dehydrogenation degree (DeH). In the last five columns are reported the activation barriers for the possible dehydrogenation processes that a given intermediate can undergo.

Intermediate	Formula	DeH	$E_a^{\text{C1-C2}}$	$E_a^{\text{O1-H}}$	$E_a^{\text{O2-H}}$	$E_a^{\text{C1-H}}$	$E_a^{\text{Cm-H}}$
INT5	$\text{CH}_3\text{COHCHOH}$	2	103.2	95.5	26.0	81.9	103.4
INTa	CH_3COCHOH	3	79.9	82.1	-	113.4	87.5
INTb	CH_3COHCHO	3	129.2	-	69.7	54.3	-
INT χ	CH_3CHOHCO	3	66.5	-	-	-	-
INTe	CH_2COCHOH	4	147.5	-	-	-	-
INTf	CH_3COHCO	4	61.9	20.1	-	-	-
INTj	CH_3COCO	5	36.3	-	-	-	-
INT ω	CH_2COCO	6	30.7	-	-	-	-

Structure sensitivity

In order to investigate the reaction structure sensitivity, it is useful to compare some of the most significant results presented in Part I, for the Pt(111), with those collected here for the Pt(100). In particular, in Figure 2.16 the potential energy curve for the 1,2-PDO dehydrogenation to the 1,2-dioxy (INT7) and HA species is reported for both the surfaces; the formation of these products passes through initial O-H bond ruptures, leading to INT1 and INT4, and thus it could offer insights on the activity of the two surfaces toward these specific bond breaking steps. It seems that on Pt(100) both the primary and secondary hydroxyl O-H bond cleavages have lower activation barriers than on the Pt(111), but on this latter INT1 and INT4 result

Chapter 2. Platinum catalyzed 1,2-PDO decomposition

more stable. In other words, the more open surface seems to enhance the kinetics of these molecular events, while the (111), the thermodynamics. However, just as reported for the Pt(111) the formation of 1,2-dioxy species should not be favoured, on the grounds of the more favorable activation barriers and thermodynamics shown by the other reaction pathways.

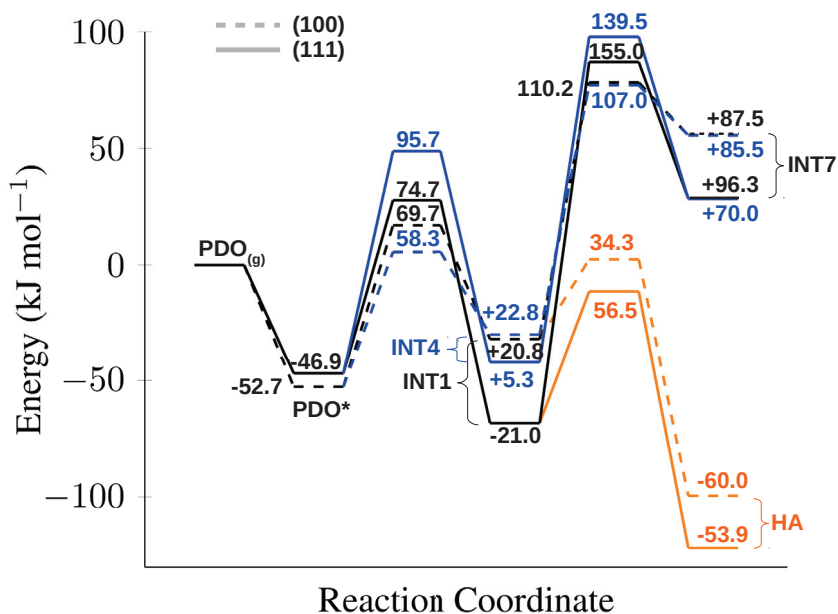


Figure 2.16 – Potential energy curves for the 1,2-PDO dehydrogenation on a model Pt(111) (solid lines) and Pt(100) (dashed lines) surface. Blue lines are associated to the paths leading to INT7, orange lines to those leading to HA. The activation barriers are displayed over each transition state energy level; the difference between the final product energy and its precursor is displayed next to each reaction intermediate energy level.

Different conclusions can be drawn for the C-H bond cleavages leading to INT2 and INT3: indeed, as it is evident from Figure 2.17, lower activation barriers are accompanied also by an increased thermodynamic stability of the surface species formed, with respect to the (111). This corroborates the hypothesis that the Pt(100) should be more active toward initial C-H bond breaking with respect the O-H ones. The same behaviour was encountered for the second dehydrogenation step, with the only exception of HA formation, which is exoergic on the (111) (HA is 15.6 kJ mol⁻¹ more stable than INT3) and endoergic on the (100), being the product 20.0 kJ mol⁻¹ destabilized with respect its precursor. The formation of INT9, the product of the primary carbon double dehydrogenation, has on the two planes nearly similar activation barriers – 79.3 (100) and 89.4 (111) kJ mol⁻¹ – but the formed surface species is much more stabilized on the (100) than on the (111).

The decomposition of INT5 on Pt(100) seems to be more difficult than on the Pt(111) surface;

2.3. Part II - 1,2-PDO decomposition on a Pt(100) surface

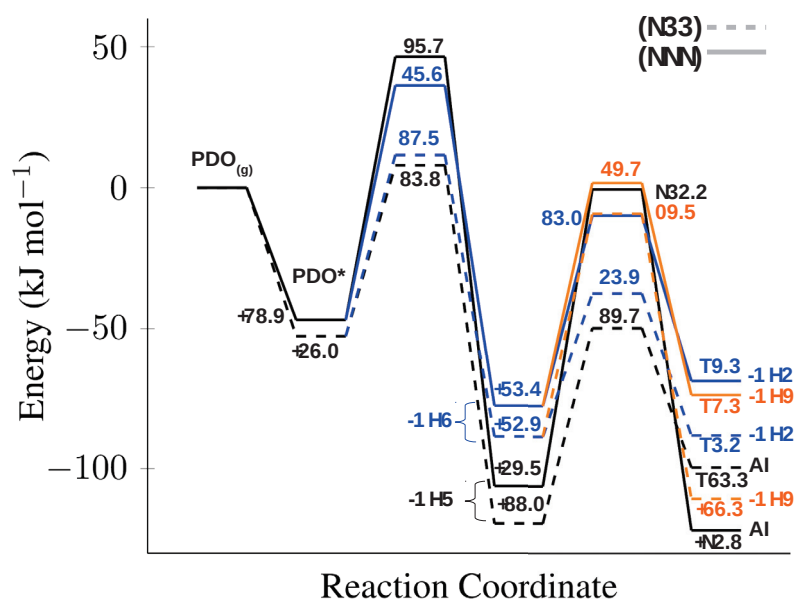


Figure 2.17 – Potential energy curves for the 1,2-PDO dehydrogenation on a model Pt(111) (solid lines) and Pt(100) (dashed lines) surface. Blue lines are associated to the paths leading to INT5, orange lines to those leading to INT9 and black ones for those leading to HA. The activation barriers are displayed over each transition state energy level; the difference between the final product energy and its precursor is displayed next to each reaction intermediate state.

Table 2.3 – Activation energy (E_a) and reaction energy difference (ΔE) for dehydrogenation of INT5 to INTa-d on Pt(100) and Pt(111); the same quantities were reported for dehydrogenation steps leading from INTa to INTe and INTf and from INTb to INTf.

Intermediate	(100)		(111)	
	E_a	ΔE	E_a	ΔE
INTa	26.0	-13.9	10.1	-39.4
INTb	95.5	-33.7	38.1	-17.0
INTc	103.4	-34.3	57.8	-19.1
INTd	81.9	-10.5	69.5	-1.0
INTe	87.5	-20.9	47.1	-26.3
INTf	54.3	-19.0	39.9	-47.5
INTf	113.4	18.9	84.7	7.6

indeed, all the activation barriers associated to the dehydrogenation are higher on the more open surface. However, this increase is not homogeneous for all the reaction pathways: as an example, while the formation of INTb passes from a required activation barrier of 38.1 kJ mol^{-1} on the (111) to the 95.5 kJ mol^{-1} calculated on the (100), that of INTa requires only 15.9 kJ mol^{-1} more. A comparison between activation barriers and the stability of the produced intermediates formed in the two cases is reported in Table 2.3; these results may suggest that on the (100) the reaction flux could pass more selectively through INTa and then it should convert to INTb *via* tautomerization. Hence the activation barrier for this hydrogen shift is even lower on the (100) and INTb is 19.8 kJ mol^{-1} more stable than INTa.

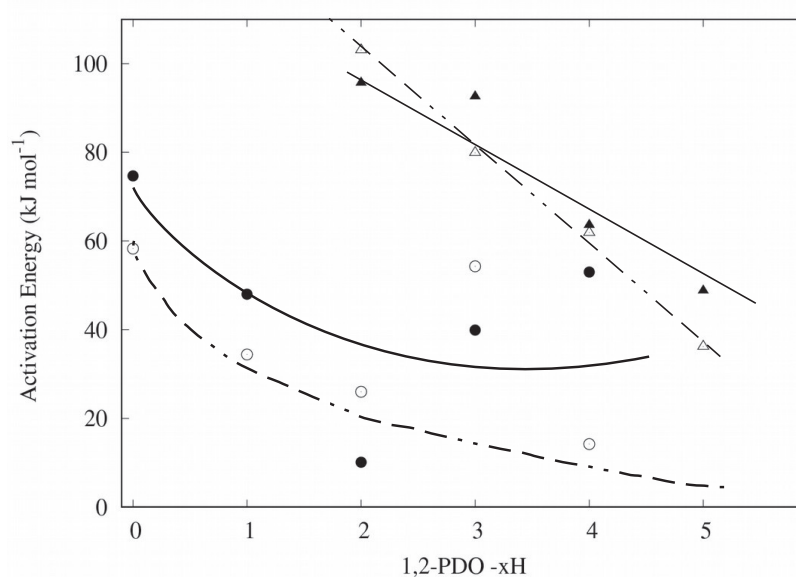


Figure 2.18 – Lowest activation energies associated to dehydrogenation and C-C bond cleavages of surface intermediates with different hydrogen content. Dehydrogenation on Pt(111) and on Pt(100) are represented respectively with full (●) and open (○) circles; C-C bond breakings on Pt(111) and Pt(100) are reported as full (▲) and open (△) triangles. Solid (Pt(111)) and dashed (Pt(100)) lines are intended to be guide for eyes.

Finally, the lowest activation barriers associated to dehydrogenation and C-C bond cleavages of each surface intermediate, at variance with the number of hydrogen atom lost was reported in Figure 2.18; this could be useful to obtain, qualitatively, a picture of the processes occurring on the (100) and (111) surface and their mutual competition. Even if finding general trend is not easy, we can reasonably say that the dehydrogenation seems slightly favoured on the (100) surface, at least if we consider among all, the lowest activation energy path for each surface intermediate. Of course there are some exception to this trend and we should take into account also the case of INT9 which has been demonstrated to have negligible activation barrier for the dehydrogenation, due to the formation of a terminal CO moiety.

Another important conclusion, in agreement with the literature [51], is that, in both cases the C-C bond breaking should become competitive with the dehydrogenation basically when 1,2-PDO has been almost completely dehydrogenated.

Conclusions

The 1,2-PDO decomposition mechanism has been studied on the (111) and (100) surfaces of a purposely shaped Pt cluster, by means of DFT calculations. In both cases, it has been shown that broadly there are two main paths that the reaction can follow: the formation of hydroxyacetone and a combined dehydrogenation/polyalcohol shortening process.

Particular attention was devoted to study the competition among C-H, O-H and C-C bond cleavages; it has been found, in agreement with the literature, that both on a Pt(111) and Pt(100) surfaces, the C-C bond breaking is activated only on highly dehydrogenated surface species. Moreover, if this specific cleavage involves a terminal CO moiety, the bond rupture is facilitated.

For the Pt(111) surface, BEP relationships, relating the reaction energy and the associated activation barrier for C-H, O-H and C-C bond cleavages molecular steps, were found; these can be used for future work developments, concerning computational catalyst screening, starting from pure thermodynamical, DFT computed, quantities.

On the whole, even if exceptions can be found, the Pt(100) surface seems to be more active toward the dehydrogenation with respect to the Pt(111) especially in the first dehydrogenation steps, while nearly similar activation barriers for the C-C bond breakings were found. In both cases, it has to be stressed the importance of intramolecular hydrogen shift steps, by which it could be possible to access pathways, otherwise kinetically unfeasible.

3 Computational Design of a Boron Nitride Supported Pd Catalyst

Formic acid was recognized as a viable source of hydrogen and high interest is addressed to the research of new technologies able to convert selectively this substrate to CO₂ and H₂, suppressing the formation of CO. As already pointed out in Chapter I, sub-nanometric metal catalysts seem to offer new possibilities for achieving high activities and selectivities in a wide range of chemical processes. Thus, a predictive study on the potential use of sub-nanometric metal clusters as catalyst for FA decomposition could offer new insights on the development of materials with selected catalytic properties.

However, in order to gain a more realistic picture of a catalytic system, the inclusion of a support should be considered, especially in the case of sub-nanometric catalysts. A particular interest was recently devoted to BN based materials. Indeed, they showed really interesting properties such as high chemical and thermal stability as well as great mechanical strength and high thermal conductivity [25, 24, 83]; these features make them especially suitable for high temperature technologies and catalysis. As an example, while it's reported that for common catalyst supports, such as γ -Al₂O₃, a partial sintering of dispersed metals occurs, boron nitride nanotubes or nanosheet should not affect the catalyst dispersion due to their thermal properties and the lack of acidic sites [84]. Moreover, in opposition to the wide majority of catalytic supports, they are hydrophobic, thus suggesting the possibility to use them in reactions where the presence of water or moisture could influence the catalyst stability and activity [85]. Moreover, BN materials were demonstrated to have potential applications as hydrogen storers.

In agreement with these state of art information, we hypothesized the possibility of combining the unique characteristics of sub-nanometric metallic catalysts and of boron nitride based supports for applications in FA dehydrogenation.

Therefore, in this chapter the potential use of a supported sub-nanometric palladium cluster as catalyst for FA decomposition was investigated by means of computational methodologies.

The chapter is structured as follows:

- Part I - Growth of a sub-nanometric Pd cluster on a boron nitride support. The growth

Chapter 3. Computational Design of a Boron Nitride Supported Pd Catalyst

pattern of a Pd cluster, going from Pd₂ to Pd₈, on a boron nitride nanotube was studied. This part was aimed at disclosing how the Pd cluster can grow on a solid support, focusing both on a structural and energetic perspective;

- Part II - Reactivity of formic acid on a hexagonal boron nitride (*h*-BN) supported Pd₆ catalyst. A Pd₆ cluster, studied in Part I, is investigated as catalyst for the formic acid decomposition. Particular attention is devoted to understand the effect of sub-nanometric size of the cluster, by comparing the results with state of art calculations on a Pd(111) surface. The support effects are evaluated performing calculations on different sites of the cluster, *i.e.* on Pd atoms far or directly in contact with the boron nitride sheet. Finally, insights on the spillover mechanism of hydrogen, on the support and on the cluster are provided;
- Part III - Influence of *h*-BN defectivity on the formic acid decomposition. The introduction of a B vacancy on the support is discussed, focusing on its influence on the reactivity presented in Part II.

Part I was adapted from an already published article, entitled "Growth of sub-nanometric palladium clusters on boron nitride nanotubes: a DFT study" [86].

Part I - Growth of a sub-nanometric Pd cluster on a boron nitride support

Computational Details

The calculations were performed by means of the Gaussian 09 package [70]. Except from few explicit cases, a QM/MM approach exploiting the 2-layer ONIOM method [87] was employed for all the calculations. According to this approach, we chose the Universal Force Field (UFF) [88] as low accuracy method and DFT as the high accuracy one. For the latter, the Coulomb-Attenuated CAM-B3LYP hybrid exchange-correlation functional was used. The Los Alamos LANL2 effective core potential with the corresponding double- ζ basis set was employed for the Pd atoms while for the B and N atoms the Dunning D95V basis set was used.

The ONIOM model system is a circumcoronene-like $B_{27}N_{27}$ portion of a (12,12) armchair single walled BNNT, formed on the whole by 12 unit cells. This was chosen on the ground of test calculations involving two different model system sizes – namely, $B_{27}N_{27}$ and $B_{48}N_{48}$ – and the largest cluster used in this investigation, the Pd_8 one, whose properties should be reasonably the most affected by the model system dimension. The Pd_8 adsorption energy was evaluated on both these model systems and the difference between the two results was negligible, being *ca.* 10 kJ mol^{-1} . Therefore, the $B_{27}N_{27}$ model system was used in order to optimize the computational efficiency. Since the calculations are not periodic, the dangling bonds on the terminal sides of the nanotube were saturated with hydrogen atoms.

In order to determine the electronic ground state of the different systems, a full geometry relaxation was carried out on a number of models resulting from the adsorption on the BNNT of one Pd atom (Pd_1) and of all the studied palladium clusters, from Pd_2 to Pd_8 , considering the possibility of several configurations and performing all the calculations in the singlet, triplet and quintet spin multiplicities. The nature of minimum on the potential energy surface of an optimized structure was always checked by the calculation and inspection of the harmonic vibrational frequencies. The adsorption energy of a Pd_n cluster on the BNNT was obtained through the general formula

$$\Delta E_n^{Ads} = E_{Pd_n/BNNT} - E_{BNNT} - E_{Pd_n} \quad (3.1)$$

where $E_{Pd_n/BNNT}$ is the total energy of the supported cluster system, E_{BNNT} the energy of the pristine BNNT and E_{Pd_n} the energy of the isolated Pd_n cluster at the same level of theory in its most stable spin multiplicity, which is the singlet for Pd_1 , the triplet for Pd_n ($n = 2 - 7$) and the quintet for Pd_8 . For the $Pd_1/BNNT$ system, the BSSE has been estimated applying the counterpoise method [89] on the solely model system of the ONIOM scheme, saturating with hydrogen atoms the dangling bonds on the edge.

Results and Discussion

The analysis of the nucleation and growth mechanisms of metal atoms to form clusters on surfaces could be a really expensive computational task. Indeed, depending on the number of metal atoms considered and on the chemical nature of the support surface, the number of different metal-atoms/surface-sites combination could become prohibitively high.

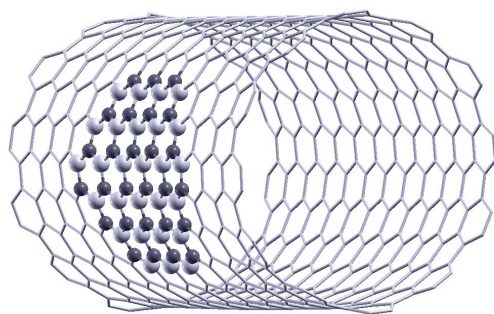
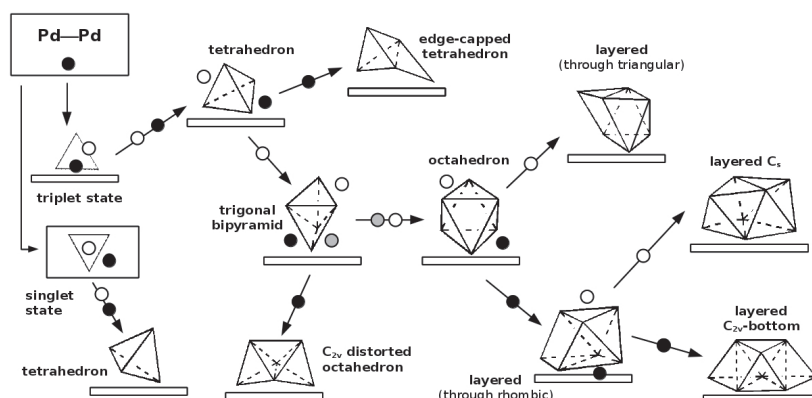


Figure 3.1 – Optimized (12,12) single walled armchair BNNT geometry: the model system used in the QM/MM ONIOM approach is highlighted by balls and sticks.

Taking into account the boron nitride nanotube, whose optimized structure is depicted in Figure 3.1, five possible adsorption sites for one metal atom can be easily recognized, namely the boron and nitrogen atop sites, the axial and zig-zag bridge sites and the center of the B_3N_3 ring. As a consequence, even the introduction of a second metal atom causes a large increase of the number of the different configurations that should be explicitly considered. In the present case, however, the two different bridge sites might be considered as equivalent. This approximation, substantiated by the slight dependence of the adsorption energies from the adsorption surface sites that characterize the transition metals on BNNTs [90], was useful to capture information in the most complicated cases. In view of this, a peculiar strategy was adopted for modeling the palladium cluster growth. At the n -th step of the growth algorithm employed, a pair of Pd_n /BNNT systems were actually generated by adding a Pd atom in two different ways to the most stable of the available Pd_{n-1} /BNNT structures. In the first case, a site at the center of an exposed Pd_{n-1} cluster face, far from the support, was chosen; in the second, the additional Pd was placed in such a way to assure interactions both with the already adsorbed cluster and the BNNT surface. A representation of this procedure is reported in Scheme 3.1. By using this protocol, it has been possible to discriminate the contributions given to the system stability by the cooperative or competitive metal-metal and metal-support interactions; the interplay between them indeed should orient toward vertical (metal-driven) or horizontal (support-driven) growth of the cluster.

The single palladium atom adsorbs on the BNNT by a N-atop coordination, showing an adsorption energy of 58.6 kJ mol^{-1} (36.9 kJ mol^{-1} after the BSSE correction) and a Pd–N

3.1. Part I - Growth of a sub-nanometric Pd cluster on a boron nitride support



Scheme 3.1 – Algorithm used for the Pd cluster growth on BNNT support: $\text{Pd}_{n-1} + \text{Pd} \rightarrow \text{Pd}_n$; white circles represent new Pd atoms placed on preexisting Pd_{n-1} faces, not in contact with the support surface; the black circles, conversely, represent new Pd atoms placed at the border between the adsorbed Pd_{n-1} cluster and the support. The most stable Pd_n cluster formed, was always chosen. The optimized geometry of the cluster in a given Pd_n/BNNT system is depicted by the representative polyhedron and identified according to the name used throughout the text; BNNT is schematically shown.

interaction distance of 2.28 Å. This kind of interaction between palladium and nitrogen has been already described by Koitz *et al.* [91] in a computational investigation of the BN-sheet growth on the surface of different transition metals.

The optimized structures that we considered relevant for describing the properties of the palladium cluster on the boron nitride nanotube, Pd_n/BNNT ($n = 2-4$), are displayed in Figure 3.2. When a second metal atom is added to the monometallic system to form the Pd_2 dimer, the configuration with the singlet spin multiplicity state is characterized by an adsorption energy of 96.5 kJ mol^{-1} while it shows one BN-bridge and one N-atop coordinated palladium atom (see Figure 3.2a). In the triplet state each palladium atom is instead N-atop coordinated to two different nitrogen atoms (Figure 3.2b), being however 71.8 kJ mol^{-1} less stable than in the singlet state. The latter thus becomes the most stable multiplicity state after Pd_2 adsorption, in line with an already reported result concerning the interaction of a palladium dimer with the phenyl rings of hypercrosslinked polystyrene [62]. Of course, the geometry and the spin state adopted by the BNNT adsorbed palladium dimer are the result of the balance among the Pd-Pd, the Pd-N and the Pd-B interactions. With respect to the isolated palladium dimer, the Pd-Pd interaction actually seems unchanged in the triplet spin state as well as the corresponding bond distance (2.53 Å). Clearly, the longer bond in the singlet Pd_2 (2.80 Å) allows a better interaction with the BN rings, as witnessed by the smaller Pd-N bond distances reported in Table 3.1.

The Pd_3/BNNT system, in the triplet state, shows two Pd atoms interacting atop with two N

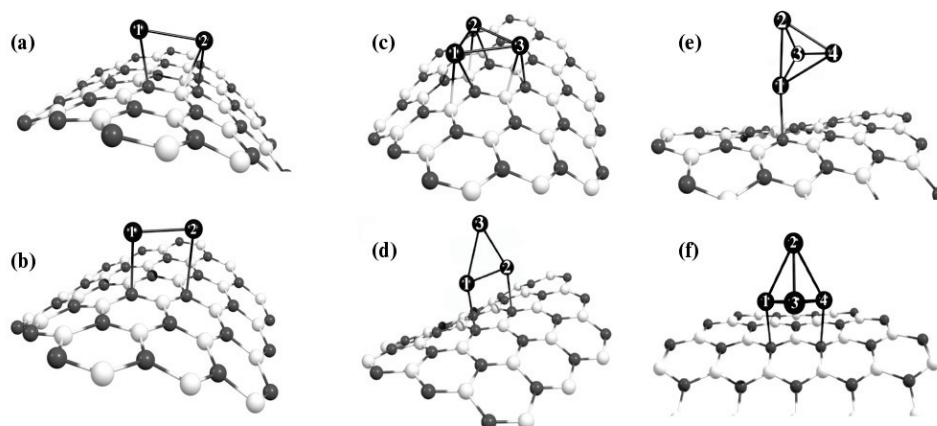


Figure 3.2 – Optimized structures of BNNT supported palladium clusters: Pd₂/BNNT in the (a) singlet and (b) triplet spin state, Pd₃/BNNT in the (c) singlet and (d) triplet spin state and Pd₄/BNNT with (e) N-atop and (f) N-atop/N-atop coordination.

Table 3.1 – Bond distance (bd) values, characterizing the adsorbed cluster geometries in the Pd₂/BNNT (singlet and triplet states) and Pd₃/BNNT (singlet and triplet states) systems

	Pd ₂ bd / Å		Pd ₃ bd / Å		
	M _s =0	M _s =1	M _s =0	M _s =1	
Pd1-Pd2	2.80	2.53	Pd1-Pd2	2.80	2.55
Pd1-N	2.30	2.54	Pd1-Pd3	2.82	2.65
Pd2-N	2.43	2.54	Pd2-Pd3	2.90	2.66
Pd2-B	2.30	—	Pd1-N	2.39	2.38
			Pd1-B	2.43	—
			Pd2-N	2.38	2.38
			Pd2-B	2.39	—
			Pd3-N	2.48	—
			Pd3-B	2.32	—

Table 3.2 – Bond distance (bd) values, characterizing the adsorbed cluster geometries of the Pd₄/BNNT system in its triplet state.

	Pd ₄ bd / Å		
	N-atop	N-atop/BN-bridge	N-atop/N-atop
Pd1-Pd3	2.69	2.74	2.76
Pd1-Pd4	2.71	2.73	2.59
Pd2-Pd3	2.57	2.56	2.54
Pd2-Pd4	2.57	2.60	2.63
Pd3-Pd4	2.70	2.71	2.77
Pd1-N	2.38	2.58	2.46
Pd4-B	—	2.57	2.89
Pd4-N	—	—	2.46

3.1. Part I - Growth of a sub-nanometric Pd cluster on a boron nitride support

atoms; the optimized structure of the singlet state cluster, which is less stable by 23.8 kJ mol^{-1} with respect to the triplet, conversely shows, for all the metal atoms, a BN-bridge coordination (Figure 3.2c). In the triplet state, the cluster retains the isosceles triangular geometry found for the unsupported Pd_3 case, with the same spin multiplicity, but it can be also observed a shortening of the bond between the Pd atoms interacting with the BNNT surface and the concomitant increase of the other two Pd-Pd bonds. On the other hand, the supported Pd_3 in the singlet state shows three different Pd-Pd distances, whereas *in vacuo* the singlet has an equilateral triangular geometry with the Pd-Pd distances equal to 2.55 \AA (Table 3.1) and is 46.4 kJ mol^{-1} less stable than the triplet. So, although its geometry is subjected to distortion, the singlet multiplicity of Pd_3 is slightly stabilized when the cluster is adsorbed on BNNT. The increased stability of the singlet state is imputable to the increased number of interactions occurring with the B_3N_3 ring: in the singlet geometry the Pd_3 cluster indeed lies on the support surface whereas in the triplet only two atoms of the cluster, as it was found for the Pd dimer, interact with it (Figure 3.2d). Considering the small energy gap between the two multiplicity states, both the adsorption geometries of Pd_3 were included in the following growth scheme.

It is well known that the Pd_4 cluster exhibits two stable *in vacuo* structures: one is square planar with D_{4h} symmetry and one, which is the most stable, a slightly distorted tetrahedron [92, 93]. Of course, adsorption processes could affect both the geometry and the intrinsic energy order of these structures. The supported cluster, either in the singlet or in the triplet spin states, shows always a tetrahedral geometry, irrespective of the multiplicity of the starting Pd_3 structure. However, now the triplet multiplicity is by far the preferred one, being 82.1 kJ mol^{-1} more stable than the singlet, which therefore will not be further discussed. The tetrahedral cluster can interact by different binding modes with the BNNT. A single Pd vertex interacts N-atop with the support, or a Pd-Pd edge interacts with two different sites of the BNNT resulting in a coordination that might show an N-atop/BN-bridge or N-atop/N-atop configuration (Figure 3.2e,f).

As a matter of fact, all these adsorption geometries are approximately isoenergetic, with interaction energies of $147.4 \text{ kJ mol}^{-1}$, $148.5 \text{ kJ mol}^{-1}$, and $152.3 \text{ kJ mol}^{-1}$, respectively. The geometry of the adsorbed Pd_4 clusters is essentially the same, irrespective of the adsorption mode (see Table 3.2). When the Pd_4 interacts by only one metallic center a stronger Pd-N interaction can be observed, along with a bond distance of 2.38 \AA while, when it interacts by two metallic centers, the double Pd-N interaction is weakened, which results in longer bond distances: 2.58 \AA for the N-atop/BN-bridge, 2.46 \AA for the N-atop/N-atop. It has to be stressed that the optimization procedure leads to the tetrahedral adsorbed configurations, even considering a planar D_{4h} Pd_4 as starting point. Therefore, it is reasonable to believe that a square planar arrangement of palladium atoms may not occur on the BNNT, a hint that the BNNT surface could control the morphology of the sub-nanoparticle.

Clearly, the geometry and the interaction energy of the adsorbed cluster should result from the interplay of the Pd-Pd interactions and of the Pd-B and Pd-N ones. Besides, according to Zhang and Alexandrova [92], which showed that the adsorption of small palladium clusters on

Chapter 3. Computational Design of a Boron Nitride Supported Pd Catalyst

TiO₂ is mainly controlled by the matching of the symmetry of the cluster with the local surface morphology, also the BNNT support could be able to rule the final cluster symmetry.

The larger Pd_n (n=5-8) clusters are characterized by several geometries, which were already treated in the literature using different computational methods [94, 95, 96]. The corresponding energy differences associated to the various geometries of a Pd_n species, when optimized *in vacuo*, can be quite small. As regard the Pd₅ cluster, it was reported that the energy differences of the three most stable configurations – namely, square pyramidal, edge-capped tetrahedral and trigonal bipyramidal – are within a range of 30 kJ mol⁻¹, according to the results obtained by multi-reference *ab initio* methods. The same structures were here obtained by the growth algorithm, both in singlet and triplet spin states on BNNT and, for the sake of comparison, also *in vacuo* at the CAM-B3LYP level. In each case, the triplet state was the most stable (*ca.* 90 kJ mol⁻¹ lower in energy than the singlet) while the trigonal bipyramidal geometry was found to be the one energetically preferred both on BNNT (the adsorption geometry is shown in Figure 3.3a, being its adsorption energy 68.3 kJ mol⁻¹) and *in vacuo*. The supported Pd₅ cluster shows two palladium atoms interacting N-atop/N-atop with the BNNT support: the two Pd-N distances were 2.38 Å, while the Pd(1)-Pd(2) one was 2.58 Å, being Pd(1) and Pd(2) the atoms directly bonded.

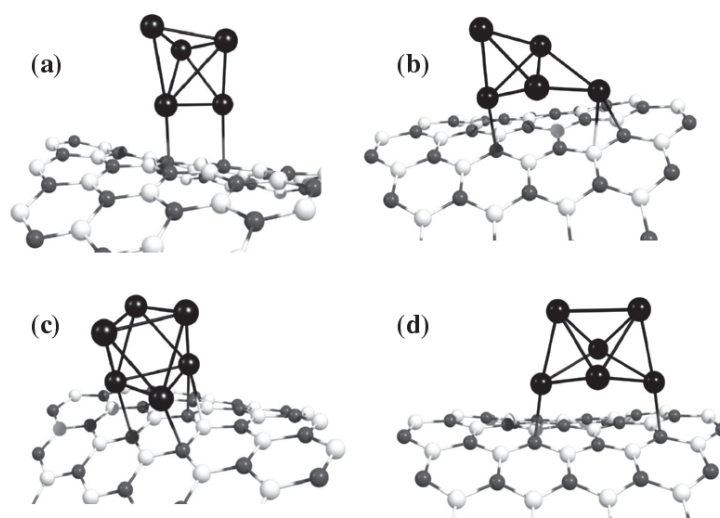


Figure 3.3 – Optimized structures of the BNNT supported Pd₅ and Pd₆ clusters: Pd₅/BNNT (a) trigonal bipyramidal and (b) edge-capped tetrahedral geometries, Pd₆/BNNT (c) octahedral and (d) C_{2v} distorted octahedral geometries.

When adsorbed on BNNT, the Pd₅ edge-capped tetrahedral cluster (Figure 3.3b) resulted 27.7 kJ mol⁻¹ less stable than the trigonal bipyramidal reference, characterized by a triplet spin state. Interestingly, while the Pd₅ edge-capped tetrahedral structure was previously reported as a saddle point in the PES of the isolated Pd₅ cluster, it is a local minimum when interacting with BNNT. In fact, according to the CAM-B3LYP results, the edge-capped tetrahedral Pd₅ geometry is not a stationary point in the isolated state, since it invariably converts to the

3.1. Part I - Growth of a sub-nanometric Pd cluster on a boron nitride support

trigonal bipyramidal structure after geometry optimization. On the other hand, although it is described as a minimum in the isolated state, with an energy 29 kJ mol^{-1} higher than that of the trigonal bipyramidal structure, the square pyramidal Pd_5 is a saddle point in the Pd_5/BNNT triplet surface. This evidence also suggests that the support should be able to affect the cluster energetics and growth. Noticeably, in the singlet surface of Pd_5/BNNT , the square pyramidal structure is a minimum, being however its energy 81 kJ mol^{-1} higher than that of the ground state.

Two optimized minima characterize the supported Pd_6 cluster, both showing octahedral geometries: one regular and the other very distorted. The first, which in the triplet state is 89.9 kJ mol^{-1} more stable than the singlet, adsorbs through a triangular face (Figure 3.3c). The second, characterized by a C_{2v} symmetry, interacts N-atop/N-atop (Figure 3.3d). Also in the distorted Pd_6 cluster, the triplet is more stable (by 78.8 kJ mol^{-1}) than the singlet. The regular octahedral geometry, which has an adsorption energy of 70.3 kJ mol^{-1} , is 12.0 kJ mol^{-1} more stable than the C_{2v} one. This energy difference is almost the same of that calculated by Ni and Zheng [97], at the RPBE level, for the isolated Pd_6 . However, according to our calculation, the *in vacuo* C_{2v} isolated species does not exist since it spontaneously converts to the octahedral one. It is worth noting (see Figure 3.3c) the complementarity of one of the octahedral Pd_6 faces with the three nitrogen atoms of the B_3N_3 ring. This, as might be expected, could rule a better interaction of the Pd cluster with the BNNT surface. Then, comparing the Pd-Pd bond distances of this face with those of the opposite one, a small deformation of the octahedron can be noticed: the interacting face experiences in the average a Pd-Pd bond lengthening of 0.1 \AA while the opposite face results slightly shrunken. Again, this is determined by efficient Pd_6 -BNNT interactions, in details two N-atop interactions (being the Pd-N distances equal to 2.45 and 2.48 \AA) and a bridge one (being the Pd-N and Pd-B distances equal to 2.44 and 2.41 \AA , respectively).

The *in vacuo* Pd_7 cluster shows a large number of geometries, ranging from the pentagonal bipyramid to the face-capped octahedron [96, 98]. The first, in the triplet spin state, was already presented in the literature as the most stable. However, as reported by Li *et al.* [95], distortions can occur due to the adsorption of small oxygenates, resulting in layered clusters similar to edge-capped octahedra. Indeed, upon the adsorption of the Pd_7 on the BNNT we found the same layered structure that, in the triplet state, resulted on the whole the most stable. This cluster is characterized by two layers (triangular and rhombic shaped) and, just for its peculiar symmetry, it was employed to demonstrate the interplay between the metal cluster and support surface geometry-matching with the metal and support binding interaction ability. As a matter of fact, we found that the energy difference arising from adsorbing the rhombic or triangular face of the cluster on BNNT is only 5 kJ mol^{-1} , the more stable species (rhombic face interacting) showing an adsorption energy of 87.8 kJ mol^{-1} . Likely, the favorable energetic contribution due to the formation of four different Pd-N interactions, which is realized when the rhombic face is adsorbed (Figure 3.4a), is balanced by the higher complementarity between the B_3N_3 ring and the Pd_3 face, which occurs when the cluster adsorbs through the triangular face (Figure 3.4b). Eventually this leads to two nearly iso-energetic structures. The other two

structures optimized in the singlet spin state are characterized by a distorted bipyramidal pentagonal geometry, that are *ca.* 80 kJ mol⁻¹ less stable than the triplet state structures.

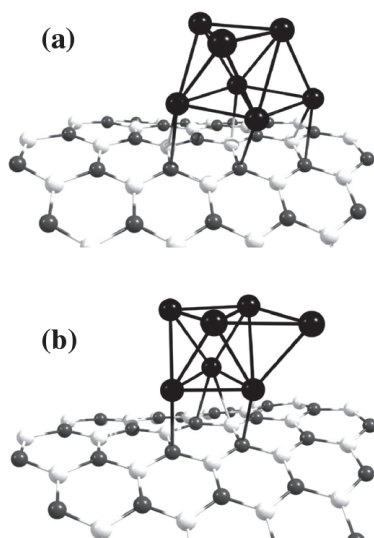


Figure 3.4 – Optimized structures of the BNNT supported Pd₇ layered cluster, adsorbed through (a) the rhombic and (b) the triangular face.

To the best of our knowledge very few studies in the literature concern the complex Pd₈ cluster [94]. Among these, Zanti *et al.* [99] have studied its structure and interaction with CO, *in vacuo* at the B3LYP level. Thus, for the sake of comparison it is interesting to report the here optimized results at the CAM-B3LYP level. In agreement to previous studies, the Pd₈ species shows four different relevant geometries: the most stable has C_s symmetry and a quintet spin multiplicity. It is approximately isoenergetic to a C₂ structure, closely resembling a doubly capped octahedron. Furthermore, a D_{2d} and a C_s Pd₈ geometry can be also found approximately 30 and 50 kJ mol⁻¹ higher in energy. Our calculations verify these geometries. However, one more C_{2v} geometry both with a triplet and quintet spin state was also found. This looks like a layered cluster with one five- and one three-atoms layer, having an arrangement closely resembling a fcc stacking plane disposition. The energetic differences specifying the most stable structures, which are always in the quintet spin state, are extremely small: the ground state shows the features of the C_s structure found by Zanti [99], then the energy increases in the order D_{2d}, C_s and C_{2v}. These are almost isoenergetic, namely within 4 kJ mol⁻¹. The less stable structure is finally the C₂, which shows an energy 22 kJ mol⁻¹ higher than that of the others. Reasonably, the found dissimilarities arise from the correction for the dispersion interactions provided by the CAM-B3LYP functional.

The optimization of the Pd₈/BNNT systems leads to the same C_s, C_{2v} and C₂ structures obtained *in vacuo*. Again the C_s structure (Figure 3.5a) is the most stable but an inversion of stability between the spin states occurs, with the triplet 21.5 kJ mol⁻¹ more stable than the quintet. The adsorption energy between the Pd₈ cluster and the support is 72.6 kJ mol⁻¹. The

3.1. Part I - Growth of a sub-nanometric Pd cluster on a boron nitride support

same inversion was found for the C_{2v} structure of the supported species that actually is slightly more stable (12.5 kJ mol^{-1}) in the triplet than in the quintet spin state. This triplet state lies 28.6 kJ mol^{-1} higher than the C_s reference state. Due to its particular layered structure, the C_{2v} cluster might interact with BNNT through the three-atom layer (C_{2v} -up, Figure 3.5b) or the five-atom one (C_{2v} -bottom, Figure 3.5c). In the C_{2v} -up adsorption mode a distortion of the cluster from its original symmetry is evident, due to the interaction of the cluster with the nitrogen atoms of the BNNT support. Indeed, at least three Pd-N bindings can be evidenced, with a mean bond length of 2.4 \AA , on the whole, contributing to an adsorption energy of 86.2 kJ mol^{-1} . Conversely, in the C_{2v} -bottom interaction mode, which shows an adsorption energy of 89.9 kJ mol^{-1} , the Pd atoms coordinate B-atop while the C_{2v} symmetry is preserved. Despite these differences, the two structures, in their most stable triplet state, are almost isoenergetic, differing by 4 kJ mol^{-1} .

It is worth to note that the energy differences calculated for the supported clusters are wider than for the unsupported ones. This is particularly evident if the supported C_2 Pd_8 structure is taken into account (Figure 3.5d): in the most stable quintet state, in fact, this structure is 44 kJ mol^{-1} less stable than the reference species, twice the difference found for the Pd_8 isolated structure. The reference state stabilization could be easily related to the fitting local connectivity occurring between the interacting face of the cluster and the BNNT surface atoms. In particular, three metallic atoms interact N-atop with one B_3N_3 ring while the fourth has an exocyclic bridge coordination, similar to that of the already described Pd_3 cluster. The Pd-N distances of 2.4 \AA clearly witnesses strong Pd/BNNT interactions.

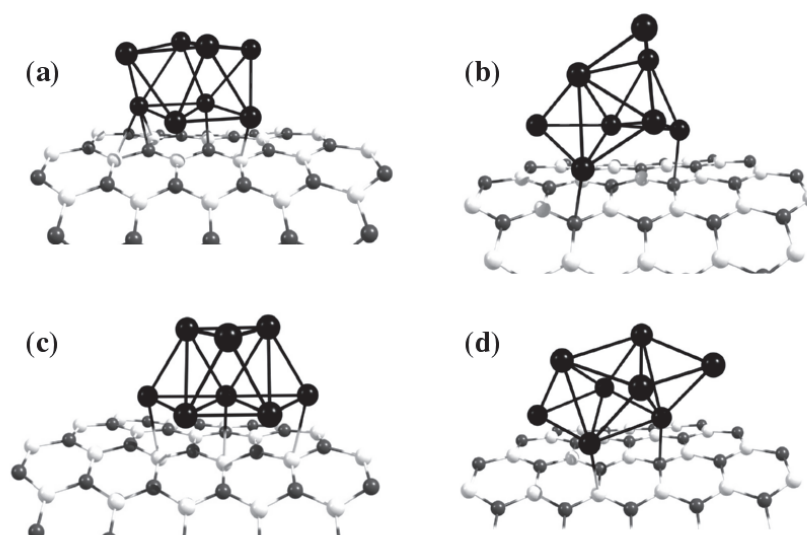


Figure 3.5 – Optimized structures of the supported Pd_8/BNNT cluster: (a) the most stable C_s structure, (b) and (c) C_{2v} -up and C_{2v} -bottom mode of adsorption, (d) quintet multiplicity C_2 structure.

Growth thermodynamics

The calculation of the cluster/support adsorption energy, although useful to investigate the desorption energetics, does not provide peculiar insights into the cluster growth process. The energetic analysis of the cluster growing is however a non trivial task that requires the definition of proper descriptors. With a simplified model, which can be exploited also to get information about the template effect of the BN nanotube, the growth of the Pd clusters onto the BNNT can be thought as a step-by-step process in which a metal atom (already adsorbed on BNNT) joins a preexisting BNNT supported cluster:



This model implies that the diffusion of a Pd atom moving on the BNNT surface should not be highly energy demanding. In order to support this hypothesis – and choosing among all the diffusion paths of one Pd atom on the hexagonal pattern of the BNNT surface – a hopping mechanism between adjacent N atop sites was studied. The process has actually a negligible energy barrier (*ca.* 6 kJ mol⁻¹) associated with a transition state in which the metal atom is B-atop. Straightforwardly, this result validates the model proposed above, also suggesting that the growth process is only slightly affected by the initial distance between the preexisting Pd_{n-1} cluster and the incoming Pd atom on the support. Besides, if the palladium atom and cluster are far away from each other, the interaction energy, E^{int} , of the Pd atom with the BNNT is certainly not influenced by the presence of the Pd_{n-1} cluster on the same support, that is:

$$E^{int}(Pd|Pd_{n-1}/BNNT) \approx E^{int}(Pd/BNNT) \quad (3.2)$$

With this assumption we can calculate the energy associated with the nth growth step, ΔE_n^g , in terms of absolute energies, according to the equation:

$$\Delta E_n^g = E_{Pd_n/BNNT} - E_{Pd_{n-1}/BNNT} - E_{Pd/BNNT}^{BSSE} + E_{BNNT} \quad (3.3)$$

where $E_{Pd_n/BNNT}$ and $E_{Pd_{n-1}/BNNT}$ are the calculated absolute energies of the Pd_n/BNNT and Pd_{n-1}/BNNT systems and $E_{Pd/BNNT}^{BSSE}$ the energy of the Pd/BNNT system, containing the correction for the basis set superposition error. Of course, each contribution was referred to the BNNT supported system in its most stable spin state. Equation 3.3 can be easily rearranged, obtaining:

$$\Delta E_n^g = \Delta E_n^{Ads} - \Delta E_{n-1}^{Ads} - \Delta E_{Pd}^{Ads} + \Delta E_v^g \quad (3.4)$$

where the ΔE_n^{Ads} terms are calculated using Equation (3.1) and ΔE_v^g , which corresponds to the expression $E_{Pd_n} - E_{Pd_{n-1}} - E_{Pd}$, is formed by terms referring only to the isolated metallic species. Finally, the constant term ΔE_{Pd}^{Ads} corresponds to the BSSE corrected adsorption energy of a Pd atom on the BNNT surface and is equal to -36.9 kJ mol⁻¹. From Equation (3.4), the energy of growth, ΔE_n^g , can be described as a sum of contributions, whose physical meaning has been

3.1. Part I - Growth of a sub-nanometric Pd cluster on a boron nitride support

already discussed earlier along the text. In particular, while the first three terms account for metal/support interactions, the last takes into account energetic contributions just related to Pd-Pd interactions, reflecting the energy released upon the addition *in vacuo* of a Pd atom to an isolated preexisting cluster. The calculated ΔE_n^g vs. n (being n the number of the Pd atoms in the cluster) are collected in Figure 3.6; other relevant quantities appearing in Equation (3.4) are reported as well. The trends of ΔE_n^g and ΔE_n^{Ads} show a quite good correlation. Both the curves, indeed, reach a minimum corresponding to Pd₄ and then slightly increase. This effect can be related to a substantial compensation of the terms ΔE_{n-1}^{Ads} and ΔE_v^g . Interestingly, except for the Pd₂ case, the energy released along the growth of a given sub-nanometric cluster is always greater than the energy released upon the adsorption of the same cluster.

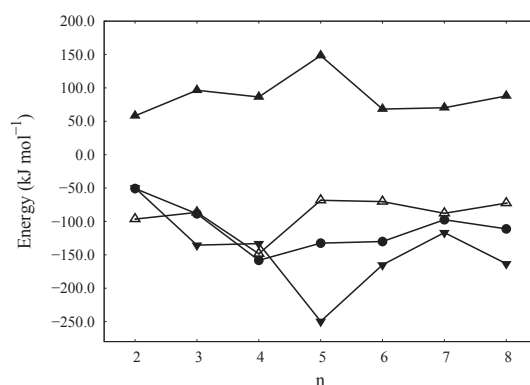


Figure 3.6 – Energy of growth and related energetic contributions characterizing the Pd_n/BNNT systems for different n: filled circles, ●, represent the ΔE_n^g values obtained by Equation (3.4); empty, △, filled up, ▲, and down, ▼, triangles illustrate various contributions (ΔE_n^{Ads} , $-\Delta E_{n-1}^{Ads}$ and ΔE_v^g , respectively) to the ΔE_n^g terms. The other two terms in Equation (3.4), ΔE_1^{Ads} and ΔE_{Pd}^{Ads} , are -58.6 and -36.9 kJ mol⁻¹, respectively.

Analyzing the trend reported in Figure 3.6, it can be noticed that after Pd₅ the growth energy is within 100-130 kJ mol⁻¹. This would seem to suggest that a sort of plateau for ΔE_n^g is reached after the formation of a characteristic triangular metallic face on BNNT, as in the case of the Pd₆, Pd₇ and Pd₈ clusters. Noticeably, the structure of the adsorbed face of the Pd_n (n = 6, 7, 8) clusters does not evidence sensible distortions with respect to the corresponding face in the isolated clusters and, further, the Pd-Pd average bond lengths of these triangular faces (Pd₆, 2.74 Å, Pd₇ rhombic, 2.78 Å, Pd₇ triangular, 2.75 Å and Pd₈, 2.77 Å) are on the whole almost matching the value of the Pd-Pd distance (2.75 Å) found in the (111) surface, showed by appositely tailored Pd₃₀ and Pd₃₆ clusters, which were investigated at the B3LYP level in previous works [62, 100].

The curvature of the lattice might influence to a large extent surface phenomena as adsorption and growth processes. Analyzing the results reported in Figure 3.6, a turning point in the growth process seems to appear in-between the Pd₃ and Pd₄ clusters. In order to rationalize the possible influence of the curvature on the growth process, the geometric and energetic features of both Pd₃ and Pd₄ were evaluated when adsorbed on a (7,7) and on a (20,20) BNNT.

Chapter 3. Computational Design of a Boron Nitride Supported Pd Catalyst

Binding modes and preferred multiplicities resulted the same for both the clusters adsorbed on the differently curved BNNTs. Regarding the energetic of the growth process, it was found that in the (7,7) and (20,20) BNNTs the ΔE_n^g were -159.9 and -163.5 kJ mol^{-1} , respectively. These values are very close to that of the (12,12), that is -158.2 kJ mol^{-1} . Summarizing it seems that a very small contribution to the cluster growth process arises from the BN network curvature, as already found for other surface processes occurring on different nanotube systems [101]. Accordingly, it can be inferred that the palladium cluster growth on a zero curvature BN sheet could occur with the same features found for the BNNT used as model in the present work. This assumption is at the basis of the *h*-BN sheet model used in the next part of the chapter to represent a catalytic support.

Part II - Reactivity of formic acid on *h*-BN supported Pd₆ catalyst

Computational Details

All the calculations were performed using the Vienna ab initio Simulation Package (VASP) [102]. The projector augmented wave (PAW) potentials were used to describe the core electrons interactions, while a plane wave basis set with a kinetic energy cutoff of 500 eV was chosen to expand the electronic wave function. The generalized gradient approximation (GGA) using the Perdew, Burke and Ernzerhof (PBE) [103] exchange correlation functional with the Grimme-D3 [104] semiempirical dispersion correction was used. To simulate a *h*-BN monolayer, a B₄₈N₄₈ supercell was replicated in the *xy* plane, being 15.03 and 17.34 Å the lattice constants; in order to avoid spurious interaction between the periodic replicas, a vacuum layer of at least 15 Å was used in the *z* direction. Due to the relatively large supercell size, the sampling of the reciprocal space was set to the Γ -point. Spin-polarized calculations were carried out and all the structures were fully relaxed until the forces acting on the atoms were smaller than 0.02 eV/Å. This computational setup was tested through benchmarking calculations, ensuring the convergence of total energy with respect to both energy cutoff and κ -point sampling. Transition states (TS) were optimized through the climbing image nudged elastic band method (CI-NEB) [105] using seven images between the initial and final states; a convergence criterion of 0.1 eV/Å was used for the forces and the nature of the stationary point on the potential energy surface was checked by the calculation and inspection of vibrational frequencies. The growth pattern of sub-nanometric Pd clusters on boron nitride supports was extensively studied in the first part of the chapter; according to our findings Pd₆, if supported onto a BNNT, exists in an octahedral geometry, which is the most stable among the Pd₆ geometrical isomers. We have as well demonstrated that the BNNT curvature has a negligible influence on the growth mechanism; thus, it is reasonable to use the same Pd₆ structure as a starting point for the *h*-BN supported cluster geometry optimization.

The adsorption energy E_{ads} of the palladium cluster on the *h*-BN was calculated by means of the following equation:

$$E_{ads} = E_{TOT} - E_{h-BN} - E_{Pd_6} \quad (3.5)$$

where E_{TOT} is the total energy of the system, E_{h-BN} is the energy of the pristine boron nitride sheet and E_{Pd_6} is the energy of the gas phase Pd₆ cluster. Using a similar expression, but taking the formic acid gas phase energy as reference and substituting the second term of Equation 3.5 with the energy of the *h*-BN supported Pd₆, the adsorption energy of formic acid has been calculated.

Results

$\text{Pd}_6/h\text{-BN}$ interaction

The optimized structure of the $h\text{-BN}$ supported Pd_6 cluster is reported in Figure 3.7; the Pd_6 shows a triple atop adsorption mode, in which each of the Pd atoms interacting with the BN surface, is placed directly onto a nitrogen atom, being the Pd-N bond distance 2.31 Å; slightly larger average bond distance of 2.45 Å was previously determined for the same cluster adsorbed on a (12,12) armchair single walled boron nitride nanotube, treated at the CAM-B3LYP level in the first part of the chapter [86]. While *in vacuo* the Pd_6 shows an octahedral geometry, with average Pd-Pd bond length of 2.65 Å some distortions can be found upon adsorption on the $h\text{-BN}$ support, that lead to an increased average bond distance of 2.68 Å. Indeed, due to the interaction with the N atoms of the support, the distance among the palladium atoms lying on the surface is increased, reaching a maximum value of 2.73 Å. The adsorption energy of the cluster has been calculated according to Equation 3.5, resulting to be $-171.2 \text{ kJ mol}^{-1}$. A direct comparison of this value with previous literature is quite difficult, due to the relative lack of studies with similar systems at the same level of calculation. As an example, on the above mentioned BNNT, a much lower adsorption energy of $-85.0 \text{ kJ mol}^{-1}$ was found, but this difference may of course be related to the different systems treated as well as the computational methods employed. In any case it is informative to compare the adsorption energy found in this study with other interaction energies obtained for selected sub-nanometric palladium clusters on typical supports used in catalysis. Indeed, one of the conclusions achieved in the most part of experimental studies dealing with boron nitride based supports, is that they should interact weaker with noble metal nanoparticles with respect to other support such as carbon nanotubes and $\gamma\text{-Al}_2\text{O}_3$ [106]. The value found in the current study is well below that was previously found by Kacprzak *et al.* [107] for Pd_9 on $\gamma\text{-Al}_2\text{O}_3$, being the adsorption energy $-318.0 \text{ kJ mol}^{-1}$ in this case, or by Duca *et al.* [108] for the same cluster on a CNT, being instead $-227.0 \text{ kJ mol}^{-1}$.

The electronic properties of the adsorbed Pd_6 were studied by means of projected density of states calculations, as shown in Figure 3.8; the interaction between the cluster and the support can be ascribed to the efficient overlap between the Pd 4d and N 2p states located right under the Fermi level. As a consequence of this interaction, upon Pd_6 adsorption, an overall broadening of the sharp peaks localized between -4 and -2 eV in Figure 3.8c, can be recognized.

The inspection of the spin magnetic moment, as well as the Bader charge analysis are recognized to be useful tools for the characterization of supported metal catalyst properties; in the here reported case the $h\text{-BN}$ supported Pd_6 retains the same total spin magnetic moment of $2.0 \mu_B$ that can be found *in vacuo*, while according to the performed Bader charge analysis, a negligible charge transfer between the cluster and the support has been found. It is interesting to compare this latter result with the findings of Prestianni *et al.* [109] regarding the interaction of a Pd_{30} cluster on a BNNT surface, in which a negative charge transfer from the support to

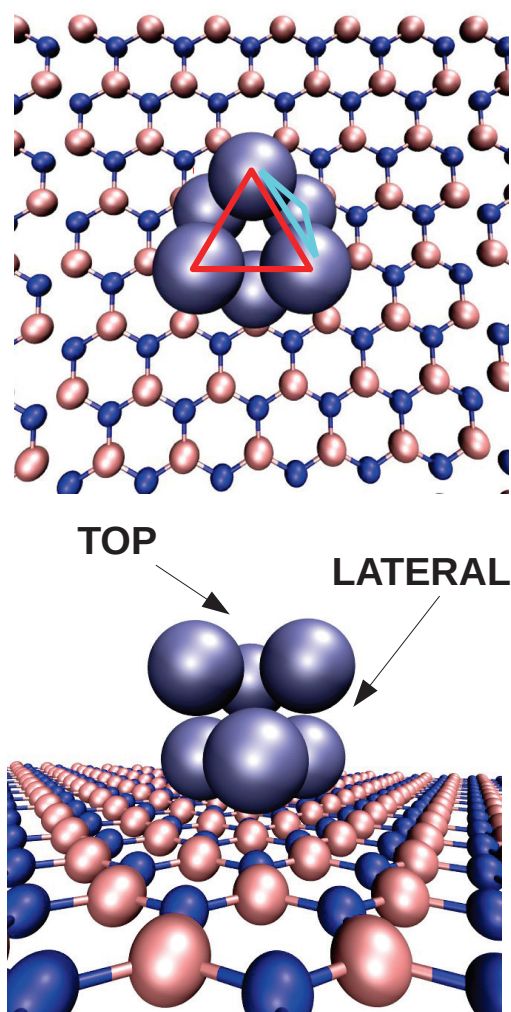


Figure 3.7 – Optimized structure of the *h*-BN supported Pd₆ cluster. On the upper panel the top view of the cluster is showed. The red triangle indicate the "top" face of the cluster while the cyan triangle, the "lateral face". These two are highlighted in the bottom panel, showing the structure from a frontal perspective.

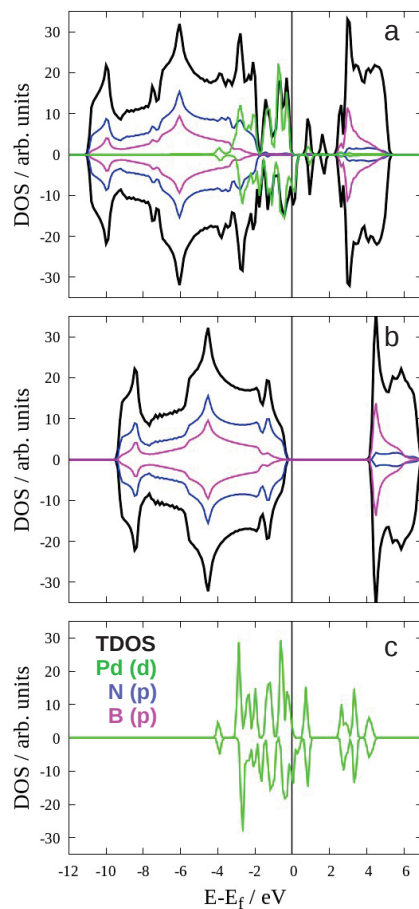


Figure 3.8 – Projected Density of States plot of a) h -BN supported Pd_6 ; b) h -BN sheet support; c) Pd_6 cluster optimized *in vacuo*; total DOS (TDOS) obtained as the sum of each PDOS contribution are showed in black, palladium (4d) states in green, boron (2p) states in pink and nitrogen (2p) states in blue. Fermi energy was taken as reference.

the catalyst has been recognized. This means that, on the whole, the amount of charge transfer may be related to both the size of the cluster and the intrinsic curvature of the support.

Formic acid adsorption

The stability of different formic acid coordination modes on the cluster has been evaluated in terms of adsorption energy. It has to be stressed that of the six Pd atoms of the cluster, three are directly interacting with the nitrogen atoms of the support; thus, it is reasonable that their properties may differ from the other three Pd atoms being further from the *h*-BN sheet. Thus, in order to account for this neighbourhood difference we chose to perform the adsorption and the associated reactivity study on two different face of the cluster: the "top" face is the triangular face whose properties should not be affected by the presence of the support, while the triangular "lateral" face is made up of two BN-interacting Pd atoms and a "top" one, as shown in Figure 3.7.

It has been already demonstrated in the literature for various metallic surfaces [110] that formic acid can be found in two different limiting adsorption modes: a perpendicular mode in which both the hydroxyl and carbonylic groups interact with the metal in a bidentate way (HCOOH*) and another one in which FA lies parallel on the surface (HCOOH_(flat)). When FA shows the perpendicular binding mode, the *trans* isomer has been found to be reactive toward the formate mediated decomposition, while in the case of parallel adsorption, the *cis* configuration, has been found to be the precursor of the carboxylic mediated dehydrogenation. The same HCOOH* and HCOOH_(flat) structures have been optimized on the Pd₆ cluster; they are reported in Figure 3.9. On the top face, the bidentate mode has an adsorption energy of -82.4 kJ mol⁻¹ while the parallel one showed a value of -46.3 kJ mol⁻¹. These two results can be compared with those of Scaranto *et al.* [111] dealing with a Pd(111) surface, that found, for the same bidentate and parallel configurations, adsorption energies of -39.6 and -2.9 kJ mol⁻¹; even considering the contribution due to the dispersion interactions, lacking in the previous study and here accounted with the Grimme-D3 semiempirical corrections, it is reasonable to infer that this difference may be attributed to the higher reactivity of the cluster atoms, that differently from the surface are naturally undercoordinated. Others limiting structures, in which only one between the hydroxyl and carbonylic moieties interacts with a Pd atom were optimized, resulting 44.6 and 55.3 kJ mol⁻¹ less stable than that showing a bidentate binding mode. According to these findings, the carbonylic moiety interacts more strongly with Pd than the hydroxyl one.

On the lateral side of the cluster three different structures showing bidentate binding modes have been optimized. Indeed the two FA oxygens can interact with the Pd atoms of this face in three different ways: i) both the carbonylic and hydroxyl moieties can be adsorbed on the N interacting Pd atoms; ii) the carbonylic moiety can be adsorbed on the N interacting Pd atoms while the hydroxyl with the Pd atom belonging to the top face or iii) the exact opposite. We found that the optimized structures arising from case ii) and iii) are nearly isoenergetic being the FA adsorption energy -103.9 and -99.4 kJ mol⁻¹ respectively; instead the guess

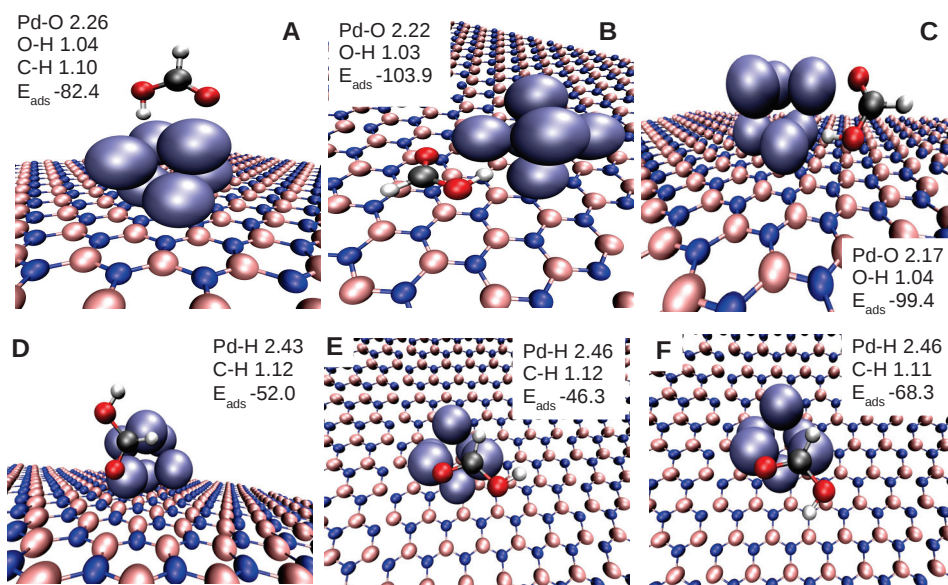


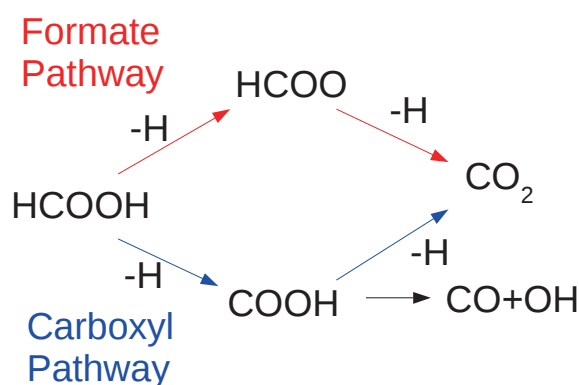
Figure 3.9 – Optimized structures of FA in its most important adsorption modes: A) bidentate mode on the top face; B) and C) bidentate mode on the lateral face, with opposite carbonyl/hydroxyl coordination; D) parallel mode ($\text{HCOOH}_{(flat)}$) on the lateral face; E) parallel mode ($\text{HCOOH}_{(flat)}$) on the top face (*cis*); F) Parallel mode ($\text{HCOOH}_{(flat)}$) on the top face (*trans*). For each panel, relevant bond lengths (in Å) and adsorption energy (E_{ads} , in kJ mol^{-1}) are reported.

3.2. Part II - Reactivity of formic acid on *h*-BN supported Pd₆ catalyst

structure provided in case i) converts naturally into ii) after optimization. It has to be noticed that FA adsorbs more strongly on the lateral face than on the top one by approximately 20 kJ mol⁻¹; the *cis* parallel adsorption mode on the lateral face instead adsorbs as strongly as on the top face, being its adsorption energy only 5.7 kJ mol⁻¹ higher. The differences reported in terms of adsorption energies, comparing multiple sites of the cluster, may be important for further analysis regarding the activity and selectivity toward the formation of specific compounds and for sure it is a key factor to take into account in more comprehensive methods such as microkinetic or kinetic Monte Carlo approaches. Instead, from the simple inspection of adsorption energies, thus thermodynamic quantities, a reasonable picture before the decomposition reaction takes place, is that the perimetral sites, directly in contact with the support, could be the first to be occupied by FA, while the top sites could be covered only after.

Formic acid decomposition

The metal catalyzed FA decomposition, whose general reaction pathway is reported in Scheme 3.2, has been deeply studied and debated in the literature. In order to study the reaction mechanism, the competition between formate (HCOO) and carboxylate (COOH) pathways and the different reactivity of top and perimetral sites of the cluster, the following procedure was here used: i) reaction intermediates and transition states associated to the first hydrogen loss on the HCOO and COOH pathways were optimized on the top and lateral faces of the cluster, according to the convention highlighted in Figure 3.7; ii) the final state (F.S.) of the first molecular event was reoptimized varying the adsorption site (each exposed Pd₆ face) of the lost hydrogen atom; iii) the most stable configuration found was used as best initial state (B.I.S.) for the subsequent hydrogen breaking step.



Scheme 3.2 – Reaction scheme for formic acid decomposition.

Top Face - Formate Pathway

From the previously reported bidentate adsorption mode, FA can decompose through the formate pathway, beginning with an O-H bond breaking; on the top face of the cluster, it was

Chapter 3. Computational Design of a Boron Nitride Supported Pd Catalyst

estimated that this process requires the overcoming of an activation barrier of 26.6 kJ mol^{-1} , leading to the formate species; this is stabilized by 41.0 kJ mol^{-1} with respect to the adsorbed FA reference, as shown in Figure 3.10.

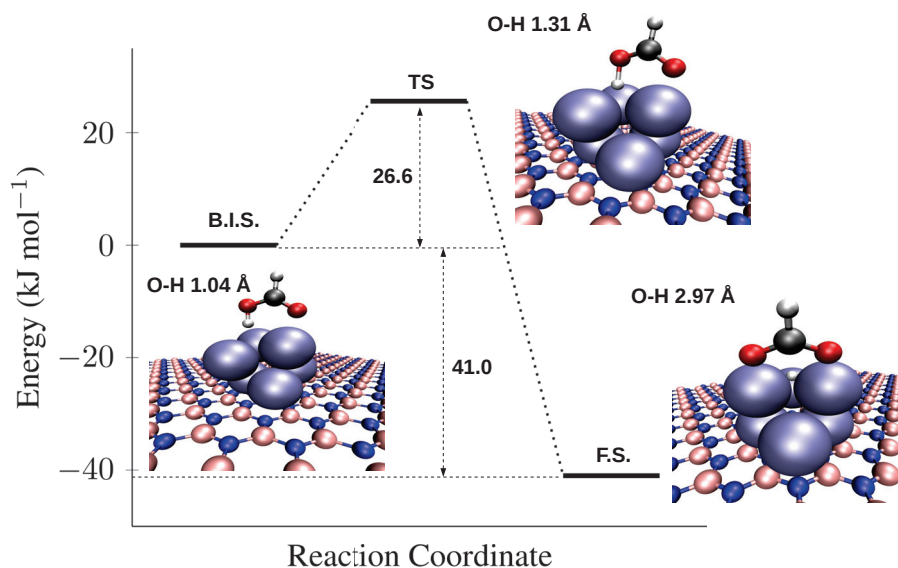


Figure 3.10 – Reaction coordinate for the $\text{HCOOH} \rightarrow \text{HCOO} + \text{H}$ step on the top face of the supported Pd_6 cluster. The optimized structures of the B.I.S., TS and final state (F.S.) are reported in the insets, with relevant geometrical descriptors.

At this point, in order to lose also the second hydrogen atom, through a successive C-H bond breaking, a coordination change should occur; indeed, in the bidentate mode, the C-H bond is too far from the cluster to be activated by the metallic species. As it is possible to see from Figure 3.11, this reaction step, which is common also on metallic surfaces [59, 44, 110, 111], requires $108.4 \text{ kJ mol}^{-1}$. The monodentate mode, characterized by the proximity of the remaining hydrogen to a palladium atom (being the Pd-H distance 1.89 \AA), is 75.3 kJ mol^{-1} less stable than the bidentate one; this difference can be reasonably ascribed to the breaking of a really stable Pd-O bond. The subsequent C-H bond cleavage requires 27.6 kJ mol^{-1} leading to a final state in which the hydrogen atom interacts atop with a palladium one; this structure has the highest destabilization along the reaction path, being 13.7 kJ mol^{-1} less stable than than its precursor, the monodentate formate; indeed, in agreement with the literature hydrogen on Pd cluster prefers to adsorb with a threefold coordination [112, 113]. The best final state (B.F.S.), reported in Figure 3.13A, shows both the hydrogen atoms adsorbed on the Pd_6 faces while CO_2 is almost desorbed from the top face cluster, being the Pd-O bond distance longer than 3.0 \AA .

3.2. Part II - Reactivity of formic acid on *h*-BN supported Pd₆ catalyst

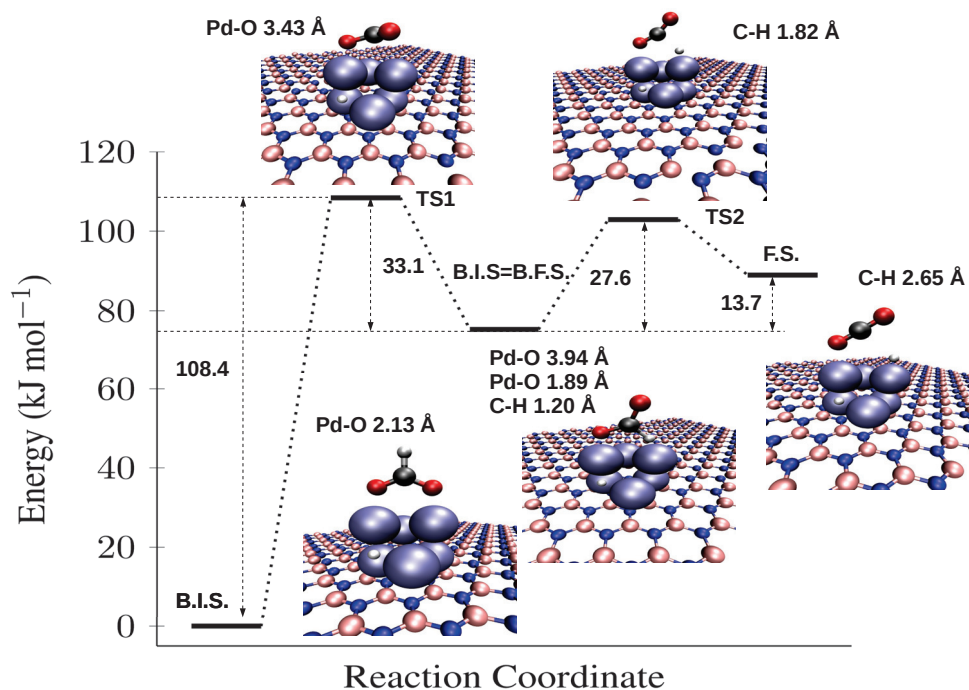


Figure 3.11 – Reaction coordinate for the HCOO → CO₂ + H step, (through a coordination change step) on the top face of the supported Pd₆ cluster. The optimized structures of B.I.S., TS and (B.)F.S. are reported in the insets, with relevant geometrical descriptors.

Top Face - Carboxyl Pathway

Starting from the FA parallel adsorption mode, the carboxylate species can be formed overcoming an activation barrier of 26.6 kJ mol^{-1} . The product of this molecular event shows the hydrogen atom atop coordinated to a Pd one, being their bond distance 1.59 \AA while the carboxylate interacts via the carbon atom with the same Pd with a Pd-C bond distance of 1.95 \AA ; this particular configuration, really similar to that previously found in the literature on a Pd(111) surface [111], allows also the interaction of the carbonylic oxygen with the Pd cluster (their bond distance is 2.24 \AA); all these features contribute to an overall stabilization of this reaction intermediate by 31.4 kJ mol^{-1} with respect to the initial state (I.S.). Instead, as above mentioned, the atop coordination of the adsorbed hydrogen is unfavoured and thus in the optimized B.F.S. the hydrogen atom shows a threefold coordination.

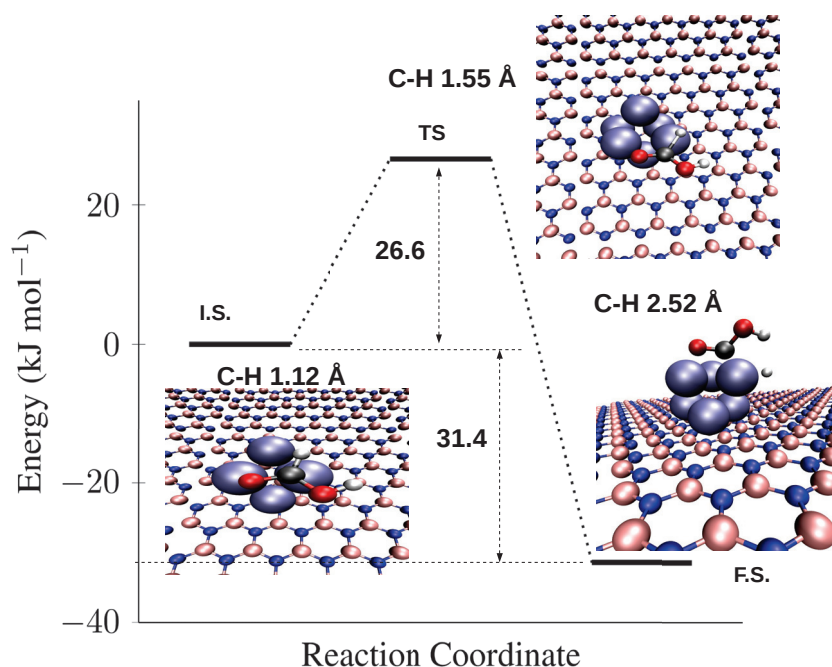


Figure 3.12 – Reaction coordinate for the $\text{HCOOH} \rightarrow \text{COOH} + \text{H}$ step on the top face of the supported Pd_6 cluster. The optimized structures of I.S., TS and F.S. are reported in the insets, with relevant geometrical descriptors.

It should be noticed also that in the B.F.S. the carboxylic fragment, shows a geometry suited for a further reaction step, since the hydroxyl moiety points directly toward one of the face of the Pd_6 . Accounting both the hydrogen coordination change and the carboxyl rearrangement, the B.F.S. resulted to be 10.0 kJ mol^{-1} more stable than the previously shown final state. The second dehydrogenation step requires 46.4 kJ mol^{-1} ; it is an exoergic process, being the B.F.S. 34.2 kJ mol^{-1} more stable than the initial one. Interestingly, it was possible to find the produced CO_2 in a peculiar bent geometry, shown in Figure 3.13B. According to Ko *et al.*

3.2. Part II - Reactivity of formic acid on *h*-BN supported Pd₆ catalyst

[114] this particular geometry arises from the negative charge transfer from the metal to the antibonding orbitals of CO₂; this is the preferred geometry also on reduced ceria support [115]. The stability of this structure with respect to the classical linear geometry depends on the specific metal: as an example on Ru(0001) the bent structure is more stable than the linear one while, on Pd(111) and on Ni(111) the physisorbed linear CO₂ is favoured [116]. On Pd₆ instead, the bent structure resulted 53.8 kJ mol⁻¹ more stable than the linear.

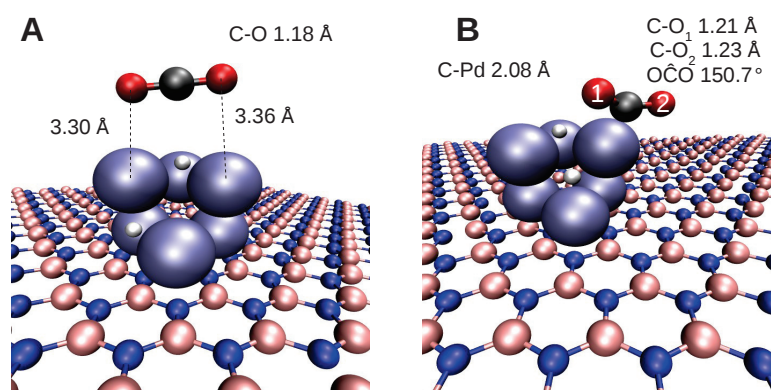


Figure 3.13 – Optimized structure of CO₂; A) linear geometry; B) bent (or v-shape) geometry. Relevant geometrical parameters are reported in the insets.

Finally, it should be mentioned that on the COOH pathway, the complete dehydrogenation is not the only possible fate for the carboxyl decomposition; indeed COOH can otherwise form CO and OH through a C-O bond breaking. As reported in Figure 3.14, this molecular event has been calculated to require 72.3 kJ mol⁻¹ to occur, approximately 30 kJ mol⁻¹ more than the previously illustrated O-H bond breaking. For this reason it won't be further treated along the thesis.

Perimetral sites reactivity

One of the first effect that a specific support could exert on subnanometric size catalyts, before invoking more specific processes involving charge transfers or reconstruction, is the removal of the symmetry that the sub-nanoparticles show when unsupported. In the case of Pd₆, despite retaining a nearly octahedral structure, it is intuitive that the Pd atoms interacting with the support may show different catalytic properties than those belonging to the "top face". The PEC and optimized structures of TSs and reaction intermediates relative to the HCOO or COOH mediated decomposition of FA on the perimetral sites of the cluster, are reported in Figure 3.15 and Figure 3.16.

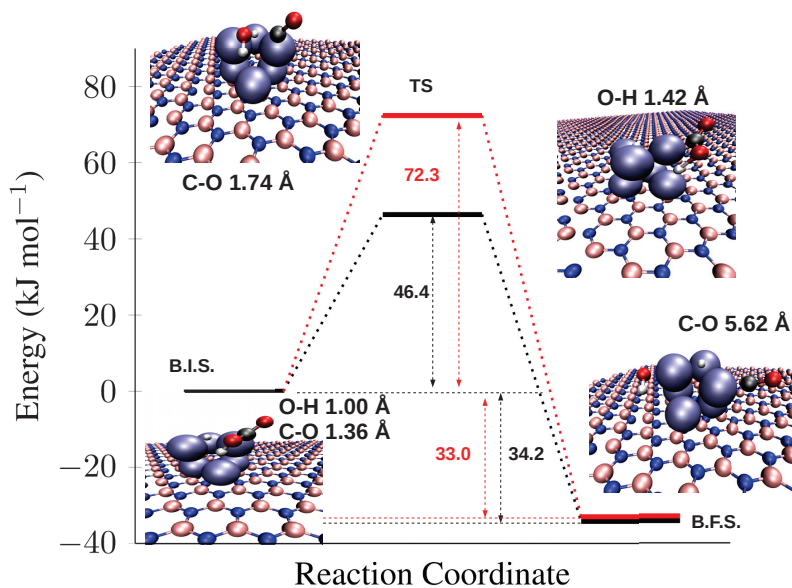


Figure 3.14 – Reaction coordinate for the $\text{COOH} \rightarrow \text{CO}_2 + \text{H}$ (black) and $\text{COOH} \rightarrow \text{CO} + \text{OH}$ (red) steps on the top face of the supported Pd_6 cluster. The optimized structures of B.I.S., TS and B.F.S. are reported in the insets, with relevant geometrical descriptors.

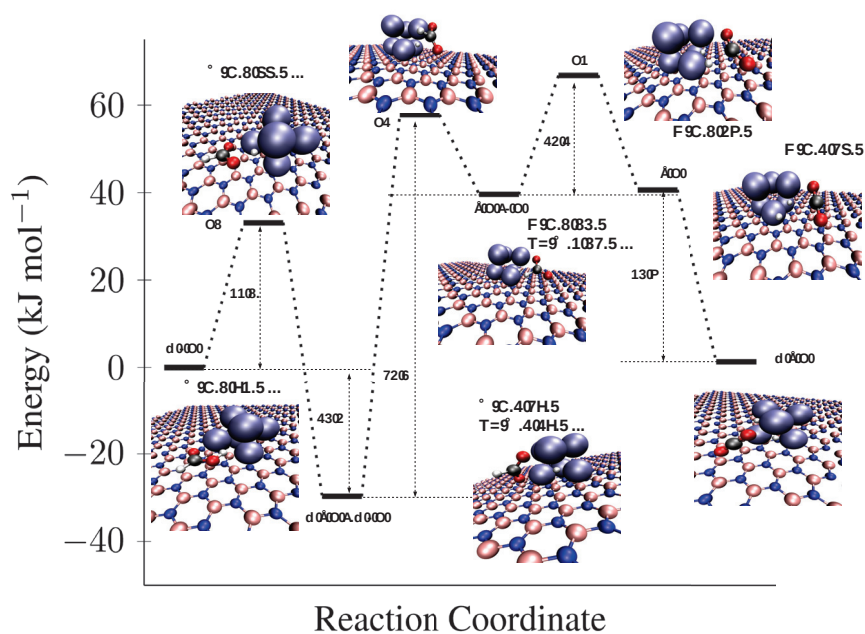


Figure 3.15 – Potential energy curve for FA decomposition through the HCOO pathway on the lateral side of the cluster. The optimized structures of (B.)I.S., TS and (B.)F.S. are reported in the insets, with relevant geometrical descriptors.

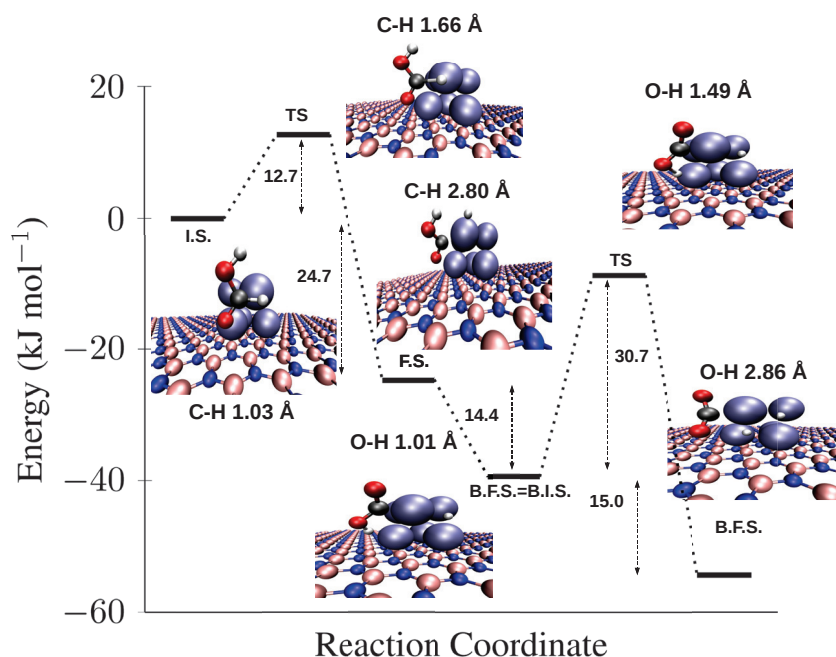


Figure 3.16 – Potential energy curve for FA decomposition through the COOH pathway on the lateral side of the cluster. The optimized structures of (B.)I.S., TS and B.F.S. are reported in the insets, with relevant geometrical descriptors.

Following the formate pathway, in order to produce HCOO from the initial adsorbed formic acid, an activation barrier of 33.1 kJ mol^{-1} has to be overcome and the reaction, just as in the case of the top face, is exoergic, being the final HCOO+H state stabilized by 29.7 kJ mol^{-1} . From this, the bidentate to monodentate conversion occurs through an elementary step characterized by an activation barrier of 87.5 kJ mol^{-1} ; similarly to what found on the top face, the process is endoergic: the final state is 69.3 kJ mol^{-1} higher in energy than the initial. The final dehydrogenation requires instead 27.2 kJ mol^{-1} .

FA can dehydrogenate following the carboxyl pathway on the side of the cluster, through a C-H bond breaking step requiring a really low activation barrier of 12.7 kJ mol^{-1} ; noticeably this value is 13.9 kJ mol^{-1} lower than that found on the top face of the cluster. Despite a deeper discussion regarding site reactivity will be reported later in the chapter, we can anticipate that the difference found in this case can be ascribed to a destabilization of the initial state, the adsorbed FA, on this side of the cluster respect to the top face. The carboxyl fragment formed upon the first dehydrogenation is atop coordinated to a Pd atom (1.95 \AA) and the dissociated hydrogen is coordinated to the same metallic site. In B.F.S., a structural rearrangement of the carboxyl as well as the hydrogen coordination change (from atop to threefold) result in an overall stabilization of 14.4 kJ mol^{-1} . Differently from the F.S. the hydroxyl in this

conformation points toward the lateral side of the cluster and thus a further dehydrogenation step is conceivable. This molecular step has an activation barrier of 30.7 kJ mol^{-1} and is slightly exoergic, being the B.F.S stabilized by 15.0 kJ mol^{-1} . This corresponds to a structure in which the CO_2 is in the already encountered v-shape geometry, while both the lost hydrogen atoms are coordinated to one of the Pd_6 triangular faces.

Discussion

Size sensitivity

It is interesting to compare the here presented results with previous studies dealing with FA decomposition on a Pd(111) surface. Indeed, this should allow to rationalize the effect of the sub-nanometric size of the cluster on the overall reactivity. Moreover, since nanoparticles often undergo nucleation and growth processes, the Pd_6 case could be informative for understanding the reaction mechanism at the very early stage, while the catalyst properties may evolve toward those of a Pd plain surface only later. The PEC of the HCOO pathway on the supported Pd_6 and on a Pd(111) surface (adapted from Scaranto *et al.* [111]) are reported in Figure 3.17 while the corresponding comparison for the COOH pathway is reported instead Figure 3.18.

A first inspection of the PEC relative to the formate pathway allows to draw two conclusions showing the pronounced difference between this reaction branch on the cluster and on the surface: first, on Pd_6 the HCOO pathway is stabilized with respect to the surface, with differences in energy that can reach approximately 50 kJ mol^{-1} in the case of the adsorbed formate. Then, aside from the energetics, also the number of elementary steps in the reaction mechanism is different, indeed in the case of the cluster mediated decomposition there is one step more. On Pd(111) it has been instead reported that once the formate converts from bidentate to the monodentate conformation, dehydrogenation leading to CO_2 is spontaneous, without passing from a connecting transition state, differently to what already discussed for the cluster. In that respect, it should be noticed that while on Pd(111) both TS1 and the monodentate FA are energetically well above the reference FA unadsorbed state, the same are instead stabilized on the cluster. This very likely thanks to a stronger interaction of these reactive species with the cluster caused by the presence of more undercoordinated metal atoms with respect to a surface model. For the same reason, some interesting differences arise also on the activation barriers of selected steps: as an example the energetic requirement for the first dehydrogenation is considerably lower on the cluster (25.6 vs 57.9 kJ mol^{-1}); instead due to the enhanced interaction between oxygen and palladium the activation barrier for the coordination change resulted 18.9 kJ mol^{-1} higher on the cluster.

3.2. Part II - Reactivity of formic acid on *h*-BN supported Pd₆ catalyst

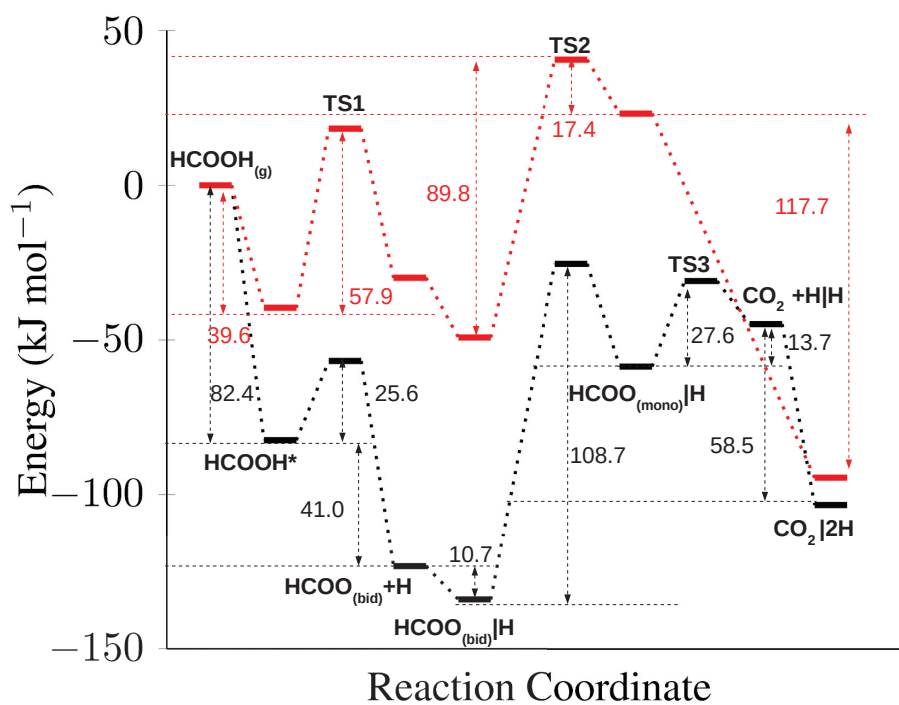


Figure 3.17 – Potential energy curve for the HCOOH decomposition, through the formate (HCOO) pathway on the *h*-BN supported Pd₆ cluster (black lines) and on a bare Pd(111) surface (red lines, adapted from Scaranto *et al.* [111]); the vertical bar notation (A|B) indicates the most stable configuration of A and B coadsorbed on the cluster.

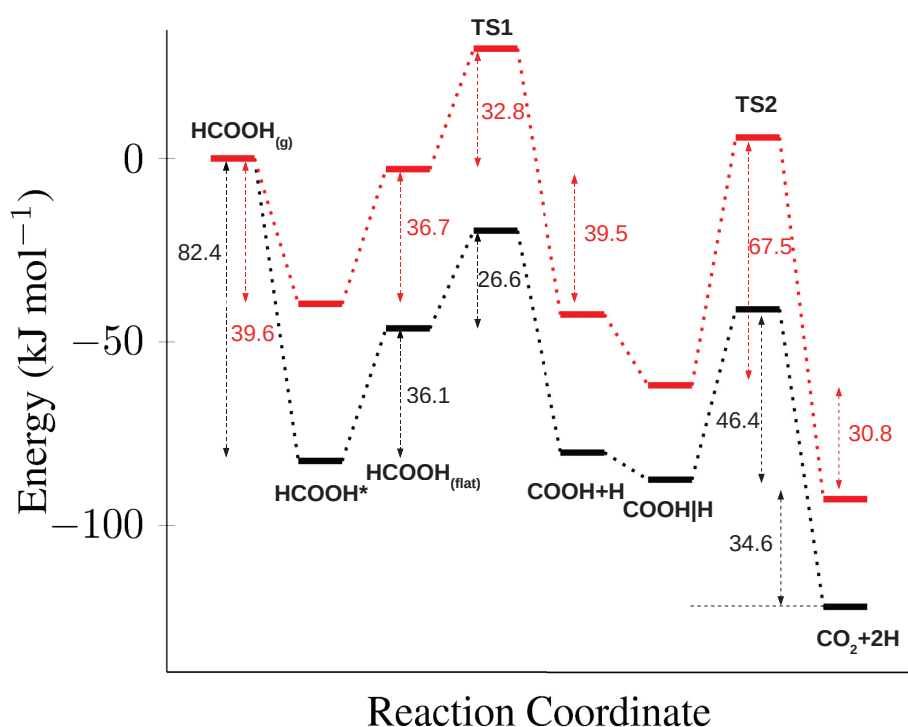


Figure 3.18 – Potential energy curve for the HCOOH decomposition, through the carboxyl (COOH) pathway on the *h*-BN supported Pd₆ cluster (black lines) and on a clean Pd(111) surface (red lines, adapted from Scaranto *et al.* [111]); the vertical bar notation (A|B) indicates the most stable configuration of A and B coadsorbed on the cluster.

In the case of the carboxyl pathway, the differences between the plain surface and the cluster are more contained. Apart from an overall stabilization of the reaction intermediates and transition states, in the same terms discussed for the HCOO pathway, the reaction mechanism shows no relevant differences, with the only exception of the activation barrier for the second dehydrogenation step, which is slightly higher on the Pd(111) surface (21.4 kJ mol⁻¹). Instead, for the first dehydrogenation step the energetic requirement is nearly identical in the two cases, with a difference within 7 kJ mol⁻¹; this is reasonably due to the geometrical features that TS1 shows both on the cluster and surface: in particular the C-H bond lies almost exactly on a single metal atom, in a sort of η^2 coordination between C,H and Pd. As a matter of fact, the same TS coordination mode has been found recently by He and Hua Li [117], that studied, within a variety of exchange-correlation functionals, a monoatomic Pd catalyst for FA decomposition and according to their results the above mentioned TS structure is that associated to the lowest activation barrier for the COOH pathway.

Competition between HCOO and COOH pathways

The PEC for the HCOOH dehydrogenation through the two selected pathways are displayed in Figure 3.19; these are relative to the top face reaction, while the perimetral sites reactivity will be discussed later in the text, for the sake of clarity. Some peculiar features of the reactivity on the cluster can be discussed from the simple analysis of the PEC. As an example, we can reasonably predict that a decomposition through the formate channel could be expected. Indeed, although the energetic requirement for the FA first dehydrogenation is approximately the same in the two pathways, in order to react through a carboxylic mediated mechanism, FA would require to change its most stable adsorption mode to the metastable nearly parallel (HCOOH_(flat)) conformation. Moreover, it is worth noting the high stabilization of the formate-hydrogen coadsorbed state with respect to the carboxyl-hydrogen one. This is a rather unexpected result since, to the best of our knowledge, the wide majority of the literature concerning FA decomposition on Pd or Pt surfaces, reports a stabilization of the carboxyl intermediate with respect to the formate [111, 110]. This energetic difference of 37.1 kJ mol⁻¹ in their B.F.S. corroborates the hypothesis of a formate mediated decomposition. Interestingly Xia and coworkers have reported that the HCOO-COOH energy levels difference is structure sensitive: the carboxyl resulted to be more stable than formate both on Pd(111) and Pd(100) but the difference is pronounced only on more open surfaces while it tends to flatten on a (211) stepped surface [35]; independently, Ju Li *et al.*, have found the same trend in the carboxyl-formate stability, on an unsupported Pd₇ [118]. These findings, together with our calculations, suggest that the preferential stabilization of one or the other intermediate could depend from the presence of undercoordinated metal sites. In fact, a similar trend has been found also for copper [59]: in this case HCOO becomes more stable than COOH passing from a (100) to a (111) surface and this difference is maintained also in the case of alumina supported sub-nanometric Cu₄ clusters [63].

This feature could be a key factor for indirectly avoiding carbon monoxide poisoning, since the high thermodynamic stability of HCOO should prevent the reaction flux to pass from the COOH intermediate, which is generally more reactive toward CO-OH bond breakings. However, even if FA undergoes through a carboxyl mediated decomposition, the activation barrier for the CO-OH bond breaking from COOH has been estimated to be 25.9 kJ mol⁻¹ higher than that associated to the dehydrogenation. Thus, at this level, we could conclude that CO poisoning should not be a major issue. Despite this, the high energy requirement for the formate coordination change as well its high degree of stabilization suggests, at this stage, possible formate poisoning.

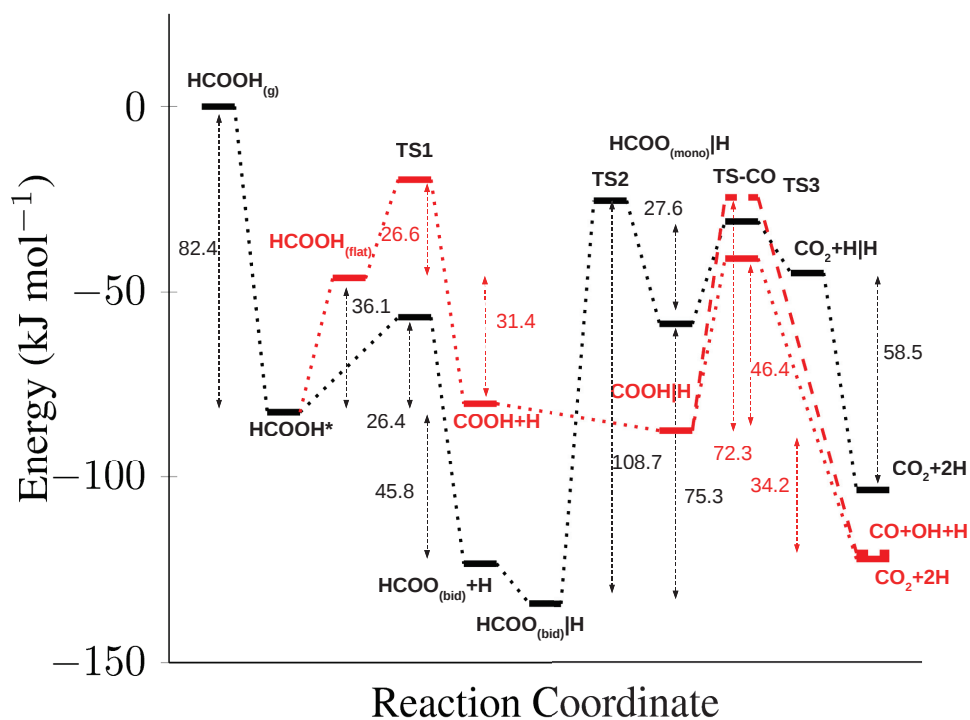


Figure 3.19 – Potential energy curve for the HCOOH decomposition, through the HCOO (black lines) and COOH (red lines) pathways, on the top face of the *h*-BN supported Pd₆ cluster; the dashed red line is associated to the C-O bond breaking from COOH, leading to CO+OH; the vertical bar notation (A|B) indicates the most stable configuration of A and B coadsorbed on the cluster.

3.2. Part II - Reactivity of formic acid on *h*-BN supported Pd₆ catalyst

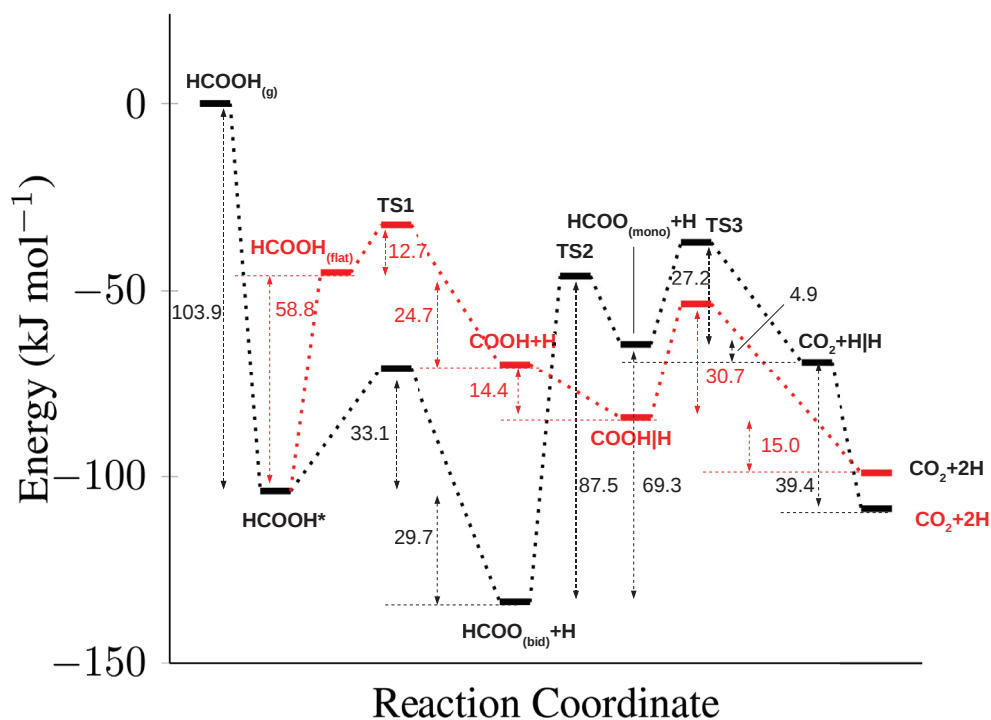


Figure 3.20 – Potential energy curve for the HCOOH decomposition, through the HCOO (black lines) and carboxyl (red lines) pathways, on the lateral side of the *h*-BN supported Pd₆ cluster; the vertical bar notation (A|B) indicates the most stable configuration of A and B coadsorbed on the cluster.

A complete picture of the catalyst activity and selectivity toward the formation of CO₂ cannot be traced without taking into account also the perimetral sites reactivity. In Figure 3.20 the PEC for the HCOO and COOH decomposition pathway on the side of the cluster has been reported. The conclusions regarding the reaction mechanism as well as the energetics are pretty similar to what already discussed for the top face reactivity; in fact, some slight differences can be found, but at this stage it is rather hard to understand how much this can affect the entire reactivity. For sure, it is evident a significant decrease of the activation barrier required for the bidentate HCOO to change coordination mode, passing from 105.0 kJ mol⁻¹ found on the top face to the more affordable value of 87.5 kJ mol⁻¹. A decrease of similar magnitude can be also found both for the first and second dehydrogenation steps of the COOH pathway: in the former case a stabilization of TS1 and in the latter, a destabilization of the carboxyl initial state contributes to lowering the activation barriers. This last evidence, together with the stabilization of TS2 suggests the weaker interaction of this species with metallic cluster and reasonably, this may be ascribed to the support effect: the Pd atoms interacting with the *h*-BN are more coordinated than the others and this likely affect both the energy required to break the Pd-O bond (*e.g.* TS2) and the stability of the adsorbed intermediate (*e.g.* carboxyl).

A similar correlation between coordination and catalytic activity was also scrutinized by Fampiou and Ramasubramaniam for a defective graphene supported Pt₁₃ cluster [119].

Hydrogen spillover

Finally, in this section we will briefly discuss how hydrogen could diffuse through the studied system. In particular, due to the high stability of formate it is interesting to verify what is the influence of a coadsorbed HCOO (top-face coordinated) on the diffusion mechanism of a H atom through the cluster or onto the support.

A first conclusion can be drawn regarding the spillover toward *h*-BN: irrespective of the HCOO presence, all the structures in which a hydrogen atom is adsorbed on a N or B atom in the proximity of the cluster converge into structures in which the hydrogen interact with Pd₆ after full optimization. In particular, H shows the already encountered threefold coordination on the cluster face nearest to the support. Optimizing H on a N or B atom farther from the cluster (approximately 6.0 Å away from the Pd-N anchoring point), we obtained two structures characterized by an atop N and B coordination, being their bond distances 1.04 and 1.37 Å. These two structures resulted 250.6 and 265.3 kJ mol⁻¹ less stable than most stable HCOO+H coadsorbed state found on the cluster. Of course these are strong evidences of the preference of hydrogen to interact with the Pd species, at least in these specific coverage conditions. In fact, Yakobson *et al.* [120] have shown for a graphene supported Pd₄ cluster that H spillover onto the support is thermodynamically unfavourable at low hydrogen coverage, while it starts to be a competing mechanism increasing the number of adsorbed H₂ molecule or exploiting the presence of graphitic islands.

On the cluster instead, a hydrogen atom can diffuse from one face to another through the connecting edge of the octahedron. In Figure 3.21, a schematic picture of the process is presented, for the analyzed cases, with and without a co-adsorbed formate molecule; for the sake of clarity the Pd₆ structure has been approximated to be a perfect octahedron and displayed through a net representation. On the clean cluster, H shows moderate activation barriers for the diffusion that are generally decreased upon the adsorption of formate, suggesting a repulsive interaction between the two adsorbed species. The diffusion barrier that shows the higher variation is associated to the mechanism that involves the edge site (*bc*) coordinated to the formate oxygens; indeed, on the clean cluster the barrier resulted 29.7 kJ mol⁻¹ lower. As regard the thermodynamic stability, on the naked cluster, all the investigated threefold sites resulted more or less isoenergetic (within the limit of 4 kJ mol⁻¹). Instead, once the formate is produced, the hydrogen atom prefers to adsorb on the *cde* face, in which two of the three Pd atoms interact with a N, belonging to the support. Indeed, this structure resulted approximately 10.7 kJ mol⁻¹ more stable than the other three investigated and shown in Figure 3.21; lastly, the diffusion from the top (*abc*) face to the center of the cluster was investigated as well; although not really treated in the literature for subnanometric clusters, this mechanism could be reminiscent of the really common subsurface hydrogen migration, well studied in the case of surfaces. As expected, both on the clean and formate covered cluster, this particular

3.2. Part II - Reactivity of formic acid on *h*-BN supported Pd₆ catalyst

interaction site is thermodynamically unfavoured, being 36.0 kJ mol⁻¹ less stable than the reference adsorption mode (threefold coordination on the *cde* face). The activation barrier for the diffusion resulted instead 37.0 kJ mol⁻¹ on the clean cluster or 28.1 kJ mol⁻¹ if the formate presence is taken into account. Given these findings it can be noticed that all the diffusion barriers are much lower than the energy required for the formate coordination change necessary for the continuation of the decomposition on this pathway; thus, the diffusion should not have a deep influence on the overall reaction mechanism.

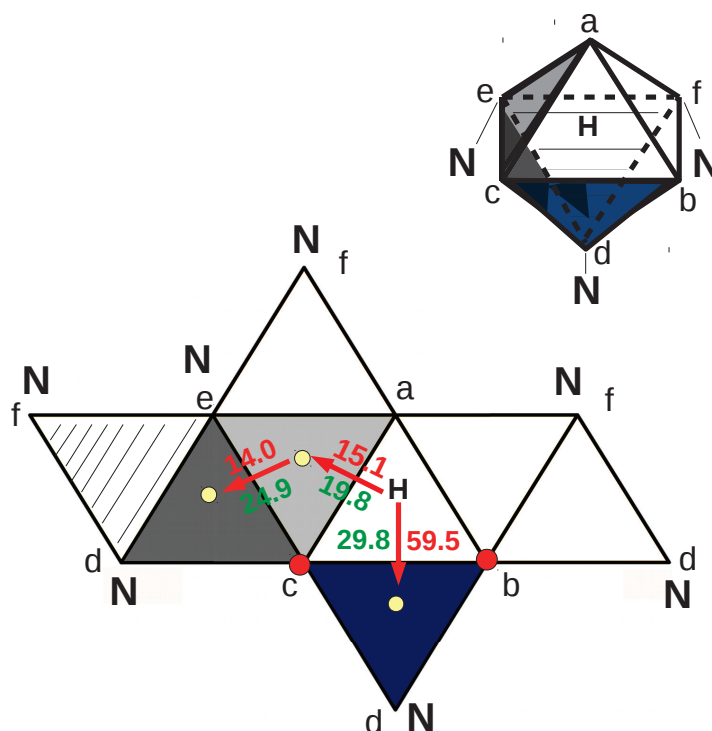


Figure 3.21 – Diffusion barriers (in kJ mol⁻¹) of hydrogen from the top face, to different threefold sites of the cluster, in presence (red) or without (green) HCOO. The final site of adsorption is indicated as a yellow circle and when HCOO is present, the oxygen adsorption sites are shown with red circles. Pd₆ is displayed through a net representation; each face is discriminated by a different color and the vertices (Pd atoms) labeled with a letter (a-f); a N was reported when that specific atom interacts with a nitrogen of the support. For the sake of clarity the three dimensional octahedral structure (approximated as a perfect octahedron) of Pd₆ is reported in the upper part of the figure, with the same letters and colors codes.

Part III - Reactivity of formic acid on a defective *h*-BN supported Pd₆ catalyst

Computational Details

The computational protocol here employed is the same of that used in Part II of this chapter. The boron defective *h*-BN sheet, from now on abbreviated *h*-B_VN, was obtained removing a B atom from the previously optimized BN sheet, as treated in Part II. In order to assess the transferability of the computational setup in the case of a defective system, some tests were carried out. In particular, the boron and nitrogen vacancy formation energy were computed, being respectively 16.6 and 12.8 eV (corresponding to 1601.9 and 1235.2 kJ mol⁻¹), in close agreement with the literature [121]. Ouyang and Song reported the *h*-B_VN sheet total magnetic moment dependency on the applied lattice strain [122]. Their results on a unstrained boron vacancy defected system were correctly reproduced by the method here chosen, being the calculated total magnetic moment 3.0 μ_B in both cases.

The adsorption energy E_{ads} of the palladium cluster on the *h*-B_VN sheet was calculated by means of the following equation:

$$E_{ads} = E_{TOT} - E_{V_B} - E_{Pd_6} \quad (3.6)$$

where E_{TOT} is the total energy of the system, E_{V_B} is the energy of the B-defected BN sheet and E_{Pd_6} is the energy of the gas phase Pd₆ cluster. Using a similar expression, but taking the FA gas phase energy as reference and substituting the second term of Equation 3.6 with the energy of the supported Pd₆, the FA adsorption energy was calculated.

Results

Adsorption of Pd₆ on defective *h*-B_VN

Similarly to what reported for analogous N-doped carbon networks [101], with the removal of a boron atom the *h*-B_VN sheet exposes three unsaturated nitrogen atoms in a D_{3h} symmetry pocket, being the N-N bond distance 2.62 Å; the bond length between the unsaturated nitrogens and their vicinal boron atoms is 1.41 Å, approximately 0.04 Å shorter than that found in a perfect *h*-BN sheet or in the areas far from the defect. The introduction of the metal cluster in the system causes a distortion of the cavity and in particular the nitrogen atoms are subjected to a displacement on the *z* direction of 0.7 Å. According to Shevlin and Guo, this out of plane distortion, in BN based materials, can be attributed to a partial *sp*³ hybridization of the atoms [121].

The optimized structure of the *h*-B_VN interacting Pd₆ shows one of the Pd atom coordinated to

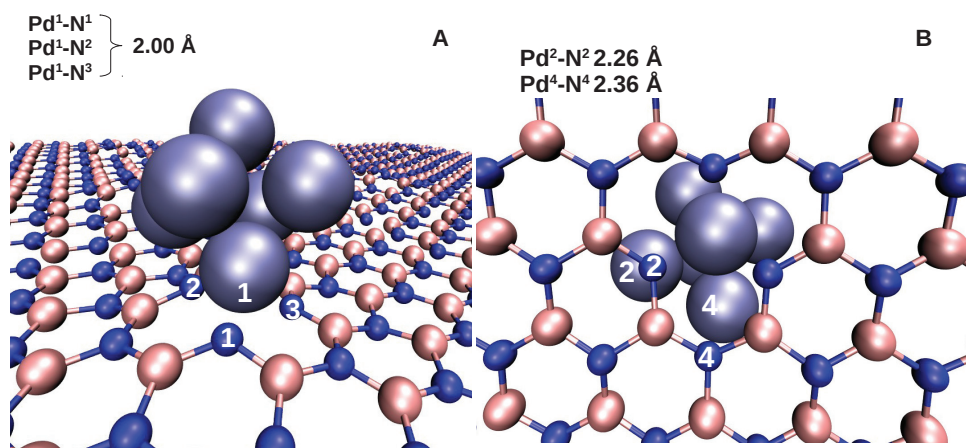


Figure 3.22 – Side (A) and bottom (B) view of the optimized structure of the *h*-B_VN supported Pd₆ cluster; relevant geometrical parameters are reported in the insets.

the three unsaturated N atoms, right at the center of the cavity, being the Pd-N bond distance 2.00 Å, as displayed in Figure 3.22A. The cluster results slightly tilted with respect to the surface; in this way other two Pd atoms, apart from that at the center of the cavity, can interact with the support, one with a Pd-N bond distance of 2.36 Å, the other with a Pd-N bond distance of 2.26 Å (see Figure 3.22B). The cluster, seems to retain a nearly octahedral geometry. An adsorption energy of 8.9 eV (858.9 kJ mol⁻¹) was calculated through Equation 3.6; this really high value demonstrates that the interaction between the defective sheet and the cluster is much stronger than that showed in Part II, when a perfect support is used. Indeed, in that case, Bader charge analysis demonstrated negligible charge transfer effects between cluster and support and the retaining of the cluster spin multiplicity with respect to the gas phase optimization was reported. Conversely, with the introduction of a boron vacancy, Bader charge analysis leads to the conclusion that a negative charge depletion from the cluster to the BN support occurs and as a consequence the Pd₆ shows a total positive charge of +0.87 |e⁻|; then, a spin quenching effect, lowering the total spin magnetic moment of the system from 3.0 (*h*-B_VN) and 2.0 (Pd₆) to 1.0 μ_B (Pd₆/*h*-B_VN) can be recognized. This is a quite common phenomenon occurring upon the interaction of metallic clusters and defective supports, such as in the case of graphene [67, 123].

Formic acid adsorption

As already discussed in Part II, FA, both on metallic clusters and surfaces, shows two different adsorption modes, namely perpendicular (HCOOH*) and parallel (HCOOH_(flat)). The former is energetically preferred and leads to a formate (HCOO) mediated decomposition pathway; the latter, usually less stable, is instead the precursor of the carboxyl (COOH) intermediate [111, 110]. On the *h*-B_VN supported Pd₆ cluster, the two configurations, whose optimized

Chapter 3. Computational Design of a Boron Nitride Supported Pd Catalyst

structures are reported in Figure 3.23, show adsorption energies of -73.8 (perpendicular) and -43.8 (parallel) kJ mol^{-1} ; these values can be compared with the results obtained for the defect-free BN sheet treated in the Part II, where adsorption energies of -82.4 and -46.3 kJ mol^{-1} were calculated respectively for HCOOH^* and $\text{HCOOH}_{(flat)}$. This means that by the introduction of the boron vacancy the FA adsorption energy slightly lowers.

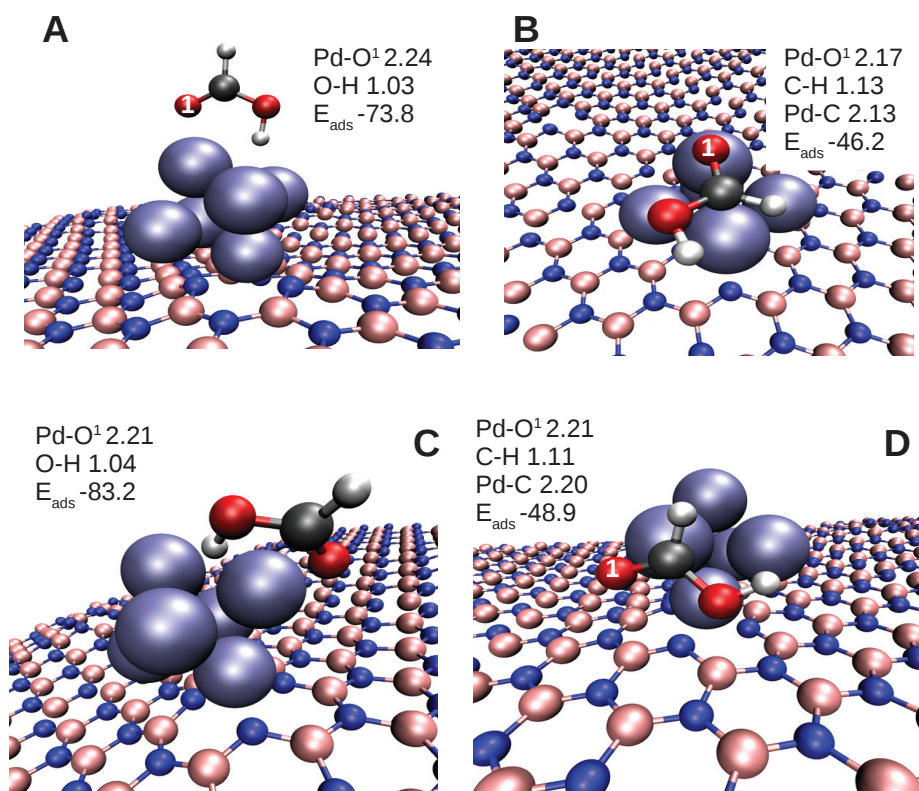


Figure 3.23 – Optimized structures of FA in its most important adsorption modes: A) perpendicular (HCOOH^*) and B) flat ($\text{HCOOH}_{(flat)}$) modes on the top face; C) perpendicular and D) flat modes on the lateral cluster face. For each panel, relevant bond lengths (in Å) and adsorption energy (E_{ads} , in kJ mol^{-1}) are reported.

It is important to remind that the Pd_6 catalyst properties may naturally depend on the reaction site considered; thus, similarly to what it has been already done for the defect-free system, two different faces of the octahedral cluster were analyzed, *i.e.* top and lateral. The adsorption energy of FA on this latter face resulted -83.2 kJ mol^{-1} for HCOOH^* and -48.9 kJ mol^{-1} for $\text{HCOOH}_{(flat)}$, thus really close to the results of the vacancy-free system.

Formic acid decomposition

The competition between HCOO and COOH decomposition pathways on the *h*-B_vN supported Pd₆ cluster has been studied both on its top face and perimetral sites. The procedure used is analogous to that reported in the Part II of this chapter based on: i) optimization of reaction intermediates and transition states for the first hydrogen loss; ii) reoptimization of the final state (F.S.) found in step i), varying the adsorption site of the produced hydrogen; iii) the most stable configuration obtained is used as best initial state (B.I.S.) for investigating the second hydrogen atom production step.

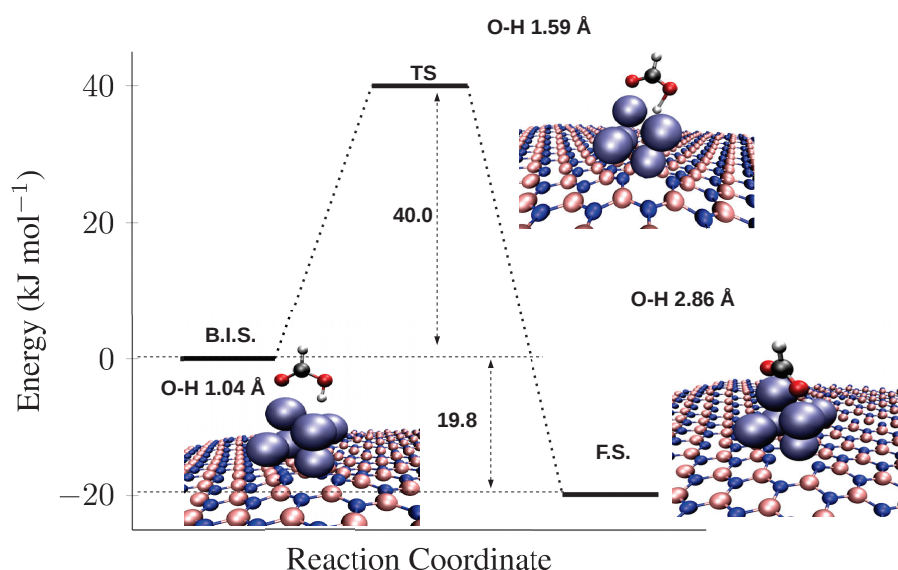


Figure 3.24 – Reaction coordinate for the HCOOH → HCOO + H step on the top face of the supported Pd₆ cluster. The optimized structures of B.I.S., TS and F.S. are reported in the insets, with relevant geometrical descriptors.

Top Face - Formate Pathway

HCOOH* can decompose to HCOO overcoming an activation barrier of 40.0 kJ mol⁻¹. This molecular process is exoergic and the final state is 19.8 kJ mol⁻¹ more stable than the adsorbed FA (see Figure 3.24). The activation barrier here found results approximately 15 kJ mol⁻¹ higher than that reported for the Pd₆/*h*-BN; the difference is even more evident comparing the stability of the formate reaction intermediate that on the defect-free supported Pd₆ cluster was 41.0 kJ mol⁻¹ more stable than the initial state.

As reported in the literature [111] and in Part II, a coordination change that leads from a bidentate interaction mode to a monodentate one is indispensable in order to break the

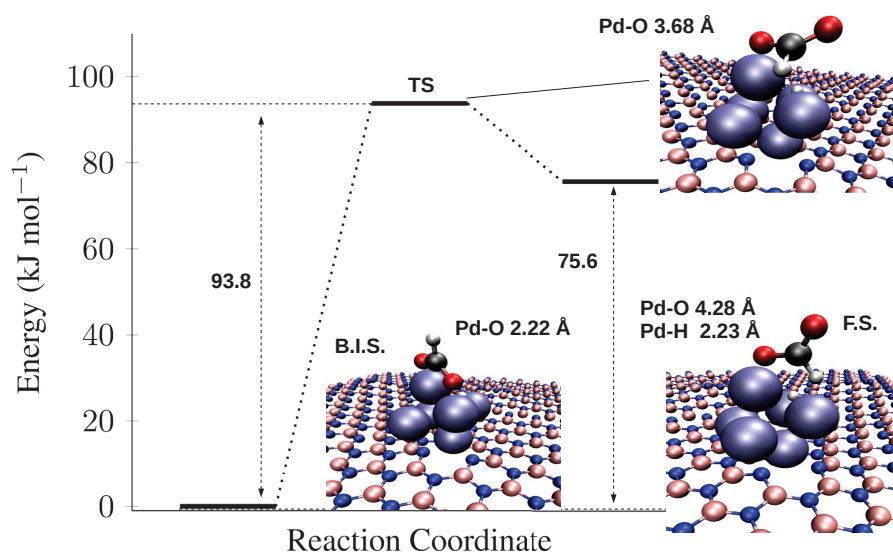


Figure 3.25 – Reaction coordinate for the HCOO coordination change on the top face of the supported Pd₆ cluster. The optimized structures of B.I.S., TS and F.S. are reported in the insets, with relevant geometrical descriptors.

3.3. Part III - Reactivity of formic acid on a defective *h*-BN supported Pd₆ catalyst

remaining C-H bond, as displayed in Figure 3.25; this step requires 93.8 kJ mol^{-1} and it is endoergic (75.6 kJ mol^{-1}), due to the breaking of a Pd-O bond. The correct orientation of hydrogen with respect the Pd catalyst, being the Pd-H bond distance 2.23 \AA , allows the last C-H bond breaking. This C-H bond cleavage is really easy, requiring only 14.9 kJ mol^{-1} and producing CO_2 , almost desorbed from the Pd sub-nanoparticle, and a Pd interacting hydrogen atom. This latter molecular step is exoergic, being the final state 90.7 kJ mol^{-1} more stable than the reference state. The optimized structures as well the energetic features of this step are reported in Figure 3.26.

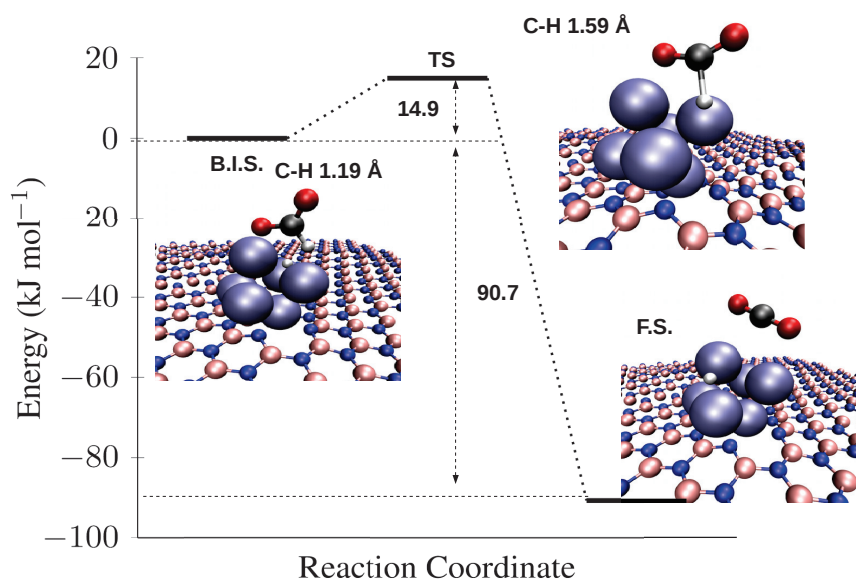


Figure 3.26 – Reaction coordinate for the $\text{HCOO} \rightarrow \text{CO}_2 + \text{H}$ step; the optimized structures of the B.I.S., TS and F.S. are reported in the insets, with relevant geometrical descriptors.

Top Face - Carboxyl Pathway

The parallelly adsorbed FA may evolve into COOH through a C-H bond breaking requiring 26.8 kJ mol^{-1} (see Figure 3.27); similarly to what reported in the Part II of this chapter, the carboxyla shows an atop coordination on a Pd atom, with a Pd-C bond distance of 2.13 \AA ; the hydrogen that has been lost in the last bond cleavage event is coordinated to the same Pd atom with a Pd-H bond length of 1.59 \AA ; this final state, that is 14.7 kJ mol^{-1} more stable than $\text{HCOOH}_{(flat)}$, is further stabilized by 49.5 kJ mol^{-1} due to the diffusion of H to a three-fold site of the cluster.

The final dehydrogenation step, implying an O-H bond breaking, requires $112.0 \text{ kJ mol}^{-1}$ and leads to the formation of CO_2 that, as previously mentioned (see Part II), assumes a peculiar v-shaped geometry. The process is exoergic, being this last structure 33.1 kJ mol^{-1} more stable

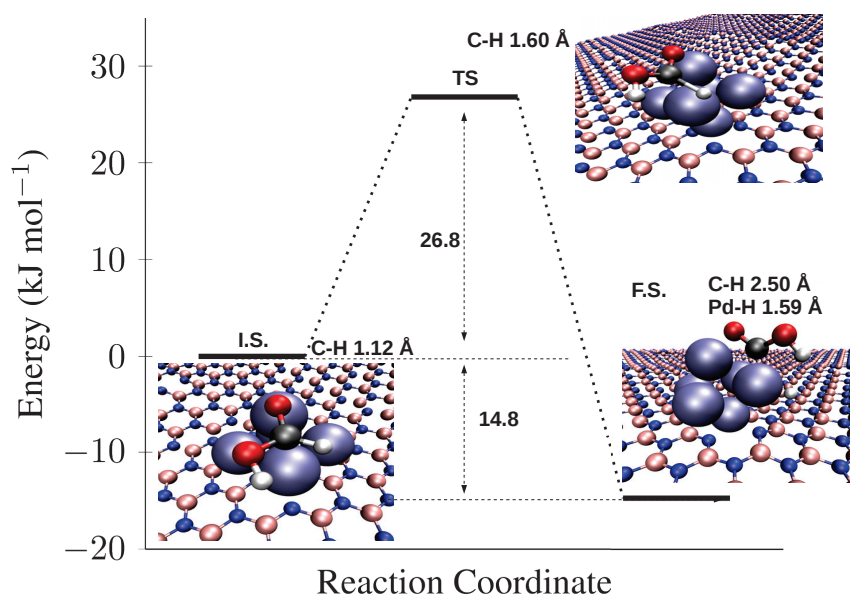


Figure 3.27 – Reaction coordinate for the $\text{HCOOH} \rightarrow \text{COOH} + \text{H}$ step on the top face of the supported Pd₆ cluster. The optimized structures I.S., TS and F.S. are reported in the insets, with relevant geometrical descriptors.

3.3. Part III - Reactivity of formic acid on a defective *h*-BN supported Pd₆ catalyst

than the initial carboxyl intermediate. It is interesting to notice how the introduction of a boron vacancy may affect the catalyst reactivity: indeed, the activation barrier for the O-H bond breaking enormously increases with respect to the defect-free system. This can have two different implications in the reaction mechanism: i) the final dehydrogenation step, through the carboxyl pathway, may be inhibited due to the prohibitively high activation barrier; ii) the process could occur in any case, exploiting possible alternative kinetic pathways in which this step has a more affordable energetic requirement.

In effect, according to Hakkinen and co-workers [65], a variety of effects could have a non negligible influence in the case of sub-nanometric clusters and among these cluster reconstructions or relaxations (*i.e.* fluxionality) may change the energetic landscape of a catalyzed process. In the case of Pd₆, when COOH is formed, the cluster could be subjected to a relaxation process which leads to a structure 10.7 kJ mol⁻¹ more stable than the initial nearly octahedral one. Interestingly, when the cluster shows this distorted structure, the carboxyl O-H bond breaking is facilitated, requiring 54.0 kJ mol⁻¹; the final state is 42.4 kJ mol⁻¹ stabilized and shows the formed CO₂ in the v-shaped geometry, atop coordinated with a Pd atom, as shown in Figure 3.28.

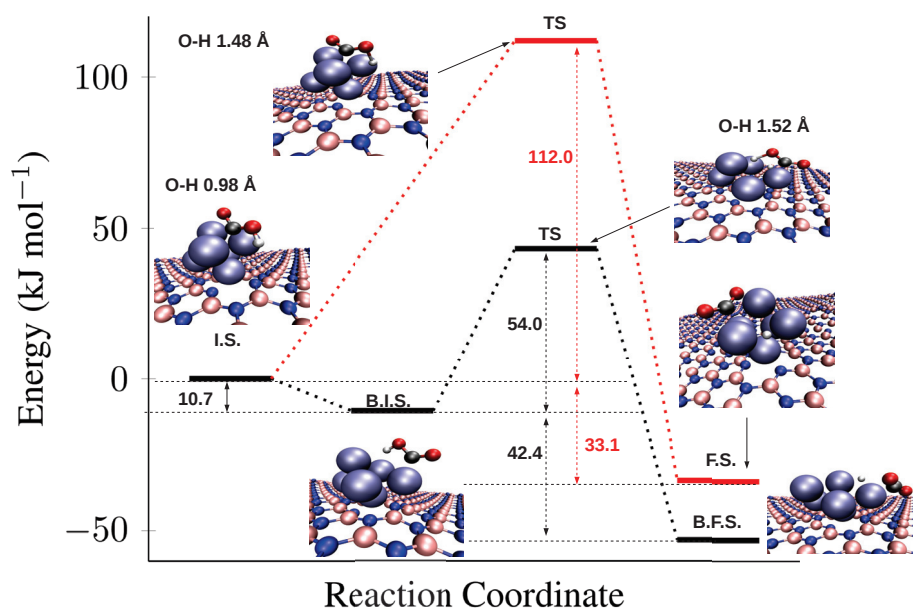


Figure 3.28 – Reaction coordinate for the COOH + H → CO₂ + 2H step on the top face of the supported Pd₆ cluster. The optimized structures of B.I.S., TS and (B.)F.S. are reported in the insets, with relevant geometrical descriptors. Black lines are used for the step in which the reconstruction of the cluster occurs; red lines are used for the unreconstructed, nearly octahedral, Pd₆ case.

Perimetral sites reactivity

The perimetral sites reactivity was investigated to unveil the role of reaction sites closer to the boron vacancy; in particular, differently from what seen in Part II for the perfect *h*-BN sheet, the presence of a defect may suggest the possibility that the unsaturated N atoms directly could take part to the reaction. Indeed, for the *h*-BN supported Pd₆ it was concluded that the influence of these specific sites, although present, was not pronounced and in any case limited to electronic effects.

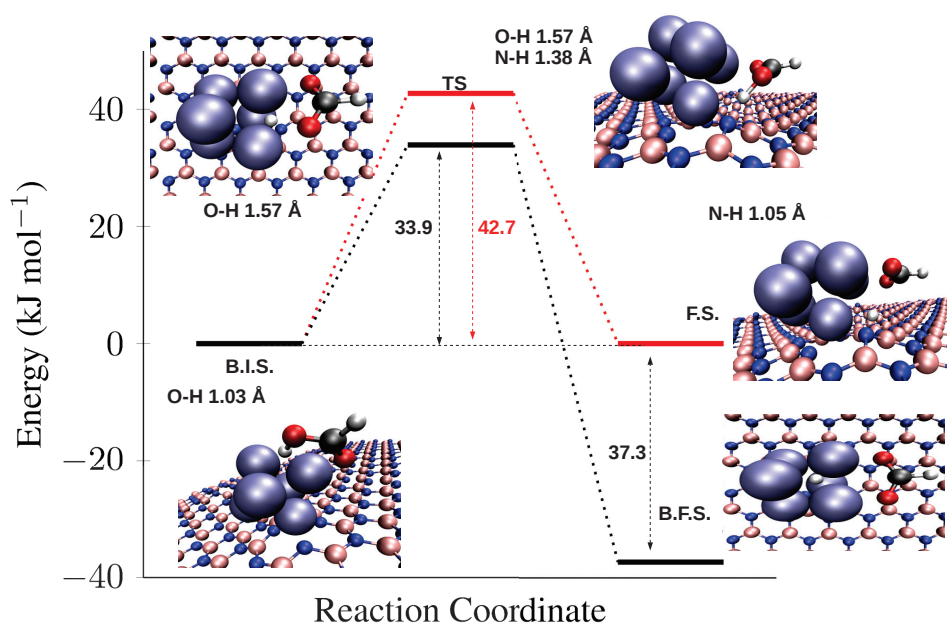


Figure 3.29 – Reaction coordinate for the $\text{HCOOH} \rightarrow \text{HCOO} + \text{H}$ (black) and $\text{HCOO} \rightarrow \text{HCOO} + \text{H}_{\text{BN}}$ (red) steps on the lateral face of the supported Pd₆ cluster. The optimized structures of B.I.S., TS and (B.)F.S. are reported in the insets, with relevant geometrical descriptors.

In particular, in the here reported case the possible presence of non-metal assisted decomposition pathways was investigated. As an example, from the perpendicular adsorption mode, HCOOH^* could decompose through an initial O-H bond breaking step, by direct hydrogen cession to one of the unsaturated N atoms. This process, whose PEC, optimized reaction intermediates and TSs are reported in Figure 3.29, was demonstrated to require 42.7 kJ mol^{-1} ; the final state, in which a hydrogen atom is bound to a nitrogen one with a bond length of 1.05 \AA , is almost isoenergetic with the adsorbed FA. By the way, this means that a great part of the energetic stabilization is due to the interaction of hydrogen with the palladium cluster. The palladium-mediated decomposition instead has an activation barrier for the first O-H bond cleavage of 33.9 kJ mol^{-1} . The lost hydrogen adsorbs on the top face of the cluster, with the usual three-fold coordination; the process is exoergic, releasing 37.3 kJ mol^{-1} . Thus, the

3.3. Part III - Reactivity of formic acid on a defective *h*-BN supported Pd₆ catalyst

most significant difference of the defect or metal-mediated decomposition pathway is the thermodynamic stability of the produced reaction intermediate, while the activation barriers are quite similar, being their difference only 8.7 kJ mol⁻¹.

On the grounds of its slightly higher feasibility and thermodynamic stability only the Pd-mediated mechanism for the prosecution of the HCOO decomposition path was further analyzed. The reaction mechanism has no evident differences with that on the top face of cluster, except from the energy required for the bidentate to monodentate interaction mode conversion. On the lateral side of the cluster this step has an activation barrier of 87.1 kJ mol⁻¹ and the monodentate HCOO is 60.9 kJ mol⁻¹ higher in energy than the bidentate coordination mode. The final dehydrogenation step, leading to CO₂, has a activation barrier of 33.1 kJ mol⁻¹.

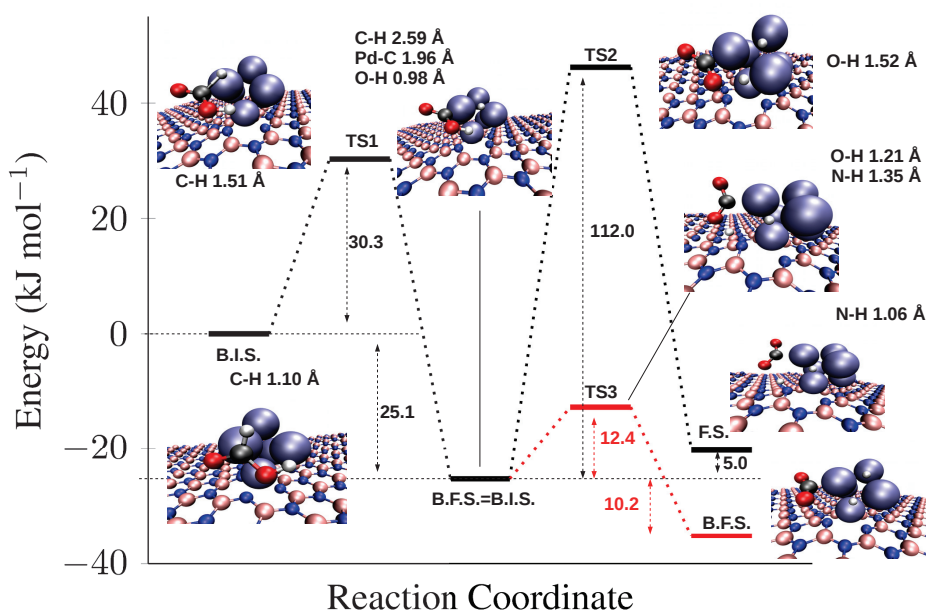


Figure 3.30 – Reaction coordinate for the HCOOH → CO₂ + 2H process, through the formation of COOH, on the lateral face of the cluster. Black lines were used for the metal mediated pathway, red lines for the support mediated one. The optimized structures of B.I.S., TS and (B.)F.S. are reported in the insets, with relevant geometrical descriptors.

Due to the geometrical features of the adsorbed FA on the lateral side, the vacancy-mediated dehydrogenation is not feasible: the adsorbed FA is not correctly orientated to interact directly with the support, as shown in Figure 3.30; instead, the Pd-mediated dehydrogenation has an activation barrier of 30.3 kJ mol⁻¹. This molecular step is exoergic, being the final state 25.1 kJ mol⁻¹ more stable than the FA. Differently from the first step, the formed COOH shows an interaction mode suited for both a Pd or support-mediated dehydrogenation. It is interesting to notice the very low activation barrier for the vacancy-mediated O-H bond cleavage, being

12.4 kJ mol⁻¹; these results, compared with the much higher energy requirement for the Pd₆-mediated dehydrogenation (71.3 kJ mol⁻¹) suggest that the support is far to be unreactive, but may have a direct role in the decomposition mechanism. The entire reaction path with associated intermediates and transition states optimized structures is displayed in Figure 3.30.

Discussion

Competition between HCOO and COOH pathways

The PEC for the HCOOH decomposition on the top face, through the two selected pathways is presented in Figure 3.31. At a glance, there are no evident differences from the PEC here presented and that relative to the defect-free system, shown in the Part II of this chapter. On the COOH pathway instead, the major point of difference between the defect-free system and the *h*-B_VN supported catalyst is the alternative kinetic path offered by the cluster reconstruction.

As previously reported in the literature [35] and along this chapter, the degree of stabilization of HCOO and COOH reaction intermediates may be a key factor for controlling the catalyst selectivity; indeed, the carboxyl has been recognized as the precursor for CO formation. Interestingly, within the introduction of a boron vacancy, the energy difference between HCOO and COOH seems to flatten; the effect is even more evident if we take into account, on the carboxyl pathway, the distorted structure of the cluster. In this case, the adsorbed formate and carboxyl are nearly isoenergetic with a difference of only 5.8 kJ mol⁻¹. Recalling one of the concept introduced in Part II, where the HCOO-COOH stabilization was correlated with the presence of the undercoordinated sites, we could say that on the *h*-B_VN the influence of low-coordinated sites is attenuated, probably due to the strong interaction of the cluster with the support. In other words, the energetic landscape seems to be more similar to that previously investigated for plane surfaces [111]. To this extent, Fampiou and Ramasubramaniam [119], in the case of defective graphene supported Pt₁₃ clusters, evidenced the weaker interaction of CO with the metal in comparison with unsupported cluster. The effect was attributed to the downshift of the d-band center of the cluster due to the strong interaction with the support, that would explain also our findings.

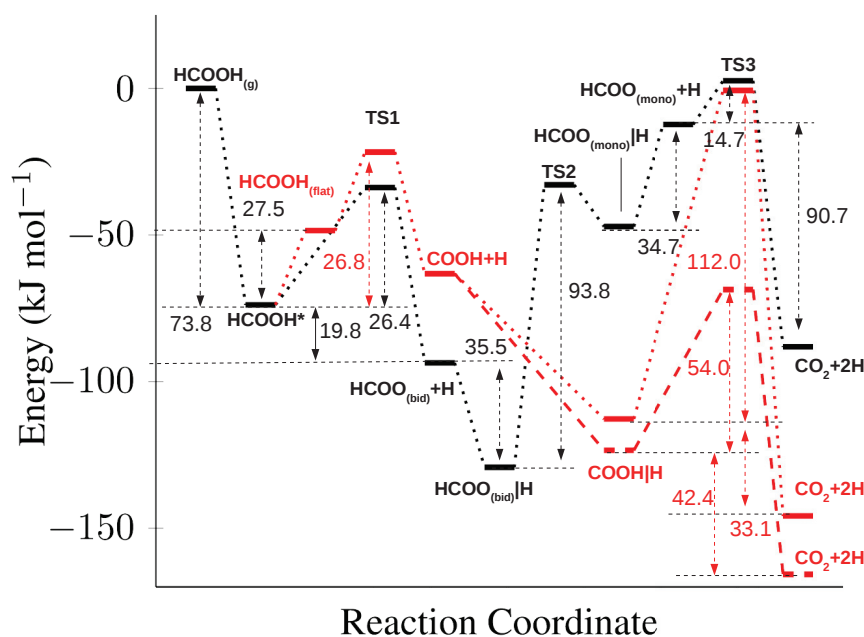


Figure 3.31 – Potential energy curve for the HCOOH decomposition, through the HCOO (black lines) and carboxyl (red lines) pathways, on the top face of the *h*-BN supported Pd₆ cluster; the dashed red line is associated to the COOH dehydrogenation on the distorted cluster; the vertical bar notation (A|B) indicates the most stable configuration of A and B coadsorbed on the cluster.

On the whole, due to the slightly higher energy requirement for the first C-H bond breaking associated on the COOH pathway, it is probable that the reaction flux could pass through the production of formate, as previously seen. However, it has to be noticed that the activation barrier required for the successive formate bidentate to monodentate conversion ($\text{HCOO}_{(bid)} \rightarrow \text{HCOO}_{(mono)}$) is much higher than that requested for the final dehydrogenation step of the COOH (considering the reconstruction). This fact, along with the contained energetic difference found for the HCOO and COOH intermediates, may suggest that a contribution of the carboxyl pathway to the overall reaction can not be completely excluded.

On the perimetral sites of the cluster the energetic landscape of the decomposition reaction is more complex, because also the vacancy-mediated O-H bond breakings have to be considered. The PEC of the HCOO and COOH pathways is reported in Figure 3.32. The formation of HCOO should be easier than the initial C-H bond breaking leading to COOH, due to the favourable thermodynamics and kinetics. The activation barrier for the vacancy-mediated decomposition is slightly higher than that required for the Pd-mediated mechanism; the higher stability of formate and hydrogen when adsorbed on the metal cluster with respect to the case in which hydrogen interacts with the support corroborates the hypothesis of a Pd-mediated

Hydrogen availability

At variance with the results shown for a perfect *h*-BN support, the reaction mechanism above discussed suggests that an interaction between hydrogen and the boron vacancy could take place. This may have important consequences for the development of strategies for simultaneous production and storage of hydrogen, starting from biomass molecules. Hence, it is interesting to deepen the fate of the produced hydrogen and its potential availability. In particular, apart from the direct hydrogen cession from formate or carboxyl, two other mechanisms were investigated: the spillover from the cluster to the support and the desorption of H₂.

For the *h*-BN supported Pd₆ cluster studied in Part II, the metal to support spillover was demonstrated to be unfeasible, in agreement with the literature treating similar systems [120]. In the here reported case, hydrogen diffusion was modeled considering a multi-step process involving first, the diffusion of hydrogen from the top face to the support-interacting face of the cluster, then the diffusion to the boron vacancy. Due to the high stability of the formate, hydrogen diffusion was studied in the presence of a co-adsorbed HCOO molecule, that, as we demonstrated in the Part II, may affect the hydrogen migration kinetics. The PEC and optimized structures relative to the hydrogen spillover mechanism are presented in Figure 3.33A. The first diffusion step has an activation barrier of 16.2 kJ mol⁻¹. Instead, the final migration has a much higher energy requirement of 83.5 kJ mol⁻¹; moreover, hydrogen is considerably less stable when adsorbed on the support than when it interacts with the cluster. Therefore, despite the introduction of a boron vacancy makes possible the diffusion to the support – contrary to the findings valid for a defect-free *h*-BN sheet – the process is still difficult. In other words, at this specific low coverage, hydrogen does prefer to interact with the metal.

Finally, hydrogen could simply desorb, as H₂, from Pd₆. This process has been previously studied by Granja *et al.* on a graphene supported Pd₆ cluster for which they calculated a H₂ desorption energy of 71.4 kJ mol⁻¹ [113].

When two hydrogen atoms produced from HCOOH interact with two different three-fold sites of the cluster, the following steps, in agreement with the above reported study, can be recognized for the recombinative desorption: i) hydrogen diffusion to an atop and an edge cluster site; ii) recombinative step iii) desorption. The optimized structures associated to these molecular events and their relative energy are reported in Figure 3.33B; taking as reference state that in which both hydrogens have a three-fold coordination, the diffusion toward the edge and atop sites is exoergic, being the final state 34.3 kJ mol⁻¹ less stable than the reference. The recombinative step has an activation barrier of 14.8 kJ mol⁻¹ and leads to a structure in which H₂ adsorbs with a η^2 coordination mode to a Pd atom, as already found in the literature for similar sub-nanometric clusters [112, 113]. However, this adsorption mode is still less stable than the reference state. At the end, a desorption energy of 67.0 kJ mol⁻¹ was calculated, in close agreement with previous studies performed on graphene supported palladium clusters [113].

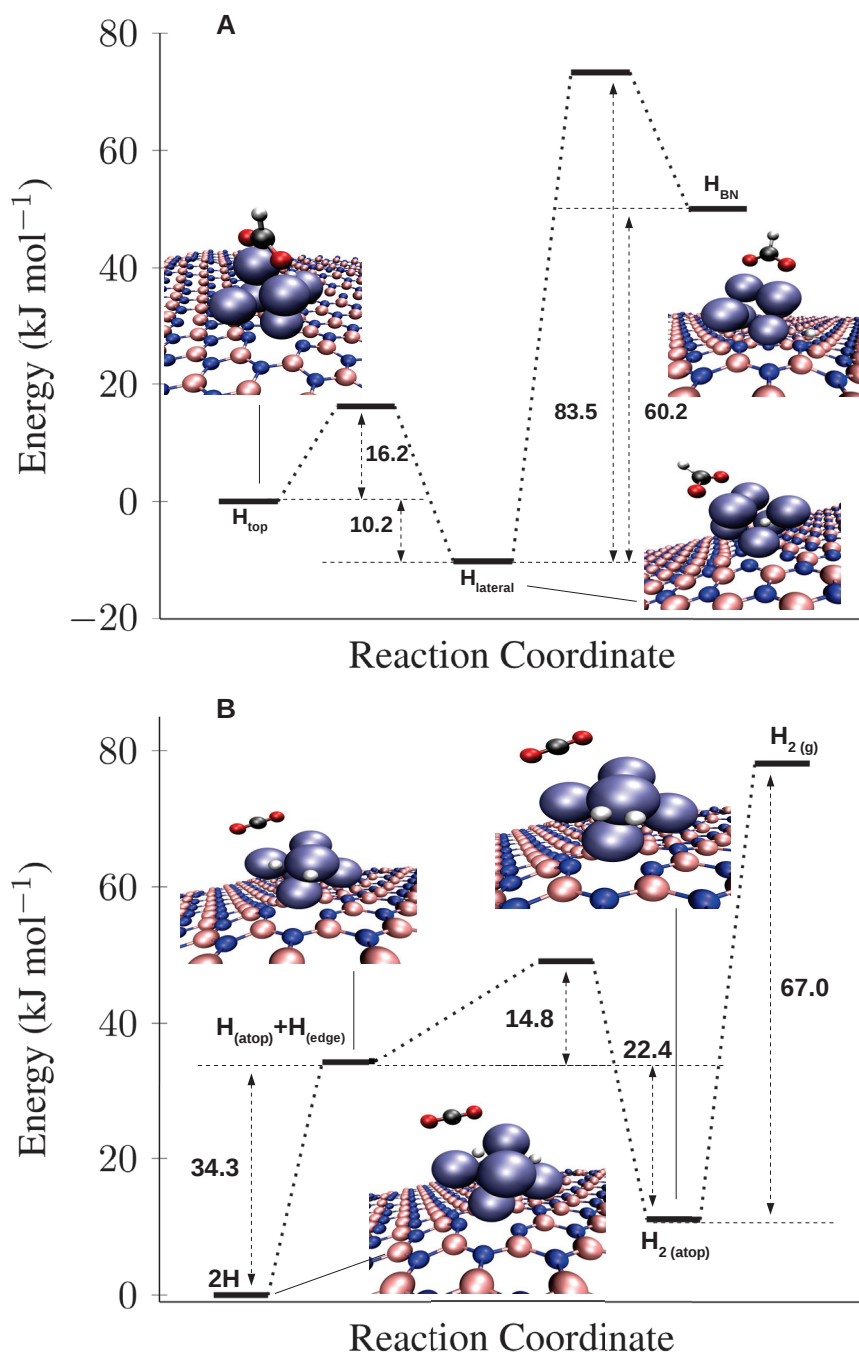


Figure 3.33 – Reaction coordinate for the hydrogen spillover (A) and desorption mechanism (B).

Conclusions

An extensive study on a boron nitride supported sub-nanometric Pd catalyst for formic acid decomposition was carried out by means of DFT calculations. The catalytic system was investigated taking into account different aspects ranging from the growth of a sub-nanometric Pd cluster on a BN support, performed through a QM/MM approach, to catalytic studies, performed with a periodic DFT method.

The interactions of sub-nanosized Pd clusters with a BNNT support were investigated, focusing both on the structural and energetic properties of the resulting systems. Different geometries and spin state multiplicities were evaluated. In some cases, namely Pd₂ and Pd₈, it was found that the interactions between the metal cluster and the BNNT support led to an inversion of the ground state multiplicity of the considered cluster. While in Pd₃/BNNT the triplet-singlet energy difference is reduced with respect to that calculated for the cluster *in vacuo*, in all other cases the whole Pd_n/BNNT system has the same multiplicity of the corresponding isolated Pd_n and shows large energy gaps with the other spin states. The growth of the Pd_n clusters would seem to be ruled by a templating effect of the BNNT B₃N₃ rings. In fact, starting from the Pd₄ cluster, the wide majority of the supported species showed triangular faces that effectively interact with the BNNT surface. For the same reason larger clusters showed stacked geometries with exposed (111)-like surfaces, thus suggesting the possibility to exploit BNNT supports as templating scaffolds.

Starting from these evidences, a *h*-BN supported Pd₆ sub-nanometric cluster was studied and proposed as a suitable system for fast and selective formic acid to hydrogen conversion. In particular, the competition between two dehydrogenation paths, namely formate and carboxyl was investigated. DFT calculations suggest that FA should decompose through the formate reaction pathway, due to the high stabilization of the HCOO reaction intermediate. However, even through the COOH pathway, the dehydrogenation process should be preferred to the decarbonylation, being the activation barrier for this latter process approximately 30 kJ mol⁻¹ higher in energy. The activation barriers calculated for the dehydrogenation steps are generally lower than those found previously on Pd surfaces. The highest activation barrier found, of approximately 108 kJ mol⁻¹, is associated to the conversion from bidentate to monodentate formate, presumably the rate determining step. Both this high energy requirement as well as the stabilization of most of the reaction intermediates were ascribed to the high level of undercoordination of the Pd atoms in the cluster. The lower activation barrier required for the same rearrangement on the lateral face of the cluster (hence interacting with the support) and the comparison with state of art DFT studies on periodic surfaces, substantiate this conclusion. In this sense the role of site coordination for tuning the stability of HCOO or COOH surface intermediates has to be stressed.

The influence of support defectivity was addressed, introducing a B vacancy in the *h*-BN support. In this case we demonstrated that the energetic landscape of formic acid decomposition is influenced by the cluster fluxionality. The introduction of a boron vacancy, probably due to the strong cluster-support interaction causes generally an increase of the activation energy

Chapter 3. Computational Design of a Boron Nitride Supported Pd Catalyst

required for the initial dehydrogenation step with respect the defect-free system. Moreover we demonstrated that on the perimetral sites of the cluster, some reaction paths may involve the direct participation of the vancancy on the dehydrogenation process.

Finally, hydrogen spillover mechanism was studied, in order to understand the energetics involved in the H diffusion on Pd₆ or on the support. We concluded that, at this early stage of the reaction, the migration toward the support is energetically unfavoured; however the introduction of a B vacancy lowers the activation barrier for the diffusion, that in any case would require *ca.* 80 kJ mol⁻¹.

4 Concluding remarks

A computational investigation, mainly based on DFT approaches, was carried out to deepen different aspects of Pt and Pd catalyzed hydrogen production methods, starting from biomass derived molecules, such as 1,2-PDO and FA.

1,2-PDO decomposition was studied on a model Pt catalyst, a Pt₃₀ cluster showing both (111) and (100) plane surfaces. In both cases the formation of HA was demonstrated to be highly favoured; the decomposition mechanism involve successive dehydrogenation steps while the C-C bond breaking should become competitive only once highly dehydrogenated compounds are formed. This general trend is common both to the modeled Pt(111) and Pt(100) surfaces and thus, at least in terms of competition towards different bond cleavages, the process seems to be structure insensitive. However, the activation barriers found for the dehydrogenation, especially for the initial ones, seem to be slightly lower on the Pt(100), a possible clue of its higher activity.

Parallely, a catalytic system consisting in a *h*-BN supported sub-nanometric Pd₆ cluster was entirely modeled by means of DFT methods and its catalytic properties predicted. In particular the growth pattern of sub-nanometric Pd clusters, ranging from Pd₂ to Pd₈ onto a BNNT support was investigated and the use of a grown Pd₆ cluster as model catalyst for FA dehydrogenation was addressed. The growth mechanism, discussed in its structural and energetic features, seems to lead to the formation of stacked geometries with exposed (111)-like surfaces, due to the symmetry matching between cluster and BN support. Since we demonstrated that the sub-nanoparticle growth mechanism should be insensitive to the BNNT curvature a *h*-BN nanosheet was used in the reactivity study as model support for the selected Pd₆ cluster. The catalytic system showed really promising properties for the selective production of hydrogen from FA. A variety of aspects were taken into account in order to pinpoint the key factors governing the reactivity of the catalyst. As an example the presence of highly undercoordinated sites was suggested to be at the basis of the preferential FA decomposition through the formate pathway and of the lower activation barrier found for the dehydrogenation, with respect to a Pd(111) surface. The effect exerted by the boron nitride support was considered by studying the decomposition mechanism at the cluster-support interface, even in presence of a boron

Chapter 4. Concluding remarks

vacancy. It was concluded that the introduction of a defect in the support slightly increases the activation barriers required for the decomposition and makes the hydrogen spillover easier. However, several effects could contribute to the overall reaction mechanism such as cluster fluxionality and nitrogen mediated decomposition steps. These latter have, for some selected cases, even lower activation barriers than the metal-mediated decomposition. The C-O bond breaking, leading to CO, was demonstrated to be generally less favoured with respect the C-H and O-H ones; this clearly suggests new strategies toward the CO free production of hydrogen from renewable FA feedstocks.

The here presented studies open several scenarios for future developments. As an example the study concerning the 1,2-PDO decomposition mechanism is at the basis of an ongoing collaboration with the Laboratory of Industrial Chemistry and Reaction Engineering of the Åbo Akademi University (AAU) of Turku (FI). The combined approach would guarantee both the rationalization of decomposition reaction networks involving biomass based feeds and provide hints for specific reaction by-products identification. Finally, the study of BN supported sub-nanometric cluster, here addressed with a predictive purpose, can be exploited to direct the synthesis of highly active and selective new generation catalysts.

A Density Functional Theory Formalism

In this appendix some of the key concepts of the Density Functional Theory (DFT) will be briefly illustrated. For this aim, it is assumed that the reader has already acquired the knowledge and use of some mathematical and physical objects such as the wavefunction, quantum-mechanical operators, their expectation values and the Schrodinger's equation, as introduced in the four postulates of quantum mechanics.

With this premise, it won't be difficult to found in the following equation the expression of the Hamiltonian operator for a system of N electrons and M nuclei:

$$\mathcal{H} = -\frac{1}{2} \sum_{i=1}^N \nabla_i^2 - \frac{1}{2} \sum_{A=1}^M \nabla_A^2 - \sum_{i=1}^N \sum_{A=1}^M \frac{Z_A}{r_{iA}} + \sum_{i=1}^N \sum_{j>1}^N \frac{1}{r_{ij}} + \sum_{A=1}^M \sum_{B>1}^M \frac{Z_A Z_B}{R_{AB}} \quad (\text{A.1})$$

The first three terms of the equation are respectively the kinetic energy associated to the *i*-th electron, that referred to the *A*-th nucleus and the potential energy associated to the coulombic attraction between the *i*-th electron and *A*-th nucleus. Since the presence of an attractive potential between electrons and nuclei can be imagined as a particular occurrence of the more general case in which the electrons feel the effect of an external potential v_{ext} , it is useful to rewrite the A.1 in a more compact and generalized way as:

$$\mathcal{H} = \hat{T}_e + \hat{T}_N - \hat{v}_{ext} + \hat{U}_{ee} + \hat{U}_{Ne} \quad (\text{A.2})$$

It could be noticed that, since the third term in both Equations A.1 and A.2 depends simultaneously on nuclear and electronic coordinates, it is not possible to decouple the two variables. However, according the Born-Oppenheimer approximation, the difference between electronic and nuclear masses is so high that it is possible to infer that electrons respond instantaneously to any variation in the nuclear coordinates; this implies that once these latter have been fixed,

Appendix A. Density Functional Theory Formalism

the electronic contribution to the Hamiltonian can be rewritten as:

$$\mathcal{H}_{el} = -\frac{1}{2} \sum_{i=1}^N \nabla_i^2 - \sum_{i=1}^N \sum_{A=1}^M \frac{Z_A}{r_{iA}} + \sum_{i=1}^N \sum_{j>1}^N \frac{1}{r_{ij}} = \hat{T}_e - \hat{v}_{ext} + \hat{U}_{ee} \quad (\text{A.3})$$

Thus the electronic wavefunction, and its associated energy, will depend parametrically on the nuclear coordinates. It has to be stressed that both the electronic and complete Hamiltonian defined respectively by Equations A.2 and A.3 can be univocally expressed knowing the total number of electrons and nuclei as well as the nuclear position and charges.

From the wavefunction to the electron density: initial developments

The first postulate of quantum mechanics asserts that the wavefunction, ψ , function of $3N$ spatial coordinates and N spin variables, completely describes the state of a quantum-mechanical system, or, in other words, contains all the information concerning a molecular system. Anyway, there is nothing that prevents from looking for another quantity that, despite containing all the wavefunction information, could be easier to treat from a mathematical and physical point of view and possibly closer to the interests of a chemist or material scientist. The electronic density, $\rho(r)$, of a specified system shows some interesting properties that make it especially suited to this aim. Indeed, if integrated over all the space it is possible to obtain the total number (N) of electrons according to the following equation:

$$N = \int \rho(r) dr \quad (\text{A.4})$$

Moreover, the function $\rho(r)$ shows maxima, cusps points actually, on the nuclear positions and it is correlated to the nuclear charge as shown by Equation A.5

$$\left. \frac{\partial \bar{\rho}(r_A)}{\partial r_A} \right|_{r_A=0} = -2Z_A \rho(r_A) \quad (\text{A.5})$$

where $\bar{\rho}(r_A)$ is the spherically averaged electronic density. According to these premises, it is not surprising how Thomas and Fermi, in 1927, hypothesized that the energy of a system could be expressed as a unique function of the electronic density and this, well before than Hohenberg and Kohn, in 1964, gave a rigorous mathematical treatment to this assertion.

The Thomas-Fermi theory was based on a really simple assumption: each contribution E_a to the total energy of an electronic system, so intrinsically inhomogeneous, can be estimated

using approximations already well known for the homogeneous electron gas and calculating locally its value corresponding to a given electron density; this approximation, called "local density" (LDA) can be expressed according the following equation:

$$E_a[\rho(r)] = \int \rho(r) \varepsilon_a[\rho(r)] dr \quad (\text{A.6})$$

where $\varepsilon_a[\rho(r)]$ represents a energy density associated to a given a contribution. As already said E_a is a unique function of $\rho(r)$ that as well depends on spatial coordinates. A function that has as argument another function is called *functional*, and their dependency, called "functional dependence" is labeled using the square parentheses [].

As an example starting from the kinetic energy density of the uniform electron gas, expressed by $t[\rho] = C_\kappa \rho^{2/3}$, with $C_\kappa = 3/10(3\pi^2)^{2/3}$ Hartree, it is possible to calculate, through Equation A.6, the kinetic contribution to the total energy, obtaining the kinetic energy functional:

$$T[\rho] = C_\kappa \int \rho(r)^{5/3} dr \quad (\text{A.7})$$

Adding this one to the more intuitive classic contributions to the electron-electron and nucleus-electron interaction the Equation A.8 can be obtained

$$E[\rho] = C_\kappa \int \rho(r)^{5/3} dr + \frac{1}{2} \int \int \frac{\rho(r_1)\rho(r_2)}{r_{12}} dr_1 dr_2 + \int v_{ext}\rho(r) dr \quad (\text{A.8})$$

that is, according to the Thomas-Fermi model, the easiest expression defining the total energy using, as unique variable, the electronic density, in the LDA approximation, as displayed by Equation A.6.

Anyway this approximation, makes Equation A.8 unusable for practical purposes, that is to say for the production of results with "chemical accuracy". In fact, electronic density of atoms and molecules cannot be defined as homogeneous, even if locally computed. As a consequence, the electronic densities obtained with this approach diverge at the nuclear position and their exponential decay with the distance from the nucleus is not very well reproduced; however, the approximation is, for other reasons, more suitable to treat condensed phases.

A huge limitation to the practical use of Equation A.6 is the total lack of energetic contributions arising from the electronic "correlation": electrons are indeed considered independent, not interacting and so not correlated in any way. In other words the interelectronic repulsion term in A.6 is calculated as if each electron (or their associated electronic density) felt the influence of other electrons only in an averaged way. Obviously this is a rather crude approximation,

Appendix A. Density Functional Theory Formalism

since, for a real system, the interaction among electrons is instead instantaneous. A particular type of correlation, the "exchange", rises from pure quantum-mechanical reasons: it can be demonstrated that the repulsive contribution felt by two electrons with symmetrical spin results attenuated if compared with that felt by electrons with anti-symmetrical spin; this energetic contribution, direct consequence of the Pauli exclusion principle, is called "exchange contribution" and it can be exactly estimated through wavefunction based approaches, such as the Hartree-Fock method.

Using the same local density approximation already introduced for the other energetic contributions, Slater derived the following expression for the exchange energy $E_x[\rho]$:

$$E_x[\rho] = -C_x \int \rho(r)^{4/3} dr \quad (\text{A.9})$$

with $C_x = 9/8\alpha(3/\pi)^{(1/3)}$ hartree and $\alpha = 1$; according to other derivations, different α values were considered, such the solution proposed by Bloch and Dirac with $\alpha = 2/3$. The model described, in which this approximated expression for the exchange energy is taken into account is generally recognized as Thomas-Fermi-Dirac model. Introducing in A.8 the Slater exchange functional and a generic correlation functional $E_c[\rho]$ the following equation can be obtained:

$$E[\rho] = C_\kappa \int \rho(r)^{5/3} dr + \frac{1}{2} \iint \frac{\rho(r_1)\rho(r_2)}{r_{12}} dr_1 dr_2 + \int v_{ext}\rho(r) dr - C_x \int \rho(r)^{4/3} dr + E_c[\rho] \quad (\text{A.10})$$

Despite most of the limits of Equation A.8 are still present with the introduction of these exchange and correlation terms, we wonder what could be a general prescription for using equation A.10, since, just as the wavefunction, we only know approximated estimation for its associated electronic density.

The Hohenberg-Kohn theorems

For the wavefunction, the variational principle says that the energy associated to each trial wavefunction ψ_{trial} , will be greater than or equal to the ground state energy of the system, associated to the real wavefunction ψ_0 . Thus, for variational methods, the resolution of the many-electron system is reduced to more or less efficient constrained minimizations, used for finding the wavefunction value associated to the lowest energy. Of course, the existence of an equivalent variational principle which correlates electronic densities and energy would allow the use of similar minimizations also in the case of Equation A.10, or more generally of all the relations in which a functional dependence of energy and electronic density is expressed.

As introduced before, Hohenberg and Kohn, in 1964, gave a more rigorous mathematical treatment to density functional theory, initiating what is usually designed as "modern" DFT. The activity of Hohenberg and Kohn, culminated with the formulation of two theorems, essential for the development of density functional theory [124]. The first theorem states that

the external potential $\hat{v}_{ext}(r)$ that affects a n -electrons interacting system is, with the exception of a constant, a unique functional of the electronic density associated to the ground state of the system.

This external potential, that in the case of a molecular system is given by the attractive nuclei-electrons potential, establishes in a unique way the electronic density of the system. In other words, with the first Hohenberg-Kohn theorem is possible to affirm, from pure mathematical basis, that the electronic density of a system in its ground state contains all information required for the system definition; as previously mentioned, the Hamiltonian of an electronic system can be described knowing few quantities, *i.e.* the number of electrons, nuclei and the nuclear positions. Or more simply, representing with \rightarrow an univocal relation, the following correspondence can be found:

$$\rho(r) \rightarrow \hat{v}_{ext}(r) \rightarrow \mathcal{H} \rightarrow \psi_0$$

and in agreement with the first theorem, the energy of the system in its ground state can be expressed as:

$$E_0[\rho] = \int v_{ext}\rho(r)dr + F_{HK}[\rho] = \int v_{ext}\rho(r)dr + T[\rho] + V_{ee}[\rho] \quad (\text{A.11})$$

where $F_{HK}[\rho]$ is the so called Hohenberg-Kohn universal functional, made up by the sum of the (exact) kinetic energy ($T[\rho]$) and electronic repulsion ($V_{ee}[\rho]$) functionals; an expression for $F_{HK}[\rho]$ is obviously unknown.

The second Hohenberg-Kohn theorem is basically a reformulation of the variational principle for the electronic densities, according to the following inequality:

$$F_{HKtrial}[\rho] + \int v_{ext}\rho_{trial}(r)dr \geq \int v_{ext}\rho(r)dr + F_{HK}[\rho] = E_0[\rho] \quad (\text{A.12})$$

This means that, just as wavefunction behave, each *trial* electronic density, *i.e.* approximation of the real electronic density of the system, will be associated to an energy value greater or equal than that relative to the ground state. Intuitively, as previously introduced, by the knowledge of the electronic density and energy functional dependence, solving the n -electronic problem

could be equivalent to searching for the $\rho(r)$ function minimizing the energy.

The Kohn-Sham SCF method

The two Hohenberg-Kohn theorems don't give any insight into how to practically solve the n -electronic problem. This was object of the work of Kohn and Sham that, in 1965, suggested a general strategy for the energy calculation in an inhomogeneous electronic system. It has to be mentioned that, at the beginning of the 1900s, a similar procedure was well known for the Hartree-Fock method, based on the wavefunction.

The main concern in the application of the Hamiltonian A.2 or, in terms of electronic density, of A.11 for the calculation of the polyelectronic system energy, is the estimation of the electron-electron repulsion contribution. The Kohn-Sham approach [125], is based on a straightforwardly simple assumption: it is possible to substitute the electronic density of a n -interacting electrons system, with an equivalent, fictitious, electronic density associated to non-interacting electrons. This assumption is corroborated by the existence of a unique relation between Hamiltonian and electronic density; thus, two systems having the same electronic density profiles share the same Hamiltonian. From a practical point of view instead, this is equivalent to consider the wavefunction of the system as the results of the anti-symmetrized product of monoelectronic wavefunctions ψ_i , called Kohn-Sham orbitals. Accordingly, the polyelectronic Hamiltonian could be expressed as sum of monoelectronic operators. Hence, the electronic density can be expressed as an expansion of monoelectronic functions:

$$\rho = \sum_{i=1}^N \psi_i^2 \quad (\text{A.13})$$

It is possible to extract from A.11 each classical contribution, valid for the non interacting system, to the repulsive electron-electron potential, $J[\rho]$, and to the kinetic energy functional $T[\rho]$, obtaining:

$$E_0[\rho] = \int v_{ext}\rho(r)dr + T_0[\rho] + J[\rho] + E_{xc}[\rho] \quad (\text{A.14})$$

where $J[\rho] = \frac{1}{2} \int \int \frac{\rho(r_1)\rho(r_2)}{r_{12}} dr_1 dr_2$ and $T_0[\rho] = -\frac{1}{2}\nabla^2$. It should be noticed that in A.14, all the terms associated to non classical contributions, were included in the expression $E_{xc}[\rho]$, called exchange-correlation functional. Moreover, it is important to remind that the same A.14 is in principle exact, since, in the discussion presented so far, it has not been introduced any approximation; however, since an exact expression for the exchange-correlation functional is not known, just as the Hohenberg-Kohn universal functional, all the approximations in A.14 will be introduced in order to estimate the $E_{xc}[\rho]$ contribution.

The variational minimization of A.14 with respect to the ψ_i Kohn-Sham orbitals, leads to the Kohn-Sham equations, expressed as:

$$-\frac{1}{2}\nabla_i^2\psi_i + v_{KS}\psi_i = \epsilon_i\psi_i \quad (\text{A.15})$$

with $v_{KS} = v_{ext} + \int \frac{\rho(r_j)}{r_{ij}} dr_j + V_{xc}(r_i)$. Since the term v_{KS} depends on the solutions of Equation A.15, the Kohn-Sham equations are solved through an iterative procedure, called Self Consistent Field (SCF).

Exchange-correlation functionals

The only part of Equation A.14 that remains formally undefined is the form of the exchange-correlation functional $E_{xc}[\rho]$, from which the exchange-correlation potential, V_{xc} , showed in Equation A.15, is derived. In fact, an exact form for $E_{xc}[\rho]$ is not known; in that case the DFT method would provide an exact solution to the many-electron problem and the energy of the system could be calculated exactly. Conversely, the choice of a suitable approximation for the exchange-correlation functional $E_{xc}[\rho]$ is still among the most important concerns of DFT.

A first approximated expression was already, implicitly, introduced along the text: the Local Density Approximation (LDA), as introduced in Equation A.6. In this case, the energy is expressed as the integral of a function of the solely electronic density; while the exchange contribution can be introduced using Equation A.9, analytical expression for the correlation contribution were historically derived by Vosko, Will and Nusair starting from accurate electronic gas simulations provided by Ceperly and Alder. Later, an approximation was proposed by Perdew and Wang. Obviously the LDA suffers of all the limitations already discussed along the text.

Better performances are provided by the functionals belonging to the Generalized Gradient Approximation (GGA) class in which the dependence on the electronic density gradient, $\nabla\rho(r)$ is introduced in the exchange-correlation functional. Usually, the exchange part is introduced as a correction to the corresponding LDA functional E_X^{LDA}

$$E_X^{GGA} = E_X^{LDA} - \sum_{\sigma} \int F(s_{\sigma})\rho_{\sigma}^{4/3} dr \quad (\text{A.16})$$

where s_{σ} is a function of the density gradient, *i.e.* the reduced density gradient per spin. A variety of expressions for F were proposed in the literature; the first, derived by Becke, was in

Appendix A. Density Functional Theory Formalism

the form:

$$F^{B88} = \frac{\beta s_{\sigma}^2}{1 + 6\beta s_{\sigma}^2 \sinh^{-1}(s_{\sigma})} \quad (\text{A.17})$$

with $\beta = 0.0042$. From this expression more recent functionals were derived such as the PW91 [126]. According to other methods, the function F is expressed as a rational function of the reduced density gradient. From this approach the Becke (B86), Perdew (P86) and Perdew, Burke, Ernzerhof (PBE) [103] functionals were obtained.

Taking into account higher order derivatives of the electronic density, such as $\nabla^2 \rho(r)$, leads to the so called meta-GGA functionals, such as the M06-L [71] extensively used along this dissertation.

Finally, among the most used exchange-correlation functionals the so called hybrid functionals have to be cited. In this class, GGA and LDA functionals are mixed with a fraction of exactly computed exchange term, that in principle could be calculated without approximations in the Hartree-Fock method. The reason underlying the choice of using only part of the exact exchange has to do with the correct physical description of exchange-correlation holes, whose dissertation goes beyond the aims of this appendix.

The Becke three parameters Lee-Yang-Parr functional (B3LYP) [127], developed with a proper combination of exact, GGA and LDA exchange and GGA and LDA correlation, is among the most used hybrid functional and can be expressed as:

$$E_{XC}^{B3LYP} = (1 - a)E_x^{LDA} + aE_{xc}^{\lambda=0} + bE_x^{B88} + cE_c^{LYP} + (1 - c)E_c^{LDA} \quad (\text{A.18})$$

with $a=0.20$, $b=0.72$ and $c=0.81$. In this expression E_x^{LDA} and E_x^{B88} are the exchange contributions calculated within the LDA and B88 methods, E_c^{LDA} and E_c^{LYP} the LDA and Lee-Yang-Parr correlation terms. $E_{xc}^{\lambda=0}$ is the exact exchange. Due to the success of this approach the number of hybrid functionals developed increased exponentially over the time. As an example, the PBE0 functional, proposed by Adamo and Barone [128], is built mixing the exact and PBE exchange term in a 1:3 ratio and provides good performance over a wide range of systems. In the more recent Minnesota class of functionals, the M06 and M06-2X show 27% and 54% of Hartree-Fock exchange, respectively [81].

Perdew has referred to the hierarchy of approximations developed during the last two decades as the "Jacob's ladder of DFT", where each functional category represents a different rung, toward the perfect description of a physico-chemical system and its properties. However, apart from the most crude approximations, it has to be said that finding the right exchange-correlation functional for the right application is usually much more difficult than selecting

among a category of more or less performing functionals. This concept, is even more valid in the case of computational catalysis. Indeed the chemical nature of the species treated at the same time, as well as the chemical and physical phenomena taking place, is extremely broad; as an example, the same exchange-correlation functional should be able to well describe a system containing metals, oxides and carbon-containing species, to provide accurate insights on adsorption processes as well as bond breaking steps and so on. Some general trends can be found: as an example, for a given average level of accuracy, hybrid and meta-GGA DFT methods are usually the most efficient, showing performances in terms of mean unsigned errors similar to much more expensive multilevel correlated methods. However, the maximum absolute errors are larger with the former than with the latter.

Bibliography

- [1] I. Dincer and C. Acar, "Review and evaluation of hydrogen production methods for better sustainability," *Int. J. Hydrogen Energ.*, vol. 40, no. 34, pp. 11 094 – 11 111, 2015.
- [2] C.-H. Zhou, X. Xia, C.-X. Lin, D.-S. Tong, and J. Beltramini, "Catalytic conversion of lignocellulosic biomass to fine chemicals and fuels," *Chem. Soc. Rev.*, vol. 40, no. 11, pp. 5588 – 5617, 2011.
- [3] D. Li, X. Li, and J. Gong, "Catalytic reforming of oxygenates: State of the art and future prospects," *Chem. Rev.*, vol. 116, pp. 11 529 – 11 653, 2016.
- [4] R. D. Cortright, R. R. Davda, and J. A. Dumesic, "Hydrogen from catalytic reforming of biomass-derived hydrocarbons in liquid water," *Nature*, vol. 418, no. 6901, pp. 964 – 967, 2002.
- [5] C. A. Schwengber, H. J. Alves, R. A. Schaffner, F. A. da Silva, R. Sequinel, V. R. Bach, and R. J. Ferracin, "Overview of glycerol reforming for hydrogen production," *Renew. Sust. Energ. Rev.*, vol. 58, pp. 259 – 266, 2016.
- [6] P. D. Vaidya and A. E. Rodrigues, "Glycerol reforming for hydrogen production: A review," *Chem. Eng. Tech.*, vol. 32, no. 10, pp. 1463 – 1469, 2009.
- [7] S. A. Tupy, J. G. Chen, and D. G. Vlachos, "Comparison of ethylene glycol steam reforming over pt and nipt catalysts on various supports," *Top. Catal.*, vol. 56, no. 18, pp. 1644 – 1650, 2013.
- [8] F. Pompeo, G. Santori, and N. N. Nichio, "Hydrogen and/or syngas from steam reforming of glycerol. study of platinum catalysts," *Int. J. Hydrogen Energ.*, vol. 35, no. 17, pp. 8912 – 8920, 2010.
- [9] J. W. Shabaker, G. W. Huber, and J. A. Dumesic, "Aqueous-phase reforming of oxygenated hydrocarbons over Sn-modified Ni catalysts," *J. Catal.*, vol. 222, no. 1, pp. 180 – 191, 2004.
- [10] A. Gallo, C. Pirovano, P. Ferrini, M. Marelli, R. Psaro, S. Santangelo, G. Faggio, and V. D. Santo, "Influence of reaction parameters on the activity of ruthenium based catalysts for glycerol steam reforming," *Appl. Catal. B: Environ.*, vol. 121, pp. 40 – 49, 2012.

Bibliography

- [11] T. Hirai, N.-o. Ikenaga, T. Miyake, and T. Suzuki, "Production of hydrogen by steam reforming of glycerin on ruthenium catalyst," *Energy Fuels*, vol. 19, no. 4, pp. 1761 – 1762, 2005.
- [12] S. Adhikari, S. Fernando, and A. Haryanto, "Production of hydrogen by steam reforming of glycerin over alumina-supported metal catalysts," *Catal. Today*, vol. 129, no. 3–4, pp. 355 – 364, 2007.
- [13] D. A. Simonetti, J. Rass-Hansen, E. L. Kunkes, R. R. Soares, and J. A. Dumesic, "Coupling of glycerol processing with fischer-tropsch synthesis for production of liquid fuels," *Green Chem.*, vol. 9, pp. 1073 – 1083, 2007.
- [14] R. Davda, J. Shabaker, G. Huber, R. Cortright, and J. Dumesic, "Aqueous-phase reforming of ethylene glycol on silica-supported metal catalysts," *Appl. Catal. B: Environ.*, vol. 43, no. 1, pp. 13 – 26, 2003.
- [15] L. I. Godina, A. V. Kirilin, A. V. Tokarev, and D. Yu. Murzin, "Aqueous phase reforming of industrially relevant sugar alcohols with different chiralities," *ACS Catal.*, vol. 5, no. 5, pp. 2989 – 3005, 2015.
- [16] M. Saliccioli, W. Yu, M. A. Barteau, J. G. Chen, and D. G. Vlachos, "Differentiation of O–H and C–H bond scission mechanisms of ethylene glycol on Pt and Ni/Pt using theory and isotopic labeling experiments," *J. Am. Chem. Soc.*, vol. 133, no. 20, pp. 7996 – 8004, 2011.
- [17] P. Ferrin, D. Simonetti, S. Kandoi, E. Kunkes, J. A. Dumesic, J. K. Nørskov, and M. Mavrikakis, "Modeling ethanol decomposition on transition metals: A combined application of scaling and Bronsted Evans Polanyi relations," *J. Am. Chem. Soc.*, vol. 131, no. 16, pp. 5809 – 5815, 2009.
- [18] G. Wen, Y. Xu, H. Ma, Z. Xu, and Z. Tian, "Production of hydrogen by aqueous-phase reforming of glycerol," *Int. J. Hydrogen Energ.*, vol. 33, no. 22, pp. 6657 – 6666, 2008.
- [19] Y. Guo, M. U. Azmat, X. Liu, Y. Wang, and G. Lu, "Effect of support's basic properties on hydrogen production in aqueous-phase reforming of glycerol and correlation between WGS and APR," *Appl. Energy*, vol. 92, pp. 218 – 223, 2012.
- [20] A. V. Kirilin, A. V. Tokarev, H. Manyar, C. Hardacre, T. Salmi, J.-P. Mikkola, and D. Yu. Murzin, "Aqueous phase reforming of xylitol over Pt-Re bimetallic catalyst: Effect of the re addition," *Catal. Today*, vol. 223, pp. 97 – 107, 2014.
- [21] X. Wang, N. Li, L. D. Pfefferle, and G. L. Haller, "Pt-co bimetallic catalyst supported on single walled carbon nanotube: XAS and aqueous phase reforming activity studies," *Catal. Today*, vol. 146, no. 1–2, pp. 160 – 165, 2009.
- [22] X. Wang, N. Li, Z. Zhang, C. Wang, L. D. Pfefferle, and G. L. Haller, "High-yield hydrogen production from aqueous phase reforming over single-walled carbon nanotube supported catalysts," *ACS Catal.*, vol. 2, no. 7, pp. 1480 – 1486, 2012.

- [23] G. W. Huber, J. W. Shabaker, and J. A. Dumesic, "Raney Ni-Sn catalyst for H₂ production from biomass-derived hydrocarbons," *Science*, vol. 300, no. 5628, pp. 2075 – 2077, 2003.
- [24] K. S. Kim, C. T. Kingston, A. Hrdina, M. B. Jakubinek, J. Guan, M. Plunkett, and B. Simard, "Hydrogen-catalyzed, pilot-scale production of small-diameter boron nitride nanotubes and their macroscopic assemblies," *ACS Nano*, vol. 8, no. 6, pp. 6211 – 6220, 2014.
- [25] M. Terrones, J. Romo-Herrera, E. Cruz-Silva, F. López-Urías, E. Muñoz-Sandoval, J. Velázquez-Salazar, H. Terrones, Y. Bando, and D. Golberg, "Pure and doped boron nitride nanotubes," *Mater. Today*, vol. 10, no. 5, pp. 30 – 38, 2007.
- [26] N. Meyer, D. Pirson, M. Devillers, and S. Hermans, "Particle size effects in selective oxidation of lactose with Pd/h-BN catalysts," *Appl. Catal. A*, vol. 467, pp. 463 – 473, 2013.
- [27] J. Q. Bond, D. M. Alonso, D. Wang, R. M. West, and J. A. Dumesic, "Integrated catalytic conversion of γ -Valerolactone to liquid alkenes for transportation fuels," *Science*, vol. 327, no. 5969, pp. 1110 – 1114, 2010.
- [28] A. Boddien, D. Mellmann, F. Gärtner, R. Jackstell, H. Junge, P. J. Dyson, G. Laurenczy, R. Ludwig, and M. Beller, "Efficient dehydrogenation of formic acid using an iron catalyst," *Science*, vol. 333, no. 6050, pp. 1733 – 1736, 2011.
- [29] J. J. A. Celaje, Z. Lu, E. A. Kedzie, N. J. Terrile, J. N. Lo, and T. J. Williams, "A prolific catalyst for dehydrogenation of neat formic acid," *Nat. Commun.*, vol. 7, p. 11308, 2016.
- [30] B. Loges, A. Boddien, H. Junge, and M. Beller, "Controlled generation of hydrogen from formic acid amine adducts at room temperature and application in H₂/O₂ fuel cells," *Angew. Chem. Int. Ed.*, vol. 47, no. 21, pp. 3962 – 3965, 2008.
- [31] F. Solymosi, A. Koos, N. Liliom, and I. Ugrai, "Production of CO-free H₂ from formic acid. A comparative study of the catalytic behavior of Pt metals on a carbon support," *J. Catal.*, vol. 279, no. 1, pp. 213 – 219, 2011.
- [32] K. Nishimura, K. Kunimatsu, K.-i. Machida, and M. Enyo, "Electrocatalysis of Pd + Au alloy electrodes," *J. Electroanal. Chem. Interfacial Electrochem.*, vol. 260, no. 1, pp. 181 – 192, 1989.
- [33] M. Arenz, V. Stamenkovic, T. J. Schmidt, K. Wandelt, P. N. Ross, and N. M. Markovic, "The electro-oxidation of formic acid on Pt-Pd single crystal bimetallic surfaces," *Phys. Chem. Chem. Phys.*, vol. 5, no. 19, pp. 4242 – 4251, 2003.
- [34] J.-Y. Wang, H.-X. Zhang, K. Jiang, and W.-B. Cai, "From HCOOH to CO at Pd Electrodes: A Surface-Enhanced Infrared Spectroscopy study," *J. Am. Chem. Soc.*, vol. 133, no. 38, pp. 14 876 – 14 879, 2011.
- [35] S.-I. Choi, J. A. Herron, J. Scaranto, H. Huang, Y. Wang, X. Xia, T. Lv, J. Park, H.-C. Peng, M. Mavrikakis, and Y. Xia, "A comprehensive study of formic acid oxidation on

Bibliography

- palladium nanocrystals with different types of facets and twin defects,” *ChemCatChem*, vol. 7, no. 14, pp. 2077 – 2084, 2015.
- [36] J. A. Herron, J. Scaranto, P. Ferrin, S. Li, and M. Mavrikakis, “Trends in formic acid decomposition on model transition metal surfaces: A density functional theory study,” *ACS Catal.*, vol. 4, no. 12, pp. 4434 – 4445, 2014.
- [37] J. B. Benziger and R. J. Madix, “The decomposition of formic acid on Ni(100),” *Surf. Sci.*, vol. 79, no. 2, pp. 394 – 412, 1979.
- [38] Y.-K. Sun and W. H. Weinberg, “Catalytic decomposition of formic acid on Ru(001): Transient measurements,” *J. Chem. Phys.*, vol. 94, no. 6, pp. 4587 – 4599, 1991.
- [39] S. W. Jorgensen and R. J. Madix, “Active oxygen on Group VIII metals: activation of formic acid and formaldehyde on Pd(100),” *J. Am. Chem. Soc.*, vol. 110, no. 2, pp. 397 – 400, 1988.
- [40] J. L. Davis and M. A. Barteau, “Reactions of carboxylic acids on the Pd(111)–(2 x 2) surface: multiple roles of surface oxygen atoms,” *Surf. Sci.*, vol. 256, no. 1, pp. 50 – 66, 1991.
- [41] J. B. Benziger and G. R. Schoofs, “Influence of adsorbate interactions on heterogeneous reaction kinetics. Formic acid decomposition on nickel,” *J. Phys. Chem.*, vol. 88, no. 19, pp. 4439 – 4444, 1984.
- [42] S. Vajda and M. G. White, “Catalysis applications of size-selected cluster deposition,” *ACS Catal.*, vol. 5, no. 12, pp. 7152 – 7176, 2015.
- [43] G. Kwon, G. A. Ferguson, C. J. Heard, E. C. Tyo, C. Yin, J. DeBartolo, S. Seifert, R. E. Winans, A. J. Kropf, J. Greeley, R. L. Johnston, L. A. Curtiss, M. J. Pellin, and S. Vajda, “Size-dependent subnanometer Pd cluster (Pd₄, Pd₆, and Pd₁₇) water oxidation electrocatalysis,” *ACS Nano*, vol. 7, no. 7, pp. 5808 – 5817, 2013.
- [44] J. S. Yoo, F. Abild-Pedersen, J. K. Nørskov, and F. Studt, “Theoretical analysis of transition-metal catalysts for formic acid decomposition,” *ACS Catal.*, vol. 4, no. 4, pp. 1226 – 1233, 2014.
- [45] Q.-Y. Bi, X.-L. Du, Y.-M. Liu, Y. Cao, H.-Y. He, and K.-N. Fan, “Efficient subnanometric gold-catalyzed hydrogen generation via formic acid decomposition under ambient conditions,” *J. Am. Chem. Soc.*, vol. 134, no. 21, pp. 8926 – 8933, 2012.
- [46] M. Saliccioli, M. Stamatakis, S. Caratzoulas, and D. Vlachos, “A review of multiscale modeling of metal-catalyzed reactions: Mechanism development for complexity and emergent behavior,” *Chem. Eng. Sci.*, vol. 66, no. 19, pp. 4319 – 4355, 2011.
- [47] M. Haruta, “Size- and support-dependency in the catalysis of gold,” *Catal. Today*, vol. 36, no. 1, pp. 153 – 166, 1997.

- [48] F. Abild-Pedersen, J. Greeley, F. Studt, J. Rossmeisl, T. R. Munter, P. G. Moses, E. Skúlason, T. Bligaard, and J. K. Nørskov, "Scaling properties of adsorption energies for hydrogen-containing molecules on transition-metal surfaces," *Phys. Rev. Lett.*, vol. 99, p. 016105, 2007.
- [49] J. N. Bronsted, "Acid and basic catalysis," *Chem. Rev.*, vol. 5, no. 3, pp. 231 – 338, 1928.
- [50] M. G. Evans and M. Polanyi, "Inertia and driving force of chemical reactions," *Trans. Faraday Soc.*, vol. 34, pp. 11 – 24, 1938.
- [51] M. Saliccioli and D. G. Vlachos, "Kinetic modeling of Pt catalyzed and computation-driven catalyst discovery for ethylene glycol decomposition," *ACS Catal.*, vol. 1, no. 10, pp. 1246 – 1256, 2011.
- [52] R. Alcalá, M. Mavrikakis, and J. A. Dumesic, "DFT studies for cleavage of C-C and C-O bonds in surface species derived from ethanol on Pt(111)," *J. Catal.*, vol. 218, no. 1, pp. 178 – 190, 2003.
- [53] B. Liu and J. Greeley, "A density functional theory analysis of trends in glycerol decomposition on close-packed transition metal surfaces," *Phys. Chem. Chem. Phys.*, vol. 15, no. 17, pp. 6475 – 6485, 2013.
- [54] B. Liu and J. Greeley, "Decomposition pathways of glycerol via C-H, O-H, and C-C bond scission on Pt(111): A density functional theory study," *J. Phys. Chem. C*, vol. 115, no. 40, pp. 19 702 – 19 709, 2011.
- [55] C. Michel, F. Auneau, F. Delbecq, and P. Sautet, "C-H versus O-H bond dissociation for alcohols on a Rh(111) surface: A strong assistance from hydrogen bonded neighbors," *ACS Catal.*, vol. 1, no. 10, pp. 1430 – 1440, 2011.
- [56] R. Cortese, R. Schimmenti, N. Armata, F. Ferrante, A. Prestianni, D. Duca, and D. Yu. Murzin, "Investigation of polyol adsorption on Ru, Pd, and Re using vdW density functionals," *J. Phys. Chem. C*, vol. 119, no. 30, pp. 17 182 – 17 192, 2015.
- [57] X.-K. Gu, B. Liu, and J. Greeley, "First-principles study of structure sensitivity of ethylene glycol conversion on platinum," *ACS Catal.*, vol. 5, no. 4, pp. 2623 – 2631, 2015.
- [58] X. Xia, S.-I. Choi, J. A. Herron, N. Lu, J. Scaranto, H.-C. Peng, J. Wang, M. Mavrikakis, M. J. Kim, and Y. Xia, "Facile synthesis of palladium right bipyramids and their use as seeds for overgrowth and as catalysts for formic acid oxidation," *J. Am. Chem. Soc.*, vol. 135, no. 42, pp. 15 706 – 15 709, 2013.
- [59] S. Li, J. Scaranto, and M. Mavrikakis, "On the structure sensitivity of formic acid decomposition on Cu catalysts," *Top. Catal.*, vol. 59, pp. 1580 – 1588, 2016.
- [60] S. Singh, S. Li, R. Carrasquillo-Flores, A. C. Alba-Rubio, J. A. Dumesic, and M. Mavrikakis, "Formic acid decomposition on Au catalysts: DFT, microkinetic modeling, and reaction kinetics experiments," *AIChE J.*, vol. 60, no. 4, pp. 1303 – 1319, 2014.

Bibliography

- [61] A. S. Crampton, M. D. Rötzer, C. J. Ridge, F. F. Schweinberger, U. Heiz, B. Yoon, and U. Landman, "Structure sensitivity in the nonscalable regime explored via catalysed ethylene hydrogenation on supported platinum nanoclusters," *Nat. Commun.*, vol. 7, p. 10389, 2016.
- [62] A. Prestianni, M. Crespo-Quesada, R. Cortese, F. Ferrante, L. Kiwi-Minsker, and D. Duca, "Structure sensitivity of 2-methyl-3-butyn-2-ol hydrogenation on Pd: Computational and experimental modeling," *J. Phys. Chem. C*, vol. 118, no. 6, pp. 3119 – 3128, 2014.
- [63] C. Liu, B. Yang, E. Tyo, S. Seifert, J. DeBartolo, B. von Issendorff, P. Zapol, S. Vajda, and L. A. Curtiss, "Carbon dioxide conversion to methanol over size-selected Cu₄ clusters at low pressures," *J. Am. Chem. Soc.*, vol. 137, no. 27, pp. 8676 – 8679, 2015.
- [64] M. Ahmadi, H. Mistry, and B. Roldan Cuenya, "Tailoring the catalytic properties of metal nanoparticles via support interactions," *J. Phys. Chem. Lett.*, vol. 7, no. 17, pp. 3519 – 3533, 2016.
- [65] H. Häkkinen, S. Abbet, A. Sanchez, U. Heiz, and U. Landman, "Structural, electronic and impurity-doping effects in nanoscale chemistry: Supported gold nanoclusters," *Angew. Chem. Int. Ed.*, vol. 42, no. 11, pp. 1297 – 1300, 2003.
- [66] C. T. Campbell, "Catalyst-support interactions: Electronic perturbations," *Nat Chem*, vol. 4, no. 8, 2012.
- [67] I. Fampiou and A. Ramasubramaniam, "CO Adsorption on defective graphene-supported Pt₁₃ nanoclusters," *J. Phys. Chem. C*, vol. 117, no. 39, pp. 19927 – 19933, 2013.
- [68] B. Yoon, H. Häkkinen, U. Landman, A. S. Wörz, J.-M. Antonietti, S. Abbet, K. Judai, and U. Heiz, "Charging effects on bonding and catalyzed oxidation of CO on Au₈ clusters on MgO," *Science*, vol. 307, no. 5708, pp. 403 – 407, 2005.
- [69] J. A. Rodriguez, X. Wang, P. Liu, W. Wen, J. C. Hanson, J. Hrbek, M. Pérez, and J. Evans, "Gold nanoparticles on ceria: importance of O vacancies in the activation of gold," *Top. Catal.*, vol. 44, no. 1-2, pp. 73 – 81, 2007.
- [70] M. J. Frisch, G. W. Trucks, H. B. Schlegel, G. E. Scuseria, M. A. Robb, J. R. Cheeseman, G. Scalmani, V. Barone, B. Mennucci, G. A. Petersson, H. Nakatsuji, M. Caricato, X. Li, H. P. Hratchian, A. F. Izmaylov, J. Bloino, G. Zheng, J. L. Sonnenberg, M. Hada, M. Ehara, K. Toyota, R. Fukuda, J. Hasegawa, M. Ishida, T. Nakajima, Y. Honda, O. Kitao, H. Nakai, T. Vreven, J. A. Montgomery, Jr., J. E. Peralta, F. Ogliaro, M. Bearpark, J. J. Heyd, E. Brothers, K. N. Kudin, V. N. Staroverov, R. Kobayashi, J. Normand, K. Raghavachari, A. Rendell, J. C. Burant, S. S. Iyengar, J. Tomasi, M. Cossi, N. Rega, J. M. Millam, M. Klene, J. E. Knox, J. B. Cross, V. Bakken, C. Adamo, J. Jaramillo, R. Gomperts, R. E. Stratmann, O. Yazyev, A. J. Austin, R. Cammi, C. Pomelli, J. W. Ochterski, R. L. Martin, K. Morokuma, V. G. Zakrzewski, G. A. Voth, P. Salvador, J. J. Dannenberg, S. Dapprich, A. D. Daniels,

- Ö. Farkas, J. B. Foresman, J. V. Ortiz, J. Cioslowski, and D. J. Fox, "Gaussian 09 Revision D.01," Gaussian Inc. Wallingford CT 2009.
- [71] Y. Zhao and D. G. Truhlar, "A new local density functional for main-group thermochemistry, transition metal bonding, thermochemical kinetics, and noncovalent interactions," *J. Chem. Phys.*, vol. 125, no. 19, p. 194101, 2006.
- [72] T. Jacob, R. P. Muller, and W. A. Goddard III, "Chemisorption of atomic oxygen on Pt(111) from dft studies of Pt-clusters," *J. Phys. Chem. B*, vol. 107, no. 35, pp. 9465 – 9476, 2003.
- [73] S. Boys and F. Bernardi, "The calculation of small molecular interactions by the differences of separate total energies. some procedures with reduced errors," *Mol. Phys.*, vol. 19, no. 4, pp. 553 – 566, 1970.
- [74] S. Kandoi, J. Greeley, D. Simonetti, J. Shabaker, J. A. Dumesic, and M. Mavrikakis, "Reaction kinetics of ethylene glycol reforming over platinum in the vapor versus aqueous phases," *J. Phys. Chem. C*, vol. 115, no. 4, pp. 961 – 971, 2011.
- [75] Y. Chen, M. Saliccioli, and D. G. Vlachos, "An efficient reaction pathway search method applied to the decomposition of glycerol on platinum," *J. Phys. Chem. C*, vol. 115, no. 38, pp. 18 707 – 18 720, 2011.
- [76] S. Rangarajan, R. R. O. Brydon, A. Bhan, and P. Daoutidis, "Automated identification of energetically feasible mechanisms of complex reaction networks in heterogeneous catalysis: application to glycerol conversion on transition metals," *Green Chem.*, vol. 16, pp. 813 – 823, 2014.
- [77] O. Skoplyak, M. A. Barteau, and J. G. Chen, "Reforming of oxygenates for H₂ production: Correlating reactivity of ethylene glycol and ethanol on Pt(111) and Ni/Pt(111) with surface d-band center," *J. Phys. Chem. B*, vol. 110, no. 4, pp. 1686 – 1694, 2006.
- [78] M. B. Griffin, E. L. Jorgensen, and J. W. Medlin, "The adsorption and reaction of ethylene glycol and 1,2-propanediol on pd(111): A TPD and HREELS study," *Surf. Sci.*, vol. 604, no. 19-20, pp. 1558 – 1564, 2010.
- [79] J. E. Sutton, P. Panagiotopoulou, X. E. Verykios, and D. G. Vlachos, "Combined dft, microkinetic, and experimental study of ethanol steam reforming on Pt," *J. Phys. Chem. C*, vol. 117, no. 9, pp. 4691 – 4706, 2013.
- [80] J. E. Sutton and D. G. Vlachos, "A theoretical and computational analysis of linear free energy relations for the estimation of activation energies," *ACS Catal.*, vol. 2, no. 8, pp. 1624 – 1634, 2012.
- [81] Y. Zhao and D. G. Truhlar, "The M06 suite of density functionals for main group thermochemistry, thermochemical kinetics, noncovalent interactions, excited states, and transition elements: two new functionals and systematic testing of four M06-class functionals and 12 other functionals," *Theor. Chem. Acc.*, vol. 120, no. 1-3, pp. 215–241, 2008.

Bibliography

- [82] P. Tereshchuk, A. S. Chaves, and J. L. F. Da Silva, "Glycerol adsorption on platinum surfaces: A density functional theory investigation with van der waals corrections," *J. Phys. Chem. C*, vol. 118, no. 28, pp. 15 251 – 15 259, 2014.
- [83] M. Becton and X. Wang, "Grain-size dependence of mechanical properties in polycrystalline boron-nitride: A computational study," *Phys. Chem. Chem. Phys.*, vol. 17, pp. 21 894 – 21 901, 2015.
- [84] G. Postole, A. Gervasini, C. Guimon, A. Auroux, and B. Bonnetot, "Influence of the preparation method on the surface characteristics and activity of boron-nitride-supported noble metal catalysts," *J. Phys. Chem. B*, vol. 110, no. 25, pp. 12 572 – 12 580, 2006.
- [85] J. C. S. Wu and T. Y. Chang, "VOC deep oxidation over Pt catalysts using hydrophobic supports," *Catal. Today*, vol. 44, pp. 111 – 118, 1998.
- [86] R. Schimmenti, R. Cortese, F. Ferrante, A. Prestianni, and D. Duca, "Growth of subnanometric palladium clusters on boron nitride nanotubes: a DFT study," *Phys. Chem. Chem. Phys.*, vol. 18, no. 3, pp. 1750 – 1757, 2016.
- [87] S. Dapprich, I. Komáromi, K. S. Byun, K. Morokuma, and M. J. Frisch, "A new ONIOM implementation in Gaussian98. Part I. The calculation of energies, gradients, vibrational frequencies and electric field derivatives1," *J. Mol. Struct.:THEOCHEM*, vol. 461–462, pp. 1 – 21, 1999.
- [88] A. K. Rappe, C. J. Casewit, K. S. Colwell, W. A. Goddard, and W. M. Skiff, "UFF, a full periodic table force field for molecular mechanics and molecular dynamics simulations," *J. Am. Chem. Soc.*, vol. 114, pp. 10 024 – 10 035, 1992.
- [89] S. Boys and F. Bernardi, "The calculation of small molecular interactions by the differences of separate total energies. Some procedures with reduced errors," *Mol. Phys.*, vol. 19, pp. 553 – 566, 1970.
- [90] X. Wu and X. C. Zeng, "Adsorption of transition-metal atoms on boron nitride nanotube: A density-functional study," *J. Chem. Phys.*, vol. 125, p. 044711, 2006.
- [91] R. Koitz, J. K. Norskov, and F. Studt, "A systematic study of metal-supported boron nitride materials for the oxygen reduction reaction," *Phys. Chem. Chem. Phys.*, vol. 17, pp. 12 722 – 12 727, 2015.
- [92] J. Zhang and A. N. Alexandrova, "Double σ -aromaticity in a surface-deposited cluster: Pd₄ on TiO₂ (110)," *J. Phys. Chem. Lett.*, vol. 3, no. 12, pp. 751 – 754, 2012.
- [93] G. Barone, D. Duca, F. Ferrante, and G. La Manna, "CASSCF/CASPT2 analysis of the fragmentation of H₂ on a Pd₄ cluster," *Int. J. Quant. Chem.*, vol. 110, pp. 558 – 562, 2010.
- [94] A. Prestianni, F. Ferrante, E. M. Sulman, and D. Duca, "Density functional theory investigation on the nucleation and growth of small palladium clusters on a hyper-cross-linked polystyrene matrix," *J. Phys. Chem. C*, vol. 118, pp. 21 006 – 21 013, 2014.

- [95] S. J. Li, X. Zhou, and W. Q. Tian, "Theoretical investigations on decomposition of HCOOH catalyzed by Pd₇ cluster," *J. Phys. Chem. A*, vol. 116, pp. 11 745 – 11 752, 2012.
- [96] P. Liu, "Understanding the behavior of TiO₂(110)-supported Pd₇ cluster: A density functional study," *J. Phys. Chem. C*, vol. 116, no. 48, pp. 25 337 – 25 343, 2012.
- [97] N. Meiyan and Z. Zhi, "Density functional study of hydrogen adsorption and dissociation on small Pd_n (n= 1–7) clusters," *J. Mol. Struct.: THEOCHEM*, vol. 910, no. 1–3, pp. 14 – 19, 2009.
- [98] M. Moseler, H. Häkkinen, R. N. Barnett, and U. Landman, "Structure and magnetism of neutral and anionic palladium clusters," *Phys. Rev. Lett.*, vol. 86, pp. 2545 – 2548, 2001.
- [99] G. Zanti and D. Peeters, "Dft study of small palladium clusters Pd_n and their interaction with a CO ligand (n = 1-9)," *Eur. J. Inorg. Chem.*, vol. 2009, pp. 3904 – 3911, 2009.
- [100] M. Crespo-Quesada, S. Yoon, M. Jin, A. Prestianni, R. Cortese, F. Cárdenas-Lizana, D. Duca, A. Weidenkaff, and L. Kiwi-Minsker, "Shape-dependence of pd nanocrystal carburization during acetylene hydrogenation," *J. Phys. Chem. C*, vol. 119, pp. 1101 – 1107, 2015.
- [101] R. Cortese, F. Ferrante, S. Roggan, and D. Duca, "N-Doped carbon networks: Alternative materials tracing new routes for activating molecular hydrogen," *Chem. Eur. J.*, vol. 21, pp. 3806 – 3814, 2014.
- [102] G. Kresse and J. Furthmüller, "Efficient iterative schemes for *ab initio* total-energy calculations using a plane-wave basis set," *Phys. Rev. B*, vol. 54, no. 16, pp. 11 169 – 11 186, 1996.
- [103] J. P. Perdew, K. Burke, and M. Ernzerhof, "Generalized gradient approximation made simple," *Phys. Rev. Lett.*, vol. 77, pp. 3865 – 3868, 1996.
- [104] S. Grimme, J. Antony, S. Ehrlich, and H. Krieg, "A consistent and accurate ab initio parametrization of density functional dispersion correction (DFT-D) for the 94 elements H-Pu," *J. Chem. Phys.*, vol. 132, no. 15, 2010.
- [105] G. Henkelman, B. P. Uberuaga, and H. Jönsson, "A climbing image nudged elastic band method for finding saddle points and minimum energy paths," *J. Chem. Phys.*, vol. 113, no. 22, pp. 9901 – 9904, 2000.
- [106] C.-A. Lin, J. C. Wu, J.-W. Pan, and C.-T. Yeh, "Characterization of Boron-Nitride supported Pt catalysts for the deep oxidation of benzene," *J. Catal.*, vol. 210, no. 1, pp. 39 – 45, 2002.
- [107] K. A. Kacprzak, I. Czekaj, and J. Mantzaras, "DFT studies of oxidation routes for Pd₉ clusters supported on γ -alumina," *Phys. Chem. Chem. Phys.*, vol. 14, pp. 10 243 – 10 247, 2012.

Bibliography

- [108] D. Duca, F. Ferrante, and G. La Manna, "Theoretical study of palladium cluster structures on carbonaceous supports," *J. Phys. Chem. C*, vol. 111, no. 14, pp. 5402 – 5408, 2007.
- [109] A. Prestianni, R. Cortese, F. Ferrante, R. Schimmenti, D. Duca, S. Hermans, and D. Yu. Murzin, " α -d-Glucopyranose adsorption on a Pd₃₀ cluster supported on boron nitride nanotube," *Top. Catal.*, vol. 59, no. 13-14, pp. 1178 – 1184, 2016.
- [110] J. Scaranto and M. Mavrikakis, "HCOOH decomposition on Pt(111): A DFT study," *Surf. Sci.*, vol. 648, pp. 201 – 211, 2016.
- [111] J. Scaranto and M. Mavrikakis, "Density functional theory studies of HCOOH decomposition on Pd(111)," *Surf. Sci.*, vol. 650, pp. 111 – 120, 2016.
- [112] V. D'Anna, D. Duca, F. Ferrante, and G. L. Manna, "DFT studies on catalytic properties of isolated and carbon nanotube supported Pd₉ cluster-I: adsorption, fragmentation and diffusion of hydrogen," *Phys. Chem. Chem. Phys.*, vol. 11, no. 20, pp. 4077 – 4083, 2009.
- [113] A. Granja, J. A. Alonso, I. Cabria, and M. J. Lopez, "Competition between molecular and dissociative adsorption of hydrogen on palladium clusters deposited on defective graphene," *RSC Adv.*, vol. 5, pp. 47 945 – 47 953, 2015.
- [114] J. Ko, B.-K. Kim, and J. W. Han, "Density Functional Theory study for catalytic activation and dissociation of CO₂ on bimetallic alloy surfaces," *J. Phys. Chem. C*, vol. 120, no. 6, pp. 3438 – 3447, 2016.
- [115] Z. Cheng and C. S. Lo, "Mechanistic and microkinetic analysis of co₂ hydrogenation on ceria," *Phys. Chem. Chem. Phys.*, vol. 18, pp. 7987 – 7996, 2016.
- [116] G. Peng, S. J. Sibener, G. C. Schatz, S. T. Ceyer, and M. Mavrikakis, "CO₂ Hydrogenation to formic acid on Ni(111)," *J. Phys. Chem. C*, vol. 116, no. 4, pp. 3001 – 3006, 2012.
- [117] N. He and Z. H. Li, "Palladium-atom catalyzed formic acid decomposition and the switch of reaction mechanism with temperature," *Phys. Chem. Chem. Phys.*, vol. 18, no. 15, pp. 10 005 – 10 017, 2016.
- [118] S. J. Li, X. Zhou, and W. Q. Tian, "Theoretical investigations on decomposition of HCOOH catalyzed by Pd₇ cluster," *J. Phys. Chem. A*, vol. 116, no. 47, pp. 11 745 – 11 752, 2012.
- [119] I. Fampiou and A. Ramasubramaniam, "Binding of pt nanoclusters to point defects in graphene: Adsorption, morphology, and electronic structure," *J. Phys. Chem. C*, vol. 116, no. 11, pp. 6543 – 6555, 2012.
- [120] A. K. Singh, M. A. Ribas, and B. I. Yakobson, "H-Spillover through the catalyst saturation: An *Ab Initio* thermodynamics study," *ACS Nano*, vol. 3, no. 7, pp. 1657 – 1662, 2009.
- [121] S. A. Shevlin and Z. X. Guo, "Hydrogen sorption in defective hexagonal BN sheets and BN nanotubes," *Phys. Rev. B*, vol. 76, no. 2, p. 024104, 2007.

- [122] B. Ouyang and J. Song, "Strain engineering of magnetic states of vacancy-decorated hexagonal boron nitride," *Appl. Phys. Lett.*, vol. 103, no. 10, p. 102401, 2013.
- [123] E Ferrante, A. Prestianni, R. Cortese, R. Schimmenti, and D. Duca, "Density Functional Theory Investigation on the Nucleation of Homo- and Heteronuclear Metal Clusters on Defective Graphene," *J. Phys. Chem. C*, vol. 120, no. 22, pp. 12 022 – 12 031, 2016.
- [124] P. Hohenberg and W. Kohn, "Inhomogeneous Electron Gas," *Phys. Rev.*, vol. 136, no. 3B, pp. B864–B871, 1964.
- [125] W. Kohn and L. J. Sham, "Self-Consistent Equations Including Exchange and Correlation Effects," *Phys. Rev.*, vol. 140, no. 4A, pp. A1133–A1138, 1965.
- [126] J. P. Perdew and Y. Wang, "Accurate and simple analytic representation of the electron-gas correlation energy," *Phys. Rev. B*, vol. 45, no. 23, pp. 13 244–13 249, 1992.
- [127] P. J. Stephens, F. J. Devlin, C. F. Chabalowski, and M. J. Frisch, "Ab Initio Calculation of Vibrational Absorption and Circular Dichroism Spectra Using Density Functional Force Fields," *J. Phys. Chem.*, vol. 98, no. 45, pp. 11 623–11 627, 1994.
- [128] C. Adamo and V. Barone, "Toward reliable density functional methods without adjustable parameters: The PBE0 model," *J. Che. Phys.*, vol. 110, no. 13, pp. 6158–6170, 1999.

Roberto Schimmenti

5 Via Onorato, 90139 Palermo, Italy
robertoschimmenti89@gmail.com • +39 34715566796 • LinkedIn • Google Scholar



PERSONAL DETAILS

- **Birthdate:** 21/09/1989
- **Birthplace:** Palermo, Italy
- **Nationality:** Italian

EDUCATION

University of Palermo, Palermo, Italy, EU

- **Ph.D. Student in Materials Science and Nanotechnology** Jan 2014 – 2017
 - Research areas: Computational Chemistry, Heterogeneous Catalysis, DFT, Surface Science
- **Master of Science (M.Sc.) in Chemistry** Nov 2011 – Jul 2013
 - Thesis: Thermodynamical approaches for the study of stimuli responsive supramolecular architectures
 - Research areas: Calorimetry, Thermodynamics, Supramolecular Chemistry, Materials Characterization
- **Bachelor of Science (B.Sc.) in Chemistry** Sep 2008 – Sep 2011
 - Thesis: Halloysite nanotubes for the vehicolation of corrosion inhibitor for bronze alloys
 - Research areas: Surface Science, Materials Characterization, Calorimetry, X-Ray Spectroscopy, Thermal Analysis

RESEARCH EXPERIENCES

University of Wisconsin-Madison - USA, Dept. Chemical and Biological Engineering

- **Visiting Scholar, Computational Surface Science and Catalysis Group** Feb 2016 – Jul 2016
 - Project: Theoretical investigation of supported sub-nanometric metal catalysts for selective formic acid decomposition
 - Supervisor: Prof. Manos Mavrikakis
 - Research areas: Computational Catalysis, DFT, Biomass Conversion, Surface Science

SEMINARS HELD

- **Platinum Catalyzed Aqueous Phase Reforming of 1,2-Propanediol: DFT Insights**
 - Group de Chimie Théorique et Modélisation, ENSCP - Chimie ParisTech, Paris (FR) 19/01/2016
- **Aqueous Phase Reforming of 1,2-Propanediol: DFT insights**
 - Computational Catalysis and Surface Science Group, University of Wisconsin-Madison, (USA) 17/02/2016

SCHOOL ATTENDED

- **International School on Ab initio Modelling of Solids 2015**
 - Regensburg (DE), 19-24/07/2015
- **SIESTA Tutorial ZCAM**
 - Zaragoza (ES), 16-19/06/2014
- **EMTCCM School on Theoretical Solid State Chemistry**
 - Zaragoza (ES), 12-16/05/2014

GRANTS

- **"Società Chimica Italiana - Divisione Chimica Teorica e Computazionale"**
 - To attend the XXV Congress of the Italian Chemical Society - Rende 2014

OTHER

- **Participation to international and granted research projects**
 - EU-FP7 funded SusFuelCat Project

PUBLICATIONS

- [1] R. Schimmenti, R. Cortese, L. Godina, F. Ferrante, A. Prestianni, D. Duca, D. Yu. Murzin “A Combined Theoretical and Experimental Approach for Platinum Catalyzed 1,2-Propanediol Aqueous Phase Reforming,” Submitted to *ACS Catal.*
- [2] R. Schimmenti, R. Cortese, D. Duca, M. Mavrikakis, “Boron Nitride Supported Sub-Nanometric Pd₆ Catalyst for Formic Acid Decomposition: A DFT Study” Submitted to *ChemCatChem*
- [3] R. Cortese, R. Schimmenti, F. Ferrante, A. Prestianni, D. Decarolis, D. Duca “Graph Based Analysis of Ethylene-Glycol Decomposition on a Pd Cluster,” Submitted to *J. Phys. Chem. C*
- [4] F. Ferrante, A. Prestianni, R. Cortese, R. Schimmenti, D. Duca “A DFT Investigation on the Nucleation of Homo-and Heteronuclear Metal Clusters on Defective Graphene,” *J. Phys. Chem. C*, 2016, 120, 120122
- [5] A. Prestianni, R. Cortese, F. Ferrante, R. Schimmenti, D. Duca, S. Hermans, D. Yu. Murzin “ α -d-Glucopyranose Adsorption on a Pd 30 Cluster Supported on Boron Nitride Nanotube,” *Top. Catal.*, 2016, 59, 1178
- [6] R. Schimmenti, R. Cortese, A. Prestianni, F. Ferrante, D. Duca “Growth of sub-nanometric palladium clusters on boron nitride nanotubes: a DFT study,” *Phys. Chem. Chem. Phys.*, 2016, 18, 1750
- [7] R. Cortese, R. Schimmenti, F. Ferrante, A. Prestianni, D. Duca, D. Yu. Murzin “Investigation of Polyol Adsorption on Ru, Pd, and Re Using vdW Density Functionals,” *J. Phys. Chem. C*, 2015, 119, 17182
- [8] G. Lazzara, S. Milioto, R. Schimmenti “Thermodynamics of Cyclodextrin-Star Copolymer Threading-Dethreading Process,” *J. Therm. Anal. Calor.*, 2015, 121, 1345

SELECTED

CONGRESS

COMMUNICATIONS

- [1] R. Schimmenti, R. Cortese, F. Ferrante, A. Prestianni, D. Duca
“Computational Investigation of Palladium Supported Boron Nitride Nanotube Catalysts”
Oral presentation at Europacat XII, Kazan, Russia, 30 August- 4 September 2015
- [2] R. Schimmenti, R. Cortese, D. Duca
“A computational approach to study Aqueous Phase Reforming”
Oral presentation at XXV Congress of Italian Chemical Society, Rende, Italy, 7-12 September 2014
- [3] R. Cortese, F. Ferrante, R. Schimmenti, A. Prestianni, D. Duca
“Computational study of metal-free N-doped carbon networks as hydrogenation catalysts”
Poster presentation at Europacat XII, Kazan, Russia, 30 August- 4 September 2015
- [4] R. Cortese, R. Schimmenti, F. Ferrante, A. Prestianni, D. Duca
“Theoretical Investigation of Aqueous Phase Reforming of 1,2 Propanediol over a Pt catalyst”
Poster presentation at CHITEL 2015, Torino, Italy, 26 - 31 July 2015
- [5] R. Schimmenti, R. Cortese, F. Ferrante, A. Prestianni, D. Duca
“Computationally driven design of supported metal catalysts for biomass conversion technologies”
Best Poster presentation at International School on Ab initio Modelling of Solids, Regensburg, Germany, 19 - 24 July 2015

[CV compiled on 2017-01-29]